

UNIVERSITY OF WEST BOHEMIA
FACULTY OF APPLIED SCIENCES

**Magnetron sputter deposition of Zr–Cu
based thin-film metallic alloys
and nitride films**

Ing. Michal Zítek

*A thesis submitted for the degree of Doctor of Philosophy
in the field of Plasma Physics and Physics of Thin Films*

Supervisor: doc. Ing. Petr Zeman, Ph.D.

Department of Physics

Plzeň 2018

ZÁPADOČESKÁ UNIVERZITA V PLZNI
FAKULTA APLIKOVANÝCH VĚD

**Magnetronová depozice tenkovrstvých
kovových slitin a nitridových vrstev
na bázi Zr–Cu**

Ing. Michal Zítek

*Disertační práce
k získání akademického titulu doktor
v oboru Fyzika plazmatu a tenkých vrstev*

*Školitel: doc. Ing. Petr Zeman, Ph.D.
Katedra fyziky*

Plzeň 2018

Preface

Hereby, I declare that I wrote the submitted Ph.D. thesis by myself using results obtained during my Ph.D. study and using the duly cited literature. The thesis is in a form of four scientific papers published in impacted international journals.

The thesis includes the results obtained during my Ph.D. study at the Department of Physics and NTIS, European Centre of Excellence, University of West Bohemia, since September 2014. This research was financially supported by the projects SGS–2013–045 (2013–2015): New thin-film materials and plasma deposition systems, SGS–2016–056 (2016–2018): New nanostructured thin-film materials formed by plasma technologies, GA16-18183S Advanced surface coatings with enhanced properties and thermal stability, and GAP108/12/0393 Hard nanocomposite coatings with enhanced toughness and unique properties.

Plzeň, 11.9.2018

.....

Ing. Michal Zítek

Acknowledgments

At this point, I would like to thank my supervisor doc. Ing. Petr Zeman, Ph.D. for guidance during my Ph.D. study, numerous interesting discussions and valuable advice. I would also like to thank prof. Ing. Jindřich Musil, DrSc. for guidance and helpful discussions in the beginning of my study and prof. RNDr. Jaroslav Vlček, CSc. for motivating me to enter this doctoral program. Many thanks go also to all Ph.D. students for creating a friendly atmosphere in the laboratories. I am also very grateful to my family and my girlfriend Eva for supporting me during my Ph.D. study.

Contents

I. Introduction	8
1. Metallic glasses	9
2. Nanocomposite coatings	11
3. References	12
II. Aims	15
III. Results	16
A Amorphous Zr-Cu thin-film alloys with metallic glass behavior	17
Abstract	18
1. Introduction	18
2. Experimental details	19
3. Results and discussion.....	19
3.1. Elemental composition	20
3.2. Structure.....	21
3.3. Thermal behavior.....	22
3.4. Mechanical properties and residual stress	24
3.5. Surface properties and microstructure	24
3.6. Electrical resistivity	25
4. Conclusions	25
Acknowledgments	25
References.....	25
B Tuning properties and behavior of magnetron sputtered Zr–Hf–Cu metallic glasses	27
Abstract	28
1. Introduction	28
2. Experimental details	29
3. Results and discussion.....	29
3.1. Elemental composition	30
3.2. Structure.....	32
3.3. Thermal behavior.....	32
3.4. Mechanical properties.....	33
3.5. Surface properties	34

3.6. Electrical resistivity	34
3.7. Oxidation resistance	34
4. Conclusions	34
Acknowledgments	34
References.....	35
C Impact of Al or Si addition on properties and oxidation resistance of magnetron sputtered Zr–Hf–Al/Si–Cu metallic glasses.....	36
Abstract.....	37
1. Introduction	37
2. Experimental details	38
3. Results and discussion.....	38
3.1. Elemental composition	39
3.2. Structure.....	39
3.3. Thermal behavior.....	39
3.4. Mechanical properties.....	43
3.5. Surface properties	43
3.6. Electrical resistivity	43
3.7. Oxidation resistance	44
4. Conclusions	44
Acknowledgments	44
References.....	44
D Flexible antibacterial Zr–Cu–N thin films resistant to cracking	46
Abstract.....	47
1. Introduction	47
2. Experiment	48
3. Results and discussion.....	49
3.1. Structure of flexible Zr–Cu–N films	49
3.2. Antibacterial properties of Zr–Cu–N films	49
3.3. Mechanical properties of Zr–Cu–N films.....	50
3.4. Enhanced resistance of Zr–Cu–N films to cracking.....	51
4. Conclusions	52
Acknowledgment.....	52
IV. Conclusions.....	54

V. Further publications of the candidate	56
1. Papers in impacted international journals	56
2. Contributions at international conferences.....	56
Abstract	59
Resumé	61

I. Introduction

Over the last decades, significant attention has been paid to the investigation of new advanced materials. This trend is closely related to the market requirements for materials with enhanced properties and/or lifetime. The surface of the material is crucial for many applications. Therefore, using a new material with enhanced properties in a form of a thin film is suitable for surface modification. The thin film may improve a large variety of properties of the underlying material, for instance, mechanical, chemical, optical, electrical and antibacterial properties.

In order to prepare new materials, including the materials presented in this Ph.D. thesis, advanced methods and approaches are required. It has been shown that glow discharge processes, including magnetron sputtering, are a proper technique for such a purpose. In this Ph.D. thesis we used several regimes of magnetron sputtering. For the synthesis of the thin-film metallic glasses based on Zr–Cu, we used a combination of a non-reactive conventional direct-current (dc) magnetron sputtering and high-power impulse magnetron sputtering (HiPIMS). In case of the nanocomposite Zr–Cu–N films we used a reactive pulsed magnetron sputtering.

In general, magnetron sputtering utilizes a magnetic field to sustain the low-pressure plasma discharge close to the cathode (target). The discharge is ignited and powered by applying electrical voltage between the cathode and the anode (usually the walls of the deposition chamber) in an inert process gas (usually Ar). Ions generated in the plasma are accelerated towards the target and by bombarding the target they sputter the atoms of the target material which subsequently create a thin film on the substrate. Besides the atoms, the bombardment of the target by the ions also emits electrons which are trapped in the vicinity of the target by the magnetic field and efficiently ionize the process gas [1–3].

Conventional dc magnetron sputtering is characterized by relatively low target power densities (in order of a few W/cm^2). The applied target power is limited in order to avoid target overheating. The degree of ionization of the sputtered atoms is relatively low. Therefore, the flux of particles onto the substrate consists mostly of neutral atoms. In the case of dc pulsed magnetron sputtering, the target voltage is applied in pulses and the average target power density over a period is comparable with the continuous dc magnetron sputtering. Generally, pulsed magnetron sputtering leads to a higher ionization and thus to a higher energy of sputtered atoms delivered to the substrate. HiPIMS, a relatively new technique, is a unique type of a dc pulsed magnetron sputtering. It is defined by short pulses (usually in order of tens or hundreds of μs) at a low duty cycle ($\sim 1\%$) and a very high power density ($>1 \text{ kW}/\text{cm}^2$) in a pulse. Such a high power density leads to a much larger degree of ionization of sputtered atoms. That is of great importance for certain applications such as filling of trenches and allows us also to control the deposition process and thus to tune the properties of the thin films [4].

The following subsections deal with materials studied in this Ph.D. thesis and clarify the motivation to investigate them. The major part of this Ph.D. thesis (Parts A–C) is devoted to the development of Zr–Cu based thin-film metallic glasses with enhanced mechanical and thermal properties. The second part of this Ph.D. thesis (Part D) is devoted to nanocomposite Zr–Cu–N

films with enhanced mechanical properties and strong antibacterial activity. The results obtained for these two material systems will be used in further research. Recently, it was shown that a combination of a metallic glass and a crystalline metal may lead to a suppression of a propagation of the shear bands [5–7]. As far as we know, only a limited attentions was paid to the combination of a metallic glass with a nanocomposite material [8]. Therefore, the next step in that study will be an examination of a possibility to prepare a multi-layer system of a thin-film metallic glass and a nitride film with emphasis on the enhancement of its mechanical properties.

1. Metallic glasses

Metallic glasses, first synthesized by Klement et al. in 1960 [9], are amorphous metallic alloys. They consist of elements that interact mainly via metallic bonds [10] and possess disordered atomic structure without grain boundaries. The atoms exhibit neither long-range periodical arrangement nor a completely random arrangement of atoms. In part, they are distributed in short-range atomic ordering units called icosahedral clusters [11–14]. In order to prepare the metallic glass, very high cooling rates from melt or gas (in order of $10^3 - 10^6$ K/s) are required to avoid nucleation and a subsequent crystal growth. Their unique structure leads to superior physical and mechanical properties including, for instance, high yield strength, elastic strain and hardness, good wear and corrosion resistance, excellent surface finishing and temperature-independent electrical resistivity compared to their crystalline counterparts [15–17].

Fig. 1 shows a typical thermal behavior of the metallic glass, measured using differential scanning calorimetry (DSC), which qualitatively differs from the behavior of a conventional amorphous material. Specifically, the DSC curve presented in Fig. 1 was obtained from a binary $Zr_{45}Cu_{55}$ thin-film metallic glass. One may notice that the DSC curve of the metallic glass may be characterized by a decrease of the heat flow before the onset of the exothermic crystallization peak. Such a decrease is a typical behavior of the glass and its onset is called a glass transition.

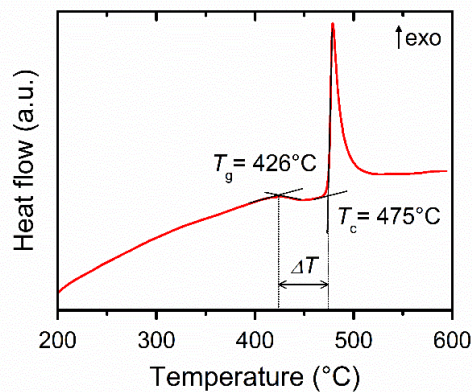


Fig. 1. DSC curve of the $Zr_{45}Cu_{55}$ thin-film metallic glass showing the glass transition and crystallization in detail. The determination of the glass transition temperature T_g , crystallization temperature T_c and supercooled liquid region ΔT is highlighted.

By a detailed examination of the DSC curve we can identify the glass transition temperature T_g , the crystallization temperature T_c and the supercooled liquid region ΔT ($\Delta T = T_c - T_g$). These temperatures and the width of the supercooled liquid region are characteristic values of the metallic glass and greatly depend on the elemental composition and the heating rate during the measurement. The metallic glass heated up into the supercooled liquid region exhibits thermo-plastic behavior. Such a behavior is interesting, for instance, for sealing of scratches or for forming the material into different shapes or structures from the original material [17,18].

The plastic deformation of the metallic glasses is also quite different when compared with the conventional crystalline metals. In the case of metallic glasses, the major mechanism to accommodate plastic deformation is shear-banding. The shear band is a form of a plastic instability that localizes large shear strains in a relatively thin band when a material is being deformed. The origin of the strain localization is connected with the shear-softening. When a local region is plastically deformed, it becomes softer than the surrounding undeformed regions and thus is more susceptible to a subsequent flow. That behavior leads to a concentration of the plastic flow into a thin band. Such a behavior is shown in Fig. 2 where shear bands are formed after indentation. Nevertheless, the metallic glasses exhibit larger ductility than ceramics [19–21].

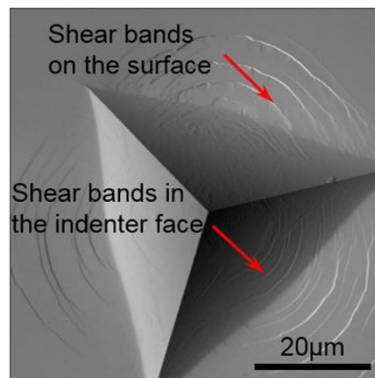


Fig. 2. AFM image of the indentation imprint of the $\text{Pd}_{40}\text{Cu}_{30}\text{Ni}_{10}\text{P}_{20}$ bulk metallic glass at the indentation load of 8 N (adapted from [21]).

In this Ph.D. thesis, we started the investigation of thin-film metallic glasses with the binary Zr–Cu system. This system exhibit one of the highest glass forming ability due to the difference in atomic sizes of Zr (1.60 Å) and Cu (1.28 Å) and to a large negative heat of mixing (–23 kJ/mol) of Zr and Cu [22]. Zr–Cu metallic glasses were prepared by various methods in both bulk and thin-film form.

The Zr–Cu thin-film metallic glasses found in the literature were prepared mostly by a conventional dc magnetron sputtering [22–25]. Advanced sputtering methods such as HiPIMS had not been used for the synthesis of this kind of a material so far. Therefore, we also focused on the preparation of Zr–Cu thin-film metallic glasses by this method. Moreover, we systematically investigated their properties including thermal, mechanical, surface and electrical properties.

The next step of the study was to investigate the possibility to enhance the properties of the binary Zr–Cu thin films by adding Hf. We varied the Hf/(Hf+Zr) ratio from 0 to 1 at two different constant Cu contents. So far, the ternary Zr–Hf–Cu system has been almost exclusively studied theoretically [26,27] indicating great glass forming ability in a wide composition range.

Regarding the experimental work only $Zr_{25}Hf_{25}Cu_{50}$ metallic alloy in a form of 50–60 μm thick ribbons was synthesized by Basu et al. [28]. It was shown that the ribbons were X-ray amorphous and exhibited glass transition. The partial replacement of Zr by Hf led to an increase of the crystallization temperature by about 50 °C. Unfortunately, no other elemental compositions or properties have been investigated yet. Therefore, we carried out a systematic study dealing with a gradual substitution of Zr for Hf in the Zr–Hf–Cu system with the aim to find the effect of Hf on the properties of the Zr–Hf–Cu thin-film metallic alloys including thermal behavior, mechanical properties and oxidation resistance.

It has been shown that alloying with an appropriate element in a proper amount is very effective in increasing glass forming ability, enhancing mechanical and magnetic properties, and improving thermal stability of some bulk metallic glasses [29]. Hence, the next step of our study was to examine the possibility to improve or tune the properties of the Zr–Hf–Cu thin-film metallic alloys by addition of Al or Si. Heretofore, quaternary Zr–Hf–Al/Si–Cu metallic alloys had not been studied in the literature. On the other hand, it was reported that alloying with Al or Si increased the crystallization temperature and the width of the supercooled liquid region of other Zr- and Cu-based metallic glasses [30–32]. In the case of Al, an increase of hardness and Young’s modulus was also observed [32]. Therefore, we investigated the ability of the Zr–Hf–Al/Si–Cu systems to form metallic glasses and the effect of the addition of Al or Si on the properties of the films. Particular attention was devoted to improvement of thermal stability, mechanical properties and oxidation resistance.

2. Nanocomposite coatings

Nanocomposite coatings consist of at least two separate phases with a nanocrystalline and/or amorphous structure. The size of the grains of the nanocrystalline phase is of the order of tens of nanometers or less. The growth of these grains is hindered by the segregation of the second phase on the grain boundaries of the first phase. Thus, the number of atoms in the boundary region is comparable to the amount of atoms in the grains. Such a unique structure, where the very small nanocrystalline grains are surrounded by the largely amorphous boundaries, exhibit different properties when compared to the conventional material with grains larger than 100 nm, e.g. very high hardness. We distinguish nanocomposites composed of two hard phases (nc-MeN/hard phase – nc- denotes nanocrystalline and Me denotes metal forming nitride phase) and nanocomposites composed of one hard and one soft phase (nc-MeN/soft phase) [33–35].

Zr–Cu–N thin films belong to the nc-MeN/soft phase group. In that case, the nanocrystalline phase is formed by ZrN and the soft phase is formed by Cu which segregates on the grain boundaries of the ZrN. Zr–Cu–N thin films were already synthesized by magnetron sputtering [36–38] and it was shown that it is possible to prepare superhard (defines as having hardness higher than 40 GPa) films with hardness of up to 55 GPa. It was also shown for different material systems that Cu-containing nanocomposite films with a sufficient amount of Cu exhibit an antibacterial activity. For instance, Cr–Cu–N films containing 24 at.% Cu exhibit strong anti-

bacterial effect [39]. Therefore, we focused on finding appropriate deposition conditions to prepare antibacterial but still hard Zr–Cu–N thin films. Moreover, we investigated the resistance to cracking of these coatings after bending and high indentation loads.

3. References

- [1] I. Safi, Recent aspects concerning DC reactive magnetron sputtering of thin films: a review, *Surf. Coatings Technol.* 127 (2000) 203–219. doi:10.1016/S0257-8972(00)00566-1.
- [2] P.J. Kelly, R.D. Arnell, Magnetron sputtering: a review of recent developments and applications, *Vacuum.* 56 (2000) 159–172. doi:10.1016/S0042-207X(99)00189-X.
- [3] G. Bräuer, B. Szyszka, M. Vergöhl, R. Bandorf, Magnetron sputtering – Milestones of 30 years, *Vacuum.* 84 (2010) 1354–1359. doi:10.1016/j.vacuum.2009.12.014.
- [4] A. Anders, J. Andersson, A. Ehiasarian, High power impulse magnetron sputtering: Current-voltage-time characteristics indicate the onset of sustained self-sputtering, *J. Appl. Phys.* 102 (2007). doi:10.1063/1.2817812.
- [5] M.C. Liu, C.J. Lee, Y.H. Lai, J.C. Huang, Microscale deformation behavior of amorphous/nanocrystalline multilayered pillars, *Thin Solid Films.* 518 (2010) 7295–7299. doi:10.1016/j.tsf.2010.04.096.
- [6] H.J. Pei, S.Y. Kuan, M.C. Liu, J.C. Huang, Tensile behavior of amorphous/nanocrystalline ZrCu/Cu multilayered films with graded interfaces, *Intermetallics.* 31 (2012) 191–195. doi:10.1016/j.intermet.2012.07.002.
- [7] Y. Cui, P. Huang, F. Wang, T.J. Lu, K.W. Xu, The hardness and related deformation mechanisms in nanoscale crystalline–amorphous multilayers, *Thin Solid Films.* 584 (2015) 270–276. doi:10.1016/j.tsf.2015.01.067.
- [8] Z. Song, Y. Li, G. He, L. Yao, J. Wang, S. Guo, K. Xu, Microstructure and Property of Self-format Graded Diffusion Barrier in Cu(Zr)/ZrN Film System, *Phys. Procedia.* 32 (2012) 645–650. doi:10.1016/j.phpro.2012.03.613.
- [9] W. Klement, R.H. Willens, P. Duwez, Non-crystalline Structure in Solidified Gold–Silicon Alloys, *Nature.* 187 (1960) 869–870. doi:10.1038/187869b0.
- [10] A.L. Greer, E. Ma, Bulk Metallic Glasses: At the Cutting Edge of Metals Research, *MRS Bull.* 32 (2007) 611–619. doi:https://doi.org/10.1557/mrs2007.121.
- [11] H.W. Sheng, W.K. Luo, F.M. Alamgir, J.M. Bai, E. Ma, Atomic packing and short-to-medium-range order in metallic glasses, *Nature.* 439 (2006) 419–425. doi:10.1038/nature04421.
- [12] N. Mattern, P. Jónvári, I. Kaban, S. Gruner, A. Elsner, V. Kokotin, H. Franz, B. Beuneu, J. Eckert, Short-range order of Cu–Zr metallic glasses, *J. Alloys Compd.* 485 (2009) 163–169. doi:10.1016/j.jallcom.2009.05.111.
- [13] G.A. Almyras, C.E. Lekka, N. Mattern, G.A. Evangelakis, On the microstructure of the Cu₆₅Zr₃₅ and Cu₃₅Zr₆₅ metallic glasses, *Scr. Mater.* 62 (2010) 33–36. doi:10.1016/j.scriptamat.2009.09.019.

- [14] D.Z. Chen, C.Y. Shi, Q. An, Q. Zeng, W.L. Mao, W.A. Goddard, J.R. Greer, Fractal atomic-level percolation in metallic glasses, *Science*. 349 (2015) 1306–10. doi:10.1126/science.aab1233.
- [15] M. Telford, The case for bulk metallic glass, *Mater. Today*. 7 (2004) 36–43. doi:10.1016/S1369-7021(04)00124-5.
- [16] M.F. Ashby, A.L. Greer, Metallic glasses as structural materials, *Scr. Mater.* 54 (2006) 321–326. doi:10.1016/j.scriptamat.2005.09.051.
- [17] A.L. Greer, Metallic glasses...on the threshold, *Mater. Today*. 12 (2009) 14–22. doi:10.1016/S1369-7021(09)70037-9.
- [18] B. Sarac, S. Bera, F. Spieckermann, S. Balakin, M. Stoica, M. Calin, J. Eckert, Micropatterning kinetics of different glass-forming systems investigated by thermoplastic net-shaping, *Scr. Mater.* 137 (2017) 127–131. doi:10.1016/j.scriptamat.2017.02.038.
- [19] A.L. Greer, Y.Q. Cheng, E. Ma, Shear bands in metallic glasses, *Mater. Sci. Eng. R Reports*. 74 (2013) 71–132. doi:10.1016/j.mser.2013.04.001.
- [20] H. Jia, F. Liu, Z. An, W. Li, G. Wang, J.P. Chu, J.S.C. Jang, Y. Gao, P.K. Liaw, Thin-film metallic glasses for substrate fatigue-property improvements, *Thin Solid Films*. 561 (2014) 2–27. doi:10.1016/j.tsf.2013.12.024.
- [21] Y.M. Lu, B.A. Sun, L.Z. Zhao, W.H. Wang, M.X. Pan, C.T. Liu, Y. Yang, Shear-banding Induced Indentation Size Effect in Metallic Glasses, *Sci. Rep.* 6 (2016) 28523. doi:10.1038/srep28523.
- [22] M. Apreutesei, P. Steyer, L. Joly-Pottuz, A. Billard, J. Qiao, S. Cardinal, F. Sanchette, J.M. Pelletier, C. Esnouf, Microstructural, thermal and mechanical behavior of co-sputtered binary Zr–Cu thin film metallic glasses, *Thin Solid Films*. 561 (2014) 53–59. doi:10.1016/j.tsf.2013.05.177.
- [23] Q. Jing, Y. Xu, X.-Y. Zhang, G. Li, L.-X. Li, Z. Xu, M.-Z. Ma, R.-P. Liu, Zr-Cu Amorphous Films Prepared by Magnetron Co-sputtering Deposition of Pure Zr and Cu, *Chinese Phys. Lett.* 26 (2009) 086109. doi:10.1088/0256-307X/26/8/086109.
- [24] P. Coddet, F. Sanchette, J.C. Rousset, O. Rapaud, C. Coddet, On the elastic modulus and hardness of co-sputtered Zr-Cu-(N) thin metal glass films, *Surf. Coat. Technol.* 206 (2012) 3567–3571. doi:10.1016/j.surfcoat.2012.02.036.
- [25] M. Apreutesei, P. Steyer, A. Billard, L. Joly-Pottuz, C. Esnouf, Zr–Cu thin film metallic glasses: An assessment of the thermal stability and phases' transformation mechanisms, *J. Alloys Compd.* 619 (2015) 284–292. doi:10.1016/j.jallcom.2014.08.253.
- [26] J. Basu, B.S. Murty, S. Ranganathan, Glass forming ability: Miedema approach to (Zr, Ti, Hf)-(Cu, Ni) binary and ternary alloys, *J. Alloys Compd.* 465 (2008) 163–172. doi:10.1016/j.jallcom.2007.10.131.
- [27] S.Y. Luo, Y.Y. Cui, Y. Dai, J.H. Li, B.X. Liu, Interatomic potential to predict the favored and optimized compositions for ternary Cu-Zr-Hf metallic glasses, *J. Appl. Phys.* 112 (2012) 103518. doi:10.1063/1.4766389.
- [28] J. Basu, S. Ranganathan, Glass forming ability and stability: Ternary Cu bearing Ti, Zr, Hf alloys, *Intermetallics*. 17 (2009) 128–135. doi:10.1016/j.intermet.2008.10.006.
- [29] Z.P. Lu, C.T. Liu, Role of minor alloying additions in formation of bulk metallic glasses: A Review, *J. Mater. Sci.* 39 (2004) 3965–3974. doi:10.1023/B:JMSC.0000031478.73621.64.
- [30] H. Choi-Yim, R. Busch, W.L. Johnson, The effect of silicon on the glass forming ability of the Cu₄₇Ti₃₄Zr₁₁Ni₈ bulk metallic glass forming alloy during processing of composites, *J. Appl. Phys.* 83 (1998) 7993–7997. doi:10.1063/1.367981.

- [31] P. Yu, H.Y. Bai, M.B. Tang, W.L. Wang, Excellent glass-forming ability in simple Cu₅₀Zr₅₀-based alloys, 2005. doi:10.1016/j.jnoncrysol.2005.03.012.
- [32] T.L. Cheung, C.H. Shek, Thermal and mechanical properties of Cu–Zr–Al bulk metallic glasses, *J. Alloys Compd.* 434 (2007) 71–74. doi:10.1016/j.jallcom.2006.08.109.
- [33] J. Musil, Hard and superhard nanocomposite coatings, *Surf. Coatings Technol.* 125 (2000) 322–330. doi:10.1016/S0257-8972(99)00586-1.
- [34] J. Musil, J. Vlček, Magnetron sputtering of hard nanocomposite coatings and their properties, *Surf. Coat. Technol.* 142–144 (2001) 557–566.
- [35] S. Zhang, N. Ali, *Nanocomposite Thin Films and Coatings*, Imperial College Press, London, 2007.
- [36] J. Musil, P. Zeman, H. Hrubý, P.H. Mayrhofer, ZrN/Cu nanocomposite film—a novel superhard material, *Surf. Coatings Technol.* 120–121 (1999) 179–183. doi:10.1016/S0257-8972(99)00482-X.
- [37] J. Musil, P. Zeman, Structure and microhardness of magnetron sputtered ZrCu and ZrCu-N films, *Vacuum.* 52 (1999) 269–275. doi:10.1016/S0042-207X(98)00297-8.
- [38] P. Zeman, R. Čerstvý, P.H. Mayrhofer, C. Mitterer, J. Musil, Structure and properties of hard and superhard Zr–Cu–N nanocomposite coatings, *Mater. Sci. Eng. A.* 289 (2000) 189–197. doi:doi.org/10.1016/S0921-5093(00)00917-5.
- [39] Y.-C. Kuo, J.-W. Lee, C.-J. Wang, Y.-J. Chang, The effect of Cu content on the microstructures, mechanical and antibacterial properties of Cr–Cu–N nanocomposite coatings deposited by pulsed DC reactive magnetron sputtering, *Surf. Coatings Technol.* 202 (2007) 854–860. doi:10.1016/j.surfcoat.2007.05.062.

II. Aims

The Ph.D. thesis is focused on the preparation and characterization of thin-film metallic alloys and nitride films based on the Zr–Cu system. The metallic alloys were non-reactively deposited by a combination of high-power impulse magnetron sputtering and conventional dc magnetron sputtering while the nitride films were deposited using reactive pulsed dual magnetron sputtering.

The main aims of the Ph.D. thesis were defined as follows:

1. To deposit binary Zr–Cu thin-film alloys in a very wide composition range and to systematically investigate the evolution of the structure and thermal, mechanical, electrical and surface properties. To find the conditions which favor the formation of Zr–Cu metallic glasses and to evaluate the benefits of sputtering of Cu in a high-power impulse regime.
2. To deposit ternary Zr–Hf–Cu thin-film alloys with increasing Hf/(Hf+Zr) ratio at different Cu contents and to investigate the effect of a gradual substitution of Hf for Zr on the film properties, the thermal stability of their glassy state and the oxidation resistance.
3. To deposit quaternary Zr–Hf–Al/Si–Cu thin-film alloys with a low content of Al or Si and to investigate the possibility to further enhance the film properties and extend their thermal stability and oxidation resistance to higher temperatures.
4. To deposit nanocomposite Zr–Cu–N films at different Cu contents and to find conditions which lead to the formation of the films with enhanced mechanical properties, especially the resistance to cracking, and the antibacterial activity.

III. Results

The thesis is submitted in a form of four scientific papers (Parts A–D) published in impacted international journals. These papers contain the most important results obtained during my Ph.D. study at the Department of Physics and NTIS, European Centre of Excellence, University of West Bohemia since September 2014. The following paragraphs summarize my contribution to each paper.

Part A: Amorphous Zr–Cu thin-film alloys with metallic glass behavior

I carried out all the depositions of the Zr–Cu thin-film alloys together with the measurements of the discharge and deposition characteristics. I performed the measurements of thickness, mechanical, electrical and hydrophobic properties of the films. In addition, I actively participated in the interpretation of the results of the structure, microstructure, thermal behavior, elemental composition and surface roughness. I actively participated in writing of the paper.

Part B: Tuning properties and behavior of magnetron sputtered Zr–Hf–Cu metallic glasses

I carried out all the depositions of the Zr–Hf–Cu thin-film alloys together with the measurements of the discharge and deposition characteristics. I performed the measurements of thickness, elemental composition, mechanical, electrical and hydrophobic properties, and surface roughness of the films. In addition, I actively participated in the interpretation of the results of the structure, thermal behavior and oxidation resistance. I wrote the first version of the paper and I actively participated in completing the final version of the paper.

Part C: Impact of Al or Si addition on properties and oxidation resistance of magnetron sputtered Zr–Hf–Al/Si–Cu metallic glasses

I carried out all the depositions of the Zr–Hf–Al/Si–Cu thin-film alloys together with the measurements of the discharge and deposition characteristics. I performed the measurements of thickness, elemental composition, mechanical, electrical and hydrophobic properties, and surface roughness of the films. In addition, I actively participated in the interpretation of the results of the structure, thermal behavior and oxidation resistance. I wrote the first version of the paper and I actively participated in completing the final version of the paper.

Part D: Flexible antibacterial Zr–Cu–N thin films resistant to cracking

I carried out all the depositions of the Zr–Cu–N thin films together with the measurements of the discharge and deposition characteristics. I performed the measurements of thickness, mechanical properties and resistance to cracking of the films. In addition, I actively participated in the interpretation of the results of the structure and antibacterial activity. I actively participated in writing of the paper.

Part A

Amorphous Zr–Cu thin-film alloys with metallic glass behavior

P. Zeman, M. Zítek, Š. Zuzjaková, R. Čerstvý

Journal of Alloys and Compounds 696 (2017) 1298–1306



Amorphous Zr–Cu thin-film alloys with metallic glass behavior



P. Zeman^{*}, M. Zítek, Š. Zuzjaková, R. Čerstvý

Department of Physics and NTIS - European Centre of Excellence, University of West Bohemia, Univerzitní 8, 306 14, Plzeň, Czech Republic

ARTICLE INFO

Article history:

Received 8 September 2016
Received in revised form
29 November 2016
Accepted 6 December 2016
Available online 9 December 2016

Keywords:

Zr–Cu
Amorphous material
Metallic glass
Thin films
Magnetron sputtering

ABSTRACT

Binary Zr–Cu thin-film alloys were prepared by non-reactive conventional dc and impulse magnetron co-sputtering using two unbalanced magnetrons equipped with Zr and Cu targets. The magnetron with the Zr target was operated in a dc regime while the magnetron with the Cu target in a pulse regime either at low or high density discharge conditions. The elemental composition in the films was controlled in a very wide composition range (~10–90 at.%). The evolution of the structure, thermal behavior, mechanical, electrical and surface properties of Zr–Cu films with increasing Cu content was systematically investigated. We found that Zr–Cu thin-film metallic glasses were prepared with the Cu content between approximately 30 and 65 at.% Cu independently of the low or high density discharge conditions used. A clear correlation between the evolution of the crystallization temperature and mechanical properties with increasing Cu content was observed. The deposition at the high density discharge conditions resulted in a preparation of the Zr–Cu thin-film metallic alloys with a compressive stress (<0 GPa), an enhanced hardness (>7 GPa), very smooth (surface roughness < 1 nm) and hydrophobic (water contact angle >100°) surface.

© 2016 Elsevier B.V. All rights reserved.

1. Introduction

Metallic alloys are commonly fabricated as crystalline materials by a relatively slow-cooling casting of a melt. Such alloys are characterized by a highly regular, well-defined arrangement of atoms on a three dimensional lattice possessing the translation periodicity. Increasing the cooling rate high enough (10^3 – 10^6 K/s) while mixing appropriate metallic elements may result in a formation of non-crystalline metallic alloys in a non-equilibrium metastable state. The structure of these alloys is then not characterized by either a long-range periodical arrangement or completely random arrangement of atoms. Recently, molecular dynamics simulations have revealed a short- and medium-range atomic ordering in these solids [1–4]. Base structural units are not unit cells as in the case of crystalline solids but various kinds of polyhedral clusters of atoms. Most of atoms are incorporated in icosahedral clusters (1 central atom surrounded by 12 atoms) having the highest packing density among others. Some clusters may also place in groups to form supercluster structures [5,6]. The presence of these specific structural units based on clusters gives rise to exceptional physical and functional properties of non-

crystalline metallic alloys compared to their crystalline counterparts.

Annealing of these non-crystalline alloys leads to their viscous flow in the supercooled liquid region between the glass transition temperature and the crystallization temperature. Hence, these alloys are called metallic glasses and can be easily deformed in this region. In addition, it has been discovered that metallic glasses exhibit a high yield strength, high elastic strain and hardness, high magnetic permeability, temperature-independent electrical resistivity, low wear and corrosion resistance, excellent surface finishing, and biocompatibility [7–10]. However, they possess a limited tensile ductility at room temperature. The plastic flow in bulk metallic glasses during tension is highly localized into shear deformation bands, which leads to their instantaneous catastrophic failure by a shear rupture [11]. This drawback has been reported to be partially overcome by a reduction of the thickness of metallic glasses below a critical value, which results in an enhanced plasticity and fatigue resistance of thin-film metallic glasses [12–14].

The present study is, therefore, focused on preparation of thin-film metallic glasses within the binary Zr–Cu system by non-reactive magnetron co-sputtering. It is the first part of an overall program that is conducted to develop advanced surface coatings with enhanced physical and functional properties based on metallic glasses. Magnetron sputtering is a physical vapor deposition technique with very high cooling rates (higher than 10^6 K/s) utilizing

^{*} Corresponding author.

E-mail address: zemanp@kfy.zcu.cz (P. Zeman).

non-equilibrium discharge plasma for thin-film preparation without the presence of dangerous gas precursors. It is a very suitable technique to prepare Zr–Cu thin-film alloys in a wide composition range. The originality of the paper lies in systematic and detailed investigation of the evolution of the structure, thermal behavior, mechanical, electrical and surface properties of Zr–Cu films with increasing Cu content in a very wide range (~10–90 at.%). Moreover, the properties of the films prepared at low density discharge conditions (conventional magnetron sputtering) are compared with those of the films prepared at high density discharge conditions (high power impulse magnetron sputtering), which generate highly ionized fluxes of Cu atoms with enhanced energies of ions bombarding the growing films [15].

2. Experimental details

Binary Zr–Cu thin-film alloys were deposited by magnetron co-sputtering using an AJA International ATC 2200-V sputter system which was pumped by a turbomolecular pump (1200 l/s) backed up with a multi-stage roots pump (27 m³/hr). The base pressure before each deposition was lower than 5×10^{-5} Pa. Depositions were carried out in argon at a pressure of 0.533 Pa (4 mTorr) using two independent unbalanced magnetrons equipped with circular, indirectly cooled targets (50.8 mm in diameter, 6.35 mm in thickness). The magnetron with the Zr target (99.5% purity, Matsurf Technologies Inc.) was supplied by an Advanced Energy Pinnacle Plus+ 5/5 kW power source working in a DC mode while the magnetron with the Cu target (99.99% purity, Matsurf Technologies Inc.) was supplied by a Hüttinger Elektronik TruPlasma Highpulse 4002 high power pulsed DC power source working in two pulsed modes. The average target power density in a pulse was fixed at 40 W/cm² in case of a film series prepared at low density discharge conditions and at 1000 W/cm² in case of a film series prepared at high density discharge conditions, see Fig. 1. The negative voltage pulse length was set to a constant value of 200 μ s for both film series. All films were deposited onto polished and ultrasonically pre-cleaned single-crystalline Si(100), soda-lime glass and molybdenum substrates held at a floating potential without any external heating. The substrates were rotated above the targets at a speed of 40 rpm and located at a target-to-substrate distance of 150 mm.

The elemental composition of the Zr–Cu film was controlled by adjusting the deposition rate from the Zr and the Cu target independently, particularly by the dc target power and the average target power in period (controlled by the repetition frequency), respectively. Since the sputtering yield of Cu is much higher than that of Zr, operating the Cu target in the pulsed modes allows us to

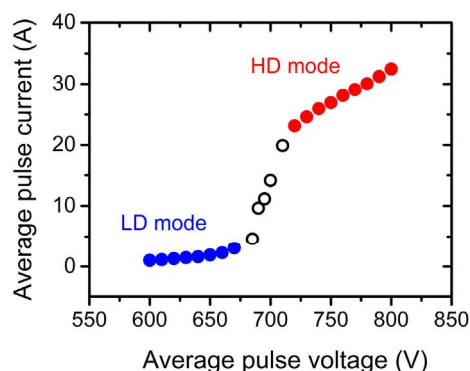


Fig. 1. Current-voltage discharge characteristics for the Cu target. The regions of low density (LD) and high density (HD) discharge conditions are highlighted. In the HD discharge, energetic Cu ions dominate over Ar ions.

precisely control a low Cu content in the films. The deposition rate of Zr and Cu was adjusted before each deposition using a quartz crystal deposition rate monitor (SQM-160, Inficon).

The elemental composition of the films on the Si substrate was analyzed in a scanning electron microscope (SU-70, Hitachi) operated at a primary electron energy of 15 keV using energy dispersive spectroscopy (UltraDry, Thermo Scientific). Zr and Cu standards were used for the quantitative analysis. The error of the elemental analysis was established to be 1 at%.

Thermal behavior of the Zr–Cu films was investigated by differential scanning calorimetry (DSC). Approximately 2 μ m thick films deposited onto the molybdenum thin foils (0.1 mm in thickness) were relatively easily delaminated from this kind of the substrate by its bending. Obtained freestanding film fragments (~3 \times 3 mm² each) of a total mass of 5 mg were then inserted into a 100 μ l alumina crucible covered with a lid. An identical uncharged crucible was used as a reference. The measurements were carried out at the same heating and cooling rate of 30 $^{\circ}$ C/min in flowing argon (1 l/h) in the temperature range from room temperature to 600 $^{\circ}$ C using a DSC system (Labsys DSC 1600, Setaram). The calorimeter was calibrated by melting of Pb, Zn and Al standards with purity of 99.998 \pm 0.001%.

X-ray diffraction (XRD) measurements of the structure of the as-deposited films on the Si substrates and of the freestanding film fragments after their annealing were carried out using a diffractometer (X'Pert PRO, PANalytical) with Cu K α radiation ($\lambda_{Cu} = 0.154187$ nm) working in a slightly asymmetrical Bragg-Brentano geometry with an ω -offset of 1.5 $^{\circ}$ and in the standard Bragg-Brentano geometry, respectively. The ω -offset was used to eliminate a strong reflection of the single-crystalline Si(100) substrate at 69.17 $^{\circ}$ of 2 θ angle. The data were collected using an ultrafast detector X'Celerator in the 2 θ range of 20 $^{\circ}$ –80 $^{\circ}$.

The film thickness and the curvature of the Si substrate coated with the film, from which a residual macrostress was determined using the modified Stoney's formula, were measured by a surface profilometer (Dektak 8 Stylus Profiler, Veeco). The hardness, effective Young's modulus and elastic recovery of the films on the Si substrate were evaluated from the load vs. displacement curves [16], which were measured at room temperature and in ambient environment by a nanoindenter (TI 950 Triboindenter, Hysitron) equipped with the Berkovich-type diamond tip. For each film, a number of indents were made at different loads ranging from 1 to 10 mN and the obtained data were averaged. The ratio of the penetration depth and the film thickness was below 10% in all cases.

The water contact angle of the films on the Si substrate was measured by a drop shape analyzer (DSA30, KRÜSS) using the sessile drop method with a water droplet volume of 2 μ l. The electrical resistivity of the films on the glass substrate was measured at room temperature by a standard four point probe with a spacing of 1.047 mm between the tips (Cylindrical probe, Jandel). The nonconductive glass substrate was used to avoid the effect of an electrically conductive substrate on the data measured. The arithmetic average surface roughness of the films on the Si substrate was evaluated from a selected square area of 2 \times 2 μ m² measured in non-contact mode of an atomic force microscope (SmartSPM, AIST-NT) equipped with a silicon tip (nominal radius of 10 nm).

3. Results and discussion

In the following part, we systematically present and discuss the elemental composition of the Zr–Cu films (Fig. 2) and its effect on their structure (Figs. 3 and 4), thermal behavior (Figs. 5–9), mechanical (Figs. 10 and 11) and surface properties (Figs. 12 and 13),

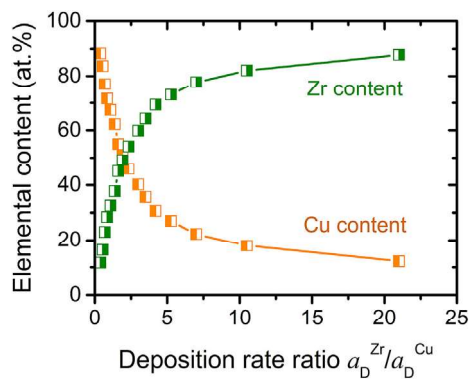


Fig. 2. Elemental composition of Zr–Cu films deposited at the LD conditions as a function of the ratio of the deposition rates $a_D^{\text{Zr}}/a_D^{\text{Cu}}$.

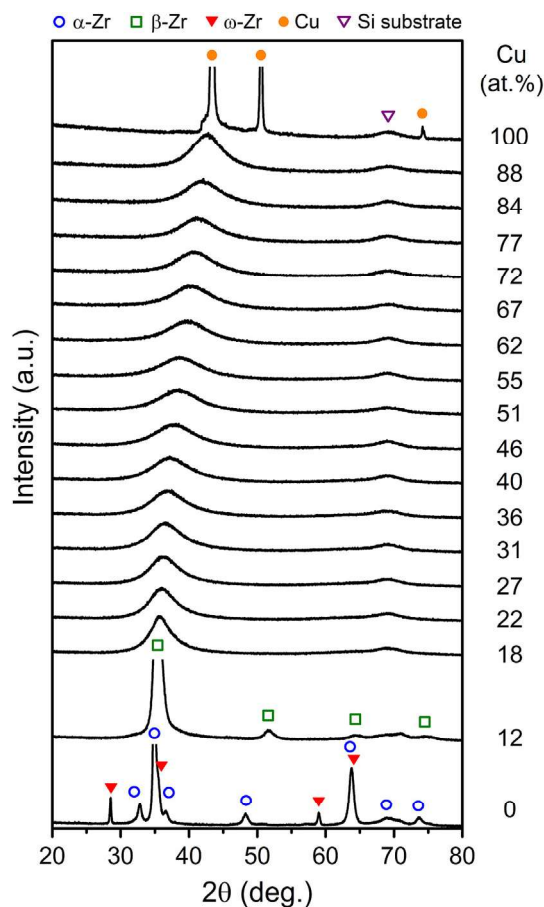


Fig. 3. XRD patterns taken from Zr–Cu films deposited at the LD conditions onto Si(100) substrates. The main diffraction peaks of α -Zr, β -Zr, ω -Zr, Cu and Si substrate are marked.

and electrical resistivity (Fig. 14). The results of the films prepared at the low density discharge (LD) conditions are compared with those of the films prepared at the high density discharge (HD) conditions.

3.1. Elemental composition

The elemental composition of the films was systematically varied by adjusting the deposition rate from the Zr and Cu targets as

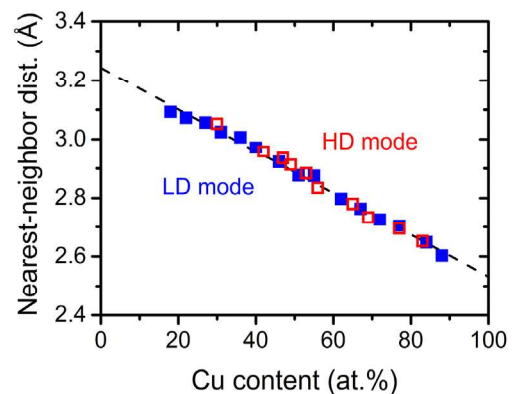


Fig. 4. Calculated nearest-neighbor distance of atoms in X-ray amorphous Zr–Cu films deposited at the LD (full symbols; 18–88 at.% Cu) and HD (open symbols; 30–83 at.% Cu) conditions.

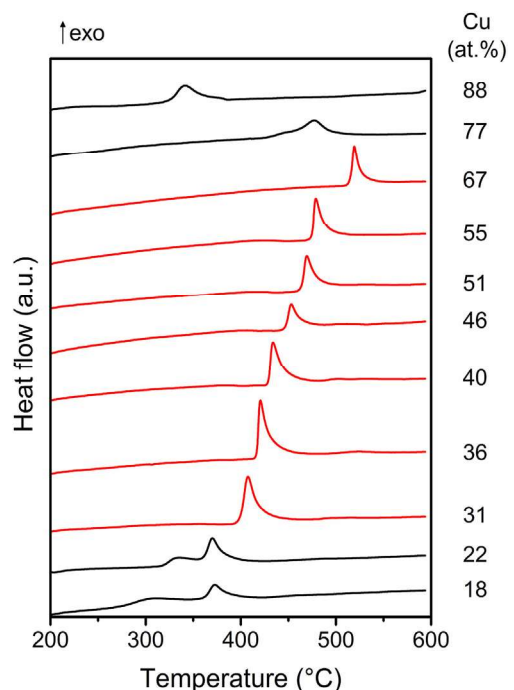


Fig. 5. Selected DSC curves of Zr–Cu films deposited at the LD conditions. Red curves correspond to the films with one, well-defined exothermic peak. Heating rate was 30 °C/min. (For interpretation of the references to colour in this figure legend, the reader is referred to the web version of this article.)

described in Experimental. The total deposition rate of the films increased with increasing Cu content and its values ranged typically between approximately 10 and 30 nm/min. Fig. 2 shows the elemental composition of the films deposited at the LD conditions as a function of the ratio of the deposition rates $a_D^{\text{Zr}}/a_D^{\text{Cu}}$. One may notice that we were able to control the elemental composition thoroughly in a very wide composition range from 12 to 88 at.% Cu. The pure Zr and Cu films serving as reference samples were deposited as well. From Fig. 2 it is clearly seen that by adjusting the ratio $a_D^{\text{Zr}}/a_D^{\text{Cu}}$ to 2 the Zr–Cu films with the identical content of Zr and Cu are prepared. This results from the fact that the molar volume of the Zr atoms (14.02 cm³/mol) is approximately 2 times higher than the molar volume of the Cu atoms (7.09 cm³/mol). That is, a pure as-deposited Cu film contains twice more atoms than a pure as-deposited Zr film of the same thickness. Taking this fact

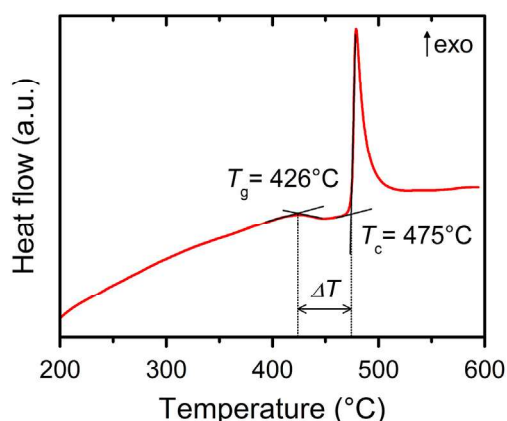


Fig. 6. DSC curve of the $Zr_{45}Cu_{55}$ thin-film metallic glass showing the glass transition and crystallization in detail. The determination of the glass transition temperature T_g , crystallization temperature T_c and supercooled liquid region ΔT is highlighted.

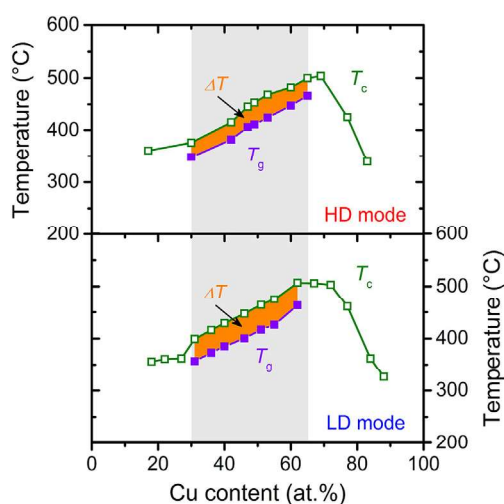


Fig. 7. Glass transition temperature T_g (full symbols), crystallization temperature T_c (open symbols) and supercooled liquid region $\Delta T = T_c - T_g$ (orange area) of the Zr–Cu films deposited at the LD and HD conditions. The grey area represents Zr–Cu thin-film metallic glasses. (For interpretation of the references to colour in this figure legend, the reader is referred to the web version of this article.)

into account we were able to precisely preset (with an error ± 2 at.%) the elemental composition of the films before each deposition at the LD and HD conditions. The elemental compositions of the films deposited at the HD conditions varied between 9 and 83 at.% Cu (not shown).

3.2. Structure

The effect of the elemental composition, represented by the Cu content, on the structure, investigated by XRD, is presented for the films deposited at the LD conditions in Fig. 3. As can be seen, only the films prepared with 0, 12 and 100 at.% Cu exhibit sharp diffraction peaks, which indicates their crystalline structure. An interesting result is the phase composition of the films with 0 and 12 at.% Cu. The XRD pattern of the pure Zr film (0 at.% Cu) is characterized by an occurrence of the diffraction peaks corresponding to hexagonal α -Zr (PDF Card No. 00-05-0665) and ω -Zr (PDF Card No. 04-006-2822) phases. While α -Zr is thermodynamically stable at low temperatures, ω -Zr is known to be a pressure-induced phase [17]. Its occurrence in the film can be therefore attributed to local

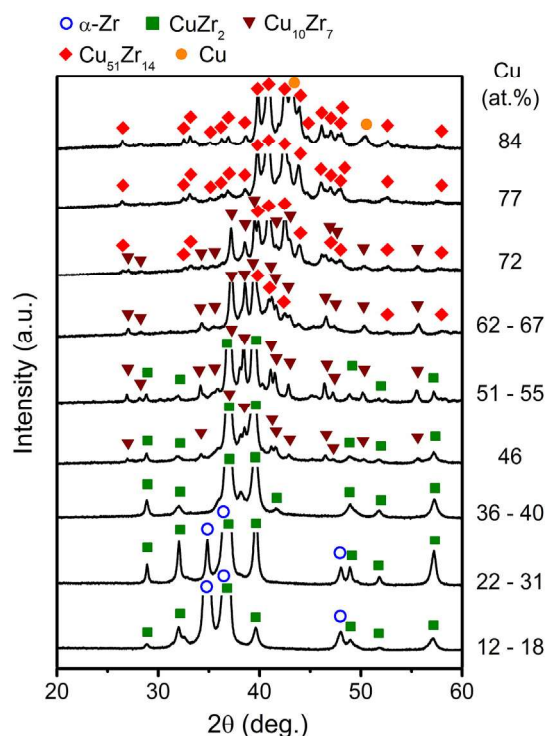


Fig. 8. XRD patterns taken from powdered freestanding fragments of Zr–Cu films (deposited at the LD conditions) after their annealing to 600 °C in argon. XRD patterns were recorded at room temperature. The main diffraction peaks of α -Zr, Cu, $CuZr_2$, $Cu_{10}Zr_7$ a $Cu_{51}Zr_{14}$ are marked.

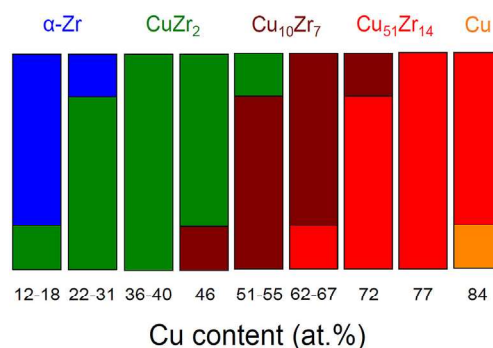


Fig. 9. Schematic diagram of the evolution of the phase composition of Zr–Cu films (annealed to 600 °C in argon) with increasing Cu content. The blue colour corresponds to α -Zr, green colour to $CuZr_2$, brown colour to $Cu_{10}Zr_7$, red colour to $Cu_{51}Zr_{14}$ and orange colour to Cu. (For interpretation of the references to colour in this figure legend, the reader is referred to the web version of this article.)

misfit strains generated in the film during its growth. On the other hand, the Zr–Cu film with 12 at.% Cu exhibits a structure of cubic β -Zr (PDF Card No. 00-34-0657), which is a thermodynamically stable phase at high temperatures (>863 °C). Apreutesei et al. [18] observed the same phase for a Zr–Cu film with 13.4 at.% Cu. We suggest that its stabilization in the film deposited without external heating is a result of a combination of high cooling rates of magnetron sputtering technique (up to 10^6 K/min) and an incorporation of Cu into the lattice of β -Zr. The same stabilization mechanism has been reported in the literature for Ti-based films sputter-deposited at low temperatures [19].

The Zr–Cu films prepared with the Cu content between 18 and 88 at.% are characterized with one, very broad peak in the XRD

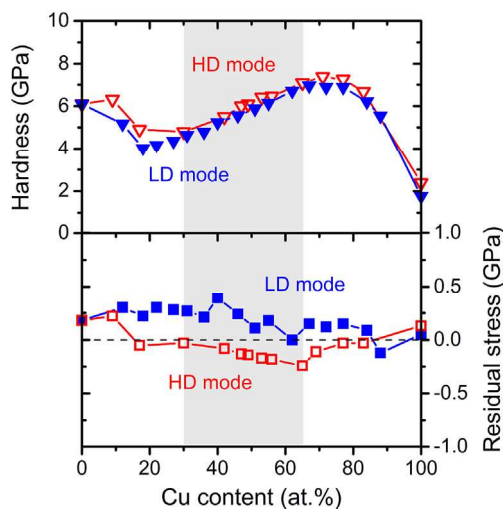


Fig. 10. Hardness and residual stress of the Zr–Cu films deposited at the LD (full symbols) and HD (open symbols) conditions. The grey area represents Zr–Cu thin-film metallic glasses.

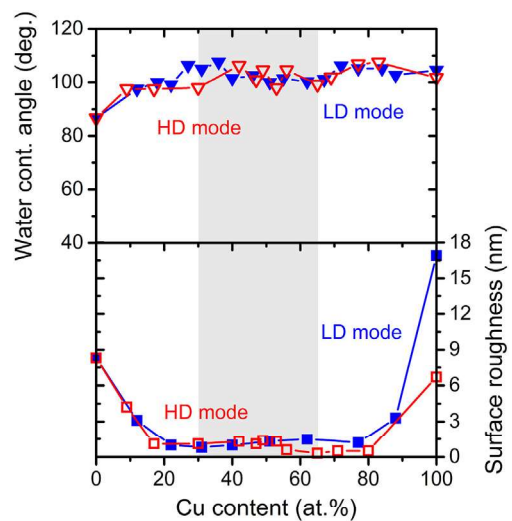


Fig. 12. Water contact angle and surface roughness of the Zr–Cu films deposited at the LD (full symbols) and HD (open symbols) conditions. The grey area represents Zr–Cu thin-film metallic glasses.

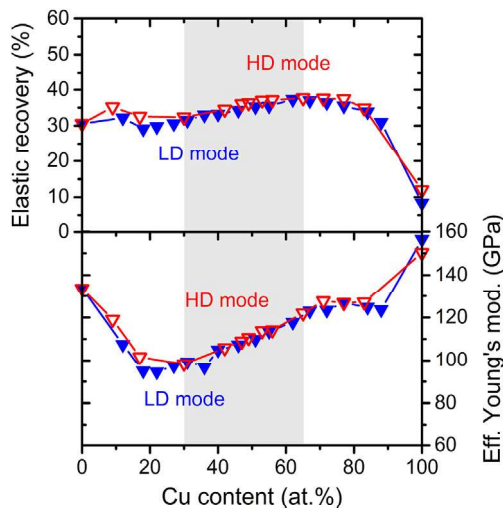


Fig. 11. Elastic recovery and effective Young's modulus of the Zr–Cu films deposited at the LD (full symbols) and HD (open symbols) conditions. The grey area represents Zr–Cu thin-film metallic glasses.

patterns. Its full width at a half maximum is between 4 and 5° and the position of its maximum shifts to higher 2θ angles with increasing Cu content. Such a broad peak with a low intensity arises as a result of X-ray scattering on an atomic or molecular network, which does not exhibit the order over a long distance, e.g., in gases, liquids or amorphous solids [20]. The presence of this peak in the XRD patterns of our films implies that the Zr–Cu films with the Cu content between 18 and 88 at.% are amorphous solids. So far, such very wide composition range has not been reported for amorphous Zr–Cu films prepared by sputtering. Apreutesei et al. [21] observed fully amorphous Zr–Cu films in the range of 33.3–89.1 at.% Cu while Coddet et al. [22] in the range of 25.6–70.4 at.% Cu. Other researchers were able to deposit only crystalline Zr–Cu films composed of separated Zr and Cu phases in these composition ranges [23,24].

Taking the position of the maximum θ_{\max} of the broad peak, we may roughly estimate a typical distance between nearest-neighbor atoms d in the amorphous network of the Zr–Cu films according to

the following formula [25]:

$$d = \frac{1.23 \lambda_{\text{Cu}}}{2 \sin \theta_{\max}}$$

The corresponding values of this distance calculated for the amorphous Zr–Cu films deposited at the LD conditions are plotted in Fig. 4. All values are compared with those corresponding to the amorphous Zr–Cu films deposited at the HD conditions. The films deposited at the HD conditions exhibit a narrower region of amorphization, namely 30–83 at.% Cu, compared to the films deposited at the LD conditions. Deposited particles, especially Cu ions, generated in the HD plasma bring more energy to the growing film, which most likely negatively affects the ability to form amorphous Zr–Cu films. From Fig. 4 it is seen that the nearest-neighbor distance of atoms almost linearly decreases with increasing Cu content. As the Cu content increases, the Cu atoms of a smaller radius (1.28 Å) gradually substitute the Zr atoms of a larger radius (1.60 Å) in the film. Extrapolating the values for the pure Zr and Cu films, we obtain the values almost perfectly fitting the distance of the nearest Zr atoms (3.20 Å) and of the nearest Cu atoms (2.56 Å) in their crystalline lattice. Note that the nearest-neighbor distance corresponds to the position of the first peak in a radial or pair distribution function, which provides the relative probability of finding an atom at a particular distance from a given atom [26,27].

3.3. Thermal behavior

To investigate thermal processes in the Zr–Cu films at elevated temperatures, the films prepared at the LD and HD conditions were annealed in argon up to 600 °C using differential scanning calorimeter. DSC curves of freestanding fragments of selected films deposited at the LD conditions are summarized in Fig. 5. Three characteristic intervals of the Cu content can be recognized. Up to 27 at.% Cu, two exothermic peaks approaching each other are detected on the DSC curves. For the Cu content higher than 67 at.%, two low-intensity exothermic peaks overlapping each other and shifting their positions to lower temperatures with increasing Cu content are observed. Between 31 and 67 at.% Cu, only one exothermic peak is detected. This peak shifts its position to higher temperatures with increasing Cu content. A very similar set of DSC

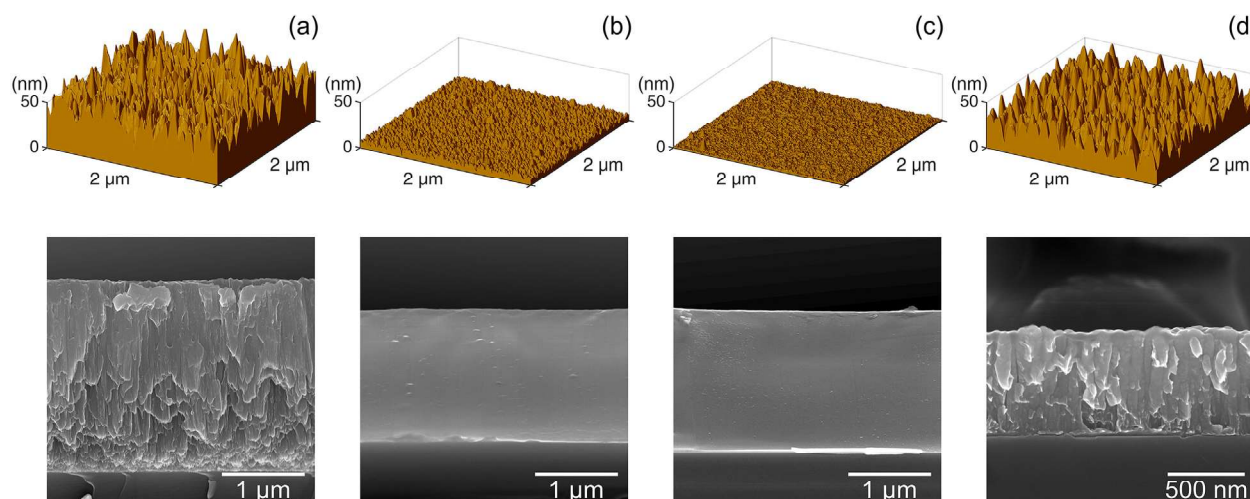


Fig. 13. The surface morphology (AFM images) and the microstructure in cross-section (SEM images) of (a) the pure Zr film, the Zr–Cu films with (b) 49 at.% and (c) 69 at.% Cu and (d) the pure Cu film deposited at the HD conditions.

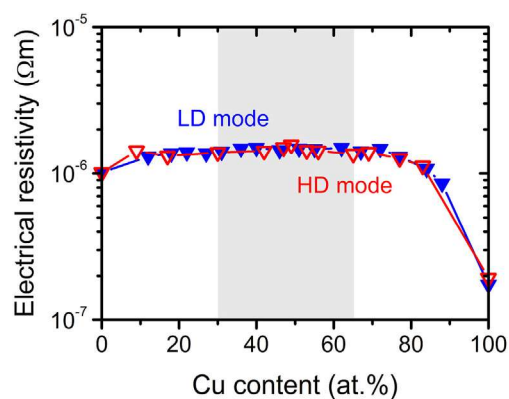


Fig. 14. Electrical resistivity of the Zr–Cu films deposited at the LD (full symbols) and HD (open symbols) conditions. The grey area represents Zr–Cu thin-film metallic glasses.

curves is also observed for the films deposited at the HD conditions (not shown). In this case, only one exothermic peak was observed for the films with the Cu content between 30 and 69 at.%. When a more detailed analysis in the vicinity of this peak is done (see Fig. 6.), one can recognize a decrease of the heat flow before the onset of this exothermic peak. This phenomenon is typical for glasses and is known as the glass transition. The glass transition is a second order transition, which involves a change in the heat capacity but it does not involve a latent heat. Beyond the glass transition temperature, T_g , the glass behaves as the supercooled liquid and exhibits thermoplastic behavior. A further increase of the temperature leads to an onset of crystallization (exothermic process) defined by the crystallization temperature, T_c .

Fig. 7 summarizes the values of T_g and T_c , determined from the intersections of tangents defined in Fig. 6, for the amorphous films deposited at the LD and HD conditions. It is clearly seen that not all amorphous films exhibit the glass transition before crystallization. We were able to unambiguously recognize the glass transition between 31 and 62 at.% Cu for the films deposited at the LD conditions and between 30 and 65 at.% Cu for the films deposited at the HD conditions. These amorphous Zr–Cu films can be therefore considered as metallic glasses. The values of T_g increase with increasing Cu content. As can be seen in Table 1, there are no

Table 1

Glass transition temperature T_g , crystallization temperature T_c and supercooled liquid region $\Delta T = T_c - T_g$ of the Zr–Cu films deposited at the LD and HD conditions.

LD conditions							
Cu (at.%)	31	36	40	46	51	55	62
T_g (°C)	357	373	385	400	417	426	463
T_c (°C)	399	416	429	447	464	475	507
ΔT (°C)	42	43	44	47	47	49	44
HD conditions							
Cu (at.%)	30	–	42	47	49	53	65
T_g (°C)	348	–	382	406	411	424	447
T_c (°C)	376	–	415	445	453	468	482
ΔT (°C)	28	–	33	39	42	44	35

significant differences between these values for both series of the films when taking into account difficulties in the determination of the onset of the glass transition due to low changes in the heat flow, especially for the films with the low (≈ 30 at.%) and high (≈ 65 at.%) Cu contents. The evolution of T_c follows the same trend but above 70 at. % Cu a rapid decrease of T_c is observed. We suggest that this decrease is evidence that the corresponding amorphous Zr–Cu films do not possess a purely glassy-like structure and may contain some nucleation sites facilitating their crystallization at lower temperatures. Comparing the values of T_c for both series of the films (see Table 1), it is obvious that the values are slightly higher for the films deposited at the LD conditions. As a consequence, these films are characterized by a larger supercooled liquid region ΔT (see Table 1). The maximum values of ΔT are measured for the films with the Cu content close to 55 at.% (49 °C and 44 °C for the LD and HD conditions, respectively). It can be therefore concluded that the Zr₄₅Cu₅₅ thin-film metallic alloys deposited at the LD conditions exhibits the highest thermal stability of the supercooled liquid region.

If we compare the above-presented DSC data with those reported in the literature for Zr–Cu melt-spun ribbons [28–33] or magnetron sputtered films [21,34,35], we find a very good agreement in the monotonic or even linear evolution of T_g and T_c within the Cu content where the films possess the glassy-like behavior. Since the values of T_g and T_c are, however, dependent on the heating rate used, it is problematic to make a comparison of their absolute values with those reported in the literature. Moreover, the accuracy

of the determination of T_g is strongly affected by the sharpness of the glass transition on the DSC curve.

After cooling down to room temperature from the maximum temperature of the DSC measurement (600 °C), the film fragments were ground to powders and XRD analysis was employed to identify their phase composition after crystallization. The corresponding XRD patterns for specific ranges of the Cu content are shown in Fig. 8. As clearly seen, all films are well crystallized as expected. Within the Cu range investigated, 3 intermetallics (CuZr_2 – PDF Card No. 00-018-0466, $\text{Cu}_{10}\text{Zr}_7$ – JCPDS Card No. 00-047-1028, $\text{Cu}_{51}\text{Zr}_{14}$ – JCPDS Card No. 00-042-1185) and two metals (α -Zr – PDF Card No. 00-05-0665, Cu – PDF Card No. 00-004-0836) are detected. Their occurrence and relative contents are schematically summarized in Fig. 9 for better illustration. Note that Fig. 9 provides only qualitative information, which phase is predominant (determined from the intensities of the corresponding XRD peaks) for the specific range of the Cu concentration. As a result, we obtained 9 representative phase compositions, which are in accordance with the binary equilibrium phase diagram of Zr–Cu [36]. The most of the Zr–Cu films after heating to 600 °C contain two crystalline phases. We suggest that while the crystallization of two phases in the films with the Cu content between 31 and 67 at% proceeds in a narrow temperature interval (one apparent exothermic peak, see Fig. 5), the crystallization of two phases in the films with the low and high Cu contents proceeds in a much wider temperature interval (two exothermic peaks, see Fig. 5).

3.4. Mechanical properties and residual stress

The effect of the elemental composition and the discharge conditions (LD vs. HD) on the hardness and residual stress of the approximately 2 μm thick Zr–Cu films is shown in Fig. 10. Depending on the Cu content, the hardness of the amorphous Zr–Cu films deposited at the LD and HD conditions monotonically increases from 4.0 to 6.9 GPa and from 4.8 to 7.5 GPa, respectively (see the upper panel of Fig. 10). The maximum values are achieved for the films with the Cu content between 65 and 77 at%. In case of the films deposited at the HD conditions, the maximum hardness is approximately 1.3 and 3 times higher than that for the pure Zr and Cu film, respectively. It can be also noticed that all values of the hardness of the films deposited at the HD conditions are slightly higher than those for the films deposited at the LD conditions. These enhanced values can be explained by the state of the residual stress generated in the films during their growth (see the bottom panel of Fig. 10). In contrast to the films deposited at the LD conditions, all amorphous films deposited at the HD conditions exhibit compressive residual stress with the values varying between -0.05 and -0.25 GPa. In general, a moderate compressive stress is positive since it enhances the hardness (the resistance against the penetration of an indenter) and helps to prevent the crack propagation in a material. The compressive stress in the films deposited at the HD conditions is a result of highly ionized fluxes of Cu atoms with enhanced energies of ions bombarding the growing films. Hence, the deposition of the films at the HD conditions is beneficial from the point of view of hardness and residual stress.

Fig. 11 presents the values of elastic recovery and effective Young's modulus for both series of the Zr–Cu films deposited. It is seen that the evolution of both quantities with increasing Cu content is compatible with that of the hardness. The elastic recovery of the amorphous Zr–Cu films deposited at the LD conditions increases from 28% (at 18 at.% Cu) to 37% (at 62 at.% Cu) and then suddenly decreases (see the upper panel). The lowest elastic recovery is measured for the pure Cu film, which confirms its high ductility. The Zr–Cu films are characterized by a higher elastic recovery than the Cu film but still they are deformed predominantly

plastically when indented. We observed a formation of pile-ups around the indentation imprints. In case of the evolution of effective Young's modulus (see the bottom panel), it is observed a similar trend, i.e., its gradual increase reaching a maximum of about 125 GPa at 77 at.% Cu. This value is lower than the value for the pure Cu film (≈ 150 GPa) indicating a lower stiffness of the Zr–Cu thin-film metallic alloys when elastically deformed. The values of elastic recovery of the Zr–Cu films deposited at the HD conditions are slightly higher but the values of the effective Young's modulus of both film series are very comparable. The above-presented evolution of the hardness and effective Young's modulus with increasing Cu content agree very well with those have been published so far [18,22,33,37,38]. In case of magnetron sputtered Zr–Cu metallic alloys, our films prepared at the HD conditions exhibit, however, the highest absolute values of hardness [18,22].

Comparing the data plotted in Figs. 10 and 11 with those in Fig. 7, one can find a clear correlation of the crystallization temperature and mechanical properties. In general, the crystallization temperature and mechanical properties are closely related to the material structure. Molecular dynamics simulations demonstrated [27,38,39] that the number of the Cu-centered icosahedral clusters in Zr–Cu metallic alloys increases with increasing Cu concentration. Since the atomic packing in these short-range ordered clusters is incompatible with any crystal lattice, the onset of crystallization shifts to higher temperatures and thermal stability of Zr–Cu metallic alloys improves as the Cu content increases. In parallel, a higher concentration of these clusters results in a higher atomic packing density and a lower free volume. As a consequence, mechanical properties such as hardness, Young's modulus, shear modulus and yield strength are enhanced [37,38].

3.5. Surface properties and microstructure

The surface properties (wettability and roughness) of the Zr–Cu films deposited at the LD and HD conditions are presented in Fig. 12. The surface wettability is quantified by the water contact angle measured 3 days after the deposition of each film (see the upper panel of Fig. 12). As can be seen, all Zr–Cu films are characterized by a high water contact angle varying between 98° and 108°. Hence, the Zr–Cu films can be considered as hydrophobic materials. The lowest water contact angle of 87° is measured for the pure Zr film. There is no significant difference between the films deposited at the LD and HD conditions.

The bottom panel of Fig. 12 shows that the amorphous Zr–Cu films exhibit a very low value of the surface roughness (below 1.5 nm), which is significantly lower than the surface roughness of the crystalline films. This is also demonstrated by Fig. 13, which presents images of the surface morphology along with the microstructure in cross-section of the pure Zr film, the Zr–Cu films with 49 and 69 at% Cu and the pure Cu film deposited at the HD conditions. Note that the surface morphology of the Zr–Cu film with 49 at% represents a typical surface morphology of the films with the Cu content between 17 and 53 at%, while the surface morphology of the Zr–Cu film with 70 at% represents a typical surface morphology of the films with the Cu content between 56 and 80 at%. The surface of the Zr–Cu thin-film metallic alloys is very smooth because no columnar microstructure develops during the film growth. From the bottom panel of Fig. 12 is also seen that the films deposited at the HD conditions exhibit a smoother surface if the Cu content is higher than 50 at%. This shows that enhanced energies of Cu ions generated at the HD conditions have an impact on the surface roughness only if a sufficient amount of Cu ions take part in a bombardment of the surface and the film growth. As expected, the effect is most pronounced for the pure Cu films, see a big difference in the surface roughness for 100 at.% Cu.

3.6. Electrical resistivity

Fig. 14 presents the room-temperature electrical resistivity of the Zr–Cu films deposited at the LD and HD conditions. It is seen that there is no dependence of the electrical resistivity on the Cu content over a wide composition range. All films are highly electrically conductive with an average value of $1.4 \times 10^{-6} \Omega\text{m}$. This value is approximately 1.4 and 8 times higher than that for the pure Zr and Cu film, respectively. One can expect that the electrical resistivity of the amorphous Zr–Cu films will be higher than that of their crystalline counterparts with the same elemental composition due to their disordered structure on long distance resulting in a higher electron scattering and shorter mean free electron path [40]. From Fig. 14 it is also obvious that there is no significant effect of the deposition conditions (LD vs. HD) on the electrical resistivity.

4. Conclusions

Conventional dc and impulse magnetron co-sputtering of Zr and Cu in pure argon was proved to be a suitable deposition technique for a reproducible preparation of Zr–Cu thin-film metallic glasses with a variety of promising properties.

Zr–Cu thin films with an amorphous structure were prepared in a very wide range of the Cu content (18–88 at.%) when the deposition was employed at the low density discharge conditions. The glass transition was unambiguously recognized for the films with the Cu content between approximately 30 and 65 at.% Cu independently of the low or high density discharge conditions used. The glass transition temperature increased gradually with increasing Cu content and the maximum of the supercooled liquid region was achieved for approximately 55 at.% Cu. A clear correlation between the evolution of the crystallization temperature and mechanical properties with increasing Cu content was observed. The deposition at the high density discharge conditions resulted in a preparation of the Zr–Cu thin-film metallic alloys with a compressive stress (<0 GPa), an enhanced hardness (>7 GPa), very smooth (surface roughness <1 nm) and hydrophobic (water contact angle $>100^\circ$) surface.

Acknowledgments

The authors thank Dr. Jiří Čapek for a helpful and stimulating discussion, Dr. Jiří Rezek for the measurements of the surface roughness and Dr. Stanislav Haviar for the measurement of the elemental composition and microstructure. This work was supported by the Czech Science Foundation under Project No. GA16-18183S.

References

- [1] H.W. Sheng, W.K. Luo, F.M. Alamgir, J.M. Bai, E. Ma, Atomic packing and short-to-medium-range order in metallic glasses, *Nature* 439 (2006) 419–425, <http://dx.doi.org/10.1038/nature04421>.
- [2] A.R. Yavari, Materials science: a new order for metallic glasses, *Nature* 439 (2006) 405–406, <http://dx.doi.org/10.1038/439405a>.
- [3] N. Mattern, P. Jovári, I. Kaban, S. Gruner, A. Elsner, V. Kokotin, et al., Short-range order of Cu–Zr metallic glasses, *J. Alloys Compd.* 485 (2009) 163–169, <http://dx.doi.org/10.1016/j.jallcom.2009.05.111>.
- [4] D.Z. Chen, C.Y. Shi, Q. An, Q. Zeng, W.L. Mao, W.A. Goddard, et al., Fractal atomic-level percolation in metallic glasses, *Science* 349 (2015) 1306–1310, <http://dx.doi.org/10.1126/science.1233>.
- [5] G.A. Almyras, C.E. Lekka, N. Mattern, G.A. Evangelakis, On the microstructure of the $\text{Cu}_{65}\text{Zr}_{35}$ and $\text{Cu}_{35}\text{Zr}_{65}$ metallic glasses, *Scr. Mater.* 62 (2010) 33–36, <http://dx.doi.org/10.1016/j.scriptamat.2009.09.019>.
- [6] J. Zemp, M. Celino, B. Schönfeld, J.F. Löffler, Icosahedral superclusters in $\text{Cu}_{64}\text{Zr}_{36}$ metallic glass, *Phys. Rev. B* 90 (2014) 144108, <http://dx.doi.org/10.1103/PhysRevB.90.144108>.
- [7] M. Telford, The case for bulk metallic glass, *Mater. Today* 7 (2004) 36–43, [http://dx.doi.org/10.1016/S1369-7021\(04\)00124-5](http://dx.doi.org/10.1016/S1369-7021(04)00124-5).
- [8] M.F. Ashby, A.L. Greer, Metallic glasses as structural materials, *Scr. Mater.* 54 (2006) 321–326, <http://dx.doi.org/10.1016/j.scriptamat.2005.09.051>.
- [9] A.L. Greer, Metallic glasses... on the threshold, *Mater. Today* 12 (2009) 14–22, [http://dx.doi.org/10.1016/S1369-7021\(09\)70037-9](http://dx.doi.org/10.1016/S1369-7021(09)70037-9).
- [10] J. Schroers, G. Kumar, T.M. Hodges, S. Chan, T.R. Kyriakides, Bulk metallic glasses for biomedical applications, *JOM* 61 (2009) 21–29, <http://dx.doi.org/10.1007/s11837-009-0128-1>.
- [11] L.A. Davis, Fracture toughnesses of metallic glasses, *Metall. Trans. A* 10 (1979) 235–240, <http://dx.doi.org/10.1007/BF02817633>.
- [12] R.D. Conner, Y. Li, W.D. Nix, W.L. Johnson, Shear band spacing under bending of Zr-based metallic glass plates, *Acta Mater.* 52 (2004) 2429–2434, <http://dx.doi.org/10.1016/j.actamat.2004.01.034>.
- [13] D. Jang, J.R. Greer, Transition from a strong-yet-brittle to a stronger-and-ductile state by size reduction of metallic glasses, *Nat. Mater.* 9 (2010) 1–5, <http://dx.doi.org/10.1038/nmat2622>.
- [14] M. Ghidelli, A. Volland, J.-J. Blandin, T. Pardoën, J.-P. Raskin, F. Mompou, et al., Exploring the mechanical size effects in $\text{Zr}_{65}\text{Ni}_{35}$ thin film metallic glasses, *J. Alloys Compd.* 615 (2014) S90–S92, <http://dx.doi.org/10.1016/j.jallcom.2013.11.154>.
- [15] J. Capek, M. Hala, O. Zabeida, J.E. Klemborg-Sapieha, L. Martinu, Steady state discharge optimization in high-power impulse magnetron sputtering through the control of the magnetic field, *J. Appl. Phys.* 111 (2012) 23301, <http://dx.doi.org/10.1063/1.3673871>.
- [16] W.C. Oliver, G.M. Pharr, An improved technique for determining hardness and elastic modulus using load and displacement sensing indentation experiments, *J. Mater. Res.* 7 (1992) 1564–1583, <http://dx.doi.org/10.1557/JMR.1992.1564>.
- [17] W. Liu, B. Li, L. Wang, J. Zhang, Y. Zhao, Simultaneous ultrasonic and synchrotron x-ray studies on pressure induced α - ω phase transition in zirconium, *J. Appl. Phys.* 104 (2008) 76102, <http://dx.doi.org/10.1063/1.2987001>.
- [18] M. Apreutesei, P. Steyer, L. Joly-Pottuz, A. Billard, J. Qiao, S. Cardinal, et al., Microstructural, thermal and mechanical behavior of co-sputtered binary Zr–Cu thin film metallic glasses, *Thin Solid Films* 561 (2014) 53–59, <http://dx.doi.org/10.1016/j.tsf.2013.05.177>.
- [19] J. Musil, A.J. Bell, J. Vlček, T. Hurkmans, Formation of high temperature phases in sputter deposited Ti-based films below 100°C , *J. Vac. Sci. Technol. A* 14 (1996) 2247–2250, <http://dx.doi.org/10.1116/1.580055>.
- [20] A. Guinier, X-ray Diffraction in Crystals, Imperfect Crystals, and Amorphous Bodies, W. H. Freeman and Company, 1963, <http://dx.doi.org/10.1021/ja01079a041>.
- [21] M. Apreutesei, P. Steyer, A. Billard, L. Joly-Pottuz, C. Esnouf, Zr–Cu thin film metallic glasses: an assessment of the thermal stability and phases' transformation mechanisms, *J. Alloys Compd.* 619 (2015) 284–292, <http://dx.doi.org/10.1016/j.jallcom.2014.08.253>.
- [22] P. Coddet, F. Sanchette, J.C. Rousset, O. Rapaud, C. Coddet, On the elastic modulus and hardness of co-sputtered Zr–Cu–(N) thin metal glass films, *Surf. Coat. Technol.* 206 (2012) 3567–3571, <http://dx.doi.org/10.1016/j.surfcoat.2012.02.036>.
- [23] O. Jimenez, M. Audronis, M.A. Baker, A. Matthews, A. Leyland, Structure and mechanical properties of nitrogen-containing Zr–Cu based thin films deposited by pulsed magnetron sputtering, *J. Phys. D: Appl. Phys.* 41 (2008) 155301, <http://dx.doi.org/10.1088/0022-3727/41/15/155301>.
- [24] J. Qin, X. Yong, Z. Xin-Yu, L. Gong, L. Li-Xin, X. Zhe, et al., Zr–Cu amorphous films prepared by magnetron Co-sputtering deposition of pure Zr and Cu, *Chin. Phys. Lett.* 26 (2009) 86109, <http://dx.doi.org/10.1088/0256-307X/26/8/086109>.
- [25] C.O. Kim, W.L. Johnson, Amorphous phase separation in the metallic glasses $(\text{Pb}_{1-y}\text{Sb}_y)_1-x\text{Au}_x$, *Phys. Rev. B* 23 (1981) 143–147, <http://dx.doi.org/10.1103/PhysRevB.23.143>.
- [26] J.L. Joel, I. Gersten, F.W. Frederick, W. Smith, *The Physics and Chemistry of Materials*, Wiley, 2001.
- [27] A.E. Lagogianni, G. Almyras, C.E. Lekka, D.G. Papageorgiou, G.A. Evangelakis, Structural characteristics of $\text{Cu}_x\text{Zr}_{100-x}$ metallic glasses by molecular dynamics simulations, *J. Alloys Compd.* 483 (2009) 658–661, <http://dx.doi.org/10.1016/j.jallcom.2008.07.211>.
- [28] A.J. Kerns, D.E. Polk, R. Ray, B.C. Giessen, Thermal behavior of Zr–Cu metallic glasses, *Mater. Sci. Eng.* 38 (1979) 49–53, [http://dx.doi.org/10.1016/0025-5416\(79\)90031-4](http://dx.doi.org/10.1016/0025-5416(79)90031-4).
- [29] K.H.J. Buschow, Thermal stability of amorphous Zr–Cu alloys, *J. Appl. Phys.* 52 (1981) 3319–3323, <http://dx.doi.org/10.1063/1.329152>.
- [30] Z. Altounian, T. Guo-hua, J.O. Strom-Olsen, Crystallization characteristics of Cu–Zr metallic glasses from $\text{Cu}_{70}\text{Zr}_{30}$ to $\text{Cu}_{25}\text{Zr}_{75}$, *J. Appl. Phys.* 53 (1982) 4755, <http://dx.doi.org/10.1063/1.331304>.
- [31] Y. Calvayrac, J.P. Chevalier, M. Harmelin, A. Quivy, J. Bigot, On the stability and structure of Cu–Zr based glasses, *Philos. Mag. Part B* 48 (1983) 323–332, <http://dx.doi.org/10.1080/13642818308246485>.
- [32] N. Mattern, A. Schöps, U. Kühn, J. Acker, O. Khvostikova, J. Eckert, Structural behavior of $\text{Cu}_x\text{Zr}_{100-x}$ metallic glass ($x=35-70$), *J. Non. Cryst. Solids* 354 (2008) 1054–1060, <http://dx.doi.org/10.1016/j.jnoncrysol.2007.08.035>.
- [33] B.F. Lu, J.F. Li, L.T. Kong, Y.H. Zhou, Correlation between mechanical behavior and glass forming ability of Zr–Cu metallic glasses, *Intermetallics* 19 (2011) 1032–1035, <http://dx.doi.org/10.1016/j.intermet.2011.03.009>.
- [34] J. Sakurai, S. Hata, A. Shimokohbe, Characteristics of Cu–Zr thin film metallic glasses fabricated using a carousel-type sputtering system, *Jpn. J. Appl. Phys.* 48 (2009) 25503, <http://dx.doi.org/10.1143/JJAP.48.025503>.

- [35] F. Zougmore, J.C. Lasjaunias, O. Béthoux, Low-temperature thermodynamic properties of amorphous sputtered $Zr_{100-x}Cu_x$ alloys. Effect of structural relaxation, *J. Phys.* 50 (1989) 1241–1265, <http://dx.doi.org/10.1051/jphys:0198900500100124100>.
- [36] T.B. Massalski, J.L. Murray, L.H. Bennett, H. Baker, L. Kacprzak, *Binary Alloy Phase Diagrams*, American Society for Metals, Ohio, 1986.
- [37] K.-W. Park, J. Jang, M. Wakeda, Y. Shibutani, J.-C. Lee, Atomic packing density and its influence on the properties of Cu–Zr amorphous alloys, *Scr. Mater* 57 (2007) 805–808, <http://dx.doi.org/10.1016/j.scriptamat.2007.07.019>.
- [38] M. Wakeda, Y. Shibutani, S. Ogata, J. Park, Relationship between local geometrical factors and mechanical properties for Cu–Zr amorphous alloys, *Intermetallics* 15 (2007) 139–144, <http://dx.doi.org/10.1016/j.intermet.2006.04.002>.
- [39] Y.Q. Cheng, H.W. Sheng, E. Ma, Relationship between structure, dynamics, and mechanical properties in metallic glass-forming alloys, *Phys. Rev. B* 78 (2008) 14207, <http://dx.doi.org/10.1103/PhysRevB.78.014207>.
- [40] H. Turnow, H. Wendrock, S. Menzel, T. Gemming, J. Eckert, Structure and properties of sputter deposited crystalline and amorphous Cu–Ti films, *Thin Solid Films* 598 (2016) 184–188, <http://dx.doi.org/10.1016/j.tsf.2015.10.081>.

Part B

Tuning properties and behavior of magnetron sputtered Zr–Hf–Cu metallic glasses

M. Zítek, P. Zeman, Š. Zuzjaková, M. Kotrlová, R. Čerstvý
Journal of Alloys and Compounds 739 (2018) 848–855



Tuning properties and behavior of magnetron sputtered Zr-Hf-Cu metallic glasses



M. Zítek, P. Zeman*, Š. Zuzjaková, M. Kotrlová, R. Čerstvý

Department of Physics and NTIS - European Centre of Excellence, University of West Bohemia, Univerzitní 8, 306 14 Plzeň, Czech Republic

ARTICLE INFO

Article history:

Received 25 July 2017

Received in revised form

15 December 2017

Accepted 25 December 2017

Available online 28 December 2017

Keywords:

Zr-Hf-Cu

Amorphous material

Metallic glasses

Thin films

Magnetron sputtering

ABSTRACT

Amorphous ternary Zr-Hf-Cu thin-film alloys with glass-like behavior were deposited by non-reactive conventional dc and high-power impulse magnetron co-sputtering using three unbalanced magnetrons equipped with Zr, Hf and Cu targets. The Zr and Hf targets were operated in a dc regime while the Cu target in a high power impulse regime. Two series of films with a gradually increasing Hf/(Hf+Zr) ratio at 46 at.% Cu and 59 at.% Cu were deposited. The effect of the elemental composition on the structure, thermal behavior, mechanical and surface properties, electrical resistivity and oxidation resistance was systematically investigated. We found a clear correlation among the evolution of the glass transition temperature, crystallization temperature, hardness and effective Young's modulus with increasing Hf/(Hf+Zr) ratio. A linear increase of these quantities is attributed to an increase of the average bond energy in the films as Hf gradually substitutes Zr. The Zr-Hf-Cu thin-film metallic glasses exhibit enhanced hardness (up to 7.8 GPa), enhanced thermal stability and oxidation resistance, very smooth (surface roughness down to 0.2 nm) and hydrophobic surface (water contact angle up to 109°), and very low electrical resistivity (lower than $1.9 \times 10^{-6} \Omega\text{m}$).

© 2017 Elsevier B.V. All rights reserved.

1. Introduction

Metallic glasses (amorphous metallic alloys) have received remarkable attention in the past years because of their unique properties including high yield strength, high elastic strain and hardness, high magnetic permeability, temperature-independent electrical resistivity, low wear and high corrosion resistance, excellent surface finishing, and biocompatibility [1–4]. These properties result from their disordered atomic structure without grain boundaries. Recently, molecular dynamics simulations have revealed that the arrangement of atoms in metallic glasses is not completely random but a short- or medium-range ordering based on different types of polyhedral clusters exists on the atomic scale [5–8]. In fact, most of the atoms are arranged in icosahedral clusters having the highest coordination number and thus the highest atomic packing density among others.

Binary Zr–Cu thin-film metallic alloys have been extensively studied during past years [9–11]. The results demonstrated a good glass forming ability in a wide range of the elemental composition.

In addition, the Zr–Cu thin-film metallic glasses exhibit a high hardness (up to 7.2 GPa), a high crystallization temperature (up to 500 °C) and a wide super-cooled liquid region (up to 71 °C). Further improvement of the mechanical and thermal properties and glass forming ability may be achieved by addition of a third element into the binary Zr–Cu metallic glasses. Several ternary Zr–Cu based metallic glasses have been synthesized [12–16]. For instance, an optimized addition of Al into Zr–Cu metallic glasses improves the hardness and the thermal stability [15] while an incorporation of Mo reduces the average friction coefficient without changing mechanical properties [14]. The addition of Hf has been studied primarily theoretically focusing on the glass forming ability in the Zr-Hf-Cu ternary system [17,18]. The calculations showed that the Zr-Hf-Cu ternary system may allow us to form metallic glasses in a wide composition range. In addition, Luo et al. found that metallic glasses with the composition around $\text{Cu}_{55}\text{Zr}_{10}\text{Hf}_{35}$ are more stable than other alloys in the system [18]. Experimentally, only Basu et al. prepared ternary $\text{Cu}_{50}\text{Zr}_{25}\text{Hf}_{25}$ glassy ribbons by the single roller melt-spinning technique [12]. There is no other experimental study dealing with systematic investigation of an addition of Hf into Zr–Cu metallic glasses is missing.

The present study is therefore focused on preparation of ternary Zr-Hf-Cu thin-film metallic glasses with various compositions and

* Corresponding author.

E-mail address: zemanp@kfy.zcu.cz (P. Zeman).

investigation of their properties and thermal behavior in detail. The preparation process builds on our previous work dealing with the binary Zr–Cu thin-film alloys [11]. A gradual incorporation of Hf (with more covalent character of bonds and much higher atomic mass than Zr) into binary Zr–Cu films is supposed to enhance and tune mechanical properties, thermal stability and oxidation resistance of the glassy state, and thus extend application potential of thin-film metallic glasses to high temperatures.

The Zr–Hf–Cu films are deposited by magnetron co-sputtering, which is a suitable deposition technique for preparation of metallic glasses mainly due to high cooling rates of the vapor on the substrate. The configuration with three independent magnetrons with Zr, Hf and Cu sputtering targets allows us to precisely control the elemental composition in a wide range. In this paper, we present correlations among the elemental composition and the structure, thermal behavior, mechanical and surface properties, and electrical resistivity of Zr–Hf–Cu thin-film metallic alloys in detail.

2. Experimental details

Ternary Zr–Hf–Cu thin-film alloys were deposited by magnetron co-sputtering using an AJA International ATC 2200–V sputter system which was pumped by a turbomolecular pump (1200 l/s) backed up with a multi-stage roots pump (27 m³/hr). The base pressure before each deposition was lower than 5×10^{-5} Pa. Depositions were carried out in argon at a pressure of 0.533 Pa (4 mTorr) using three independent unbalanced magnetrons equipped with circular, indirectly cooled targets (50.8 mm in diameter, 6.35 mm in thickness). The magnetrons with the Zr target (99.5% purity, Matsurf Technologies Inc.) and the Hf target (99.9% purity, Plasmaterials Inc.) were powered by a dual power supply (Pinnacle Plus+ 5/5 kW, Advanced Energy) working independently in two dc modes while the magnetron with the Cu target (99.99% purity, Matsurf Technologies Inc.) was powered by a pulsed dc power supply (TruPlasma Highpulse 4002, Hüttinger Elektronik) working in a high power impulse mode. The average target power density in a pulse was fixed at 1000 W/cm². The negative voltage pulse length was set to a constant value of 200 μ s. All films were deposited onto polished and ultrasonically pre-cleaned single-crystalline Si(100), soda-lime glass and molybdenum substrates held at a floating potential without any external heating. The substrates were rotated above the targets at a speed of 40 rpm and located at a target-to-substrate distance of 150 mm.

The elemental composition of the Zr–Hf–Cu films was controlled by adjusting the deposition rates from the Zr, Hf and Cu targets independently, particularly by the dc target powers (Zr and Hf) and the average target power in a period (Cu). The deposition rates were measured before each deposition using a quartz crystal deposition rate monitor (SQM-160, Inficon).

The elemental composition of the as-deposited films on the Si substrate was analyzed in a scanning electron microscope (SU-70, Hitachi) operated at a primary electron energy of 20 keV using energy dispersive spectroscopy (UltraDry, Thermo Scientific). Zr, Hf and Cu standards were used for the quantitative analysis. The error of the elemental analysis was established to be 1 at.%.

The thermal behavior of the films was investigated by differential scanning calorimetry (DSC). Approximately 2 μ m thick films deposited onto the molybdenum thin foils (0.1 mm in thickness) were relatively easily delaminated from this kind of the substrate by its bending. Obtained freestanding film fragments ($\sim 3 \times 3$ mm² each) of a total mass of 5 mg were then inserted into a 100 μ l alumina crucible covered with a lid. An identical uncharged crucible was used as a reference. The measurements were carried out at the same heating and cooling rate of 30 °C/min in flowing argon

(1 l/h) in the temperature range from room temperature to 600 °C using a DSC system (Labsys DSC 1600, Setaram). The calorimeter was calibrated by melting of Pb, Zn and Al standards with purity of $99.998 \pm 0.001\%$.

X-ray diffraction (XRD) measurements of the structure of the as-deposited films on the Si substrates and of the powdered film fragments after their annealing were carried out using a diffractometer (X'Pert PRO, PANalytical) with Cu K_α radiation ($\lambda_{Cu} = 0.154187$ nm) working in a slightly asymmetrical Bragg–Brentano geometry with an ω -offset of 1.5° and in the standard Bragg–Brentano geometry, respectively. The ω -offset was used to eliminate a strong reflection of the single-crystalline Si(100) substrate at 2θ angle of 69.17°. The data were collected using an ultrafast detector X'Celerator in the 2θ range of 20°–60°.

The film thickness and the curvature of the Si substrate coated with the film, from which a residual macrostress was determined using the modified Stoney's formula, were measured by a surface profilometer (Dektak 8 Stylus Profiler, Veeco). The hardness, effective Young's modulus and elastic recovery of the films on the Si substrate were evaluated from the load vs. displacement curves [19], which were measured at room temperature and in ambient environment by a nanoindenter (TI 950 Triboindenter, Hysitron) equipped with a Berkovich-type diamond tip. For each film, a number of indents were made at different loads ranging from 1 to 10 mN and the obtained data were averaged. The ratio of the penetration depth and the film thickness was below 10% in all cases.

The water contact angle of the films on the Si substrate was measured by a drop shape analyzer (DSA30, KRÜSS) using the sessile drop method with a water droplet volume of 2 μ l. The electrical resistivity of the films on the glass substrate was measured at room temperature by a standard four point probe with a spacing of 1.047 mm between the tips (Cylindrical probe, Jandel). The nonconductive glass substrate was used to avoid the effect of an electrically conductive substrate on the data measured. The arithmetic average surface roughness of the films on the Si substrate was evaluated from a selected square area of 2×2 μ m² measured in non-contact mode of an atomic force microscope (SmartSPM, AIST-NT) equipped with a silicon tip (nominal radius of 10 nm).

The oxidation resistance of the films was investigated by thermogravimetry (TG) using a symmetrical high resolution system (Setaram TAG 2400). The TG analysis was carried out in synthetic atmospheric air (flow rate of 1 l/h) with dynamic heating in the temperature range from room temperature up to 1000 °C. The heating and cooling rates were set to 10 and 30 °C/min, respectively. The Si substrates were coated only on one side. After subtracting the thermogravimetric signal corresponding to oxidation of the uncoated sides, the resulting thermogravimetric curve is related to the oxidation resistance of the Zr–Hf–Cu film only.

3. Results and discussion

In this section, the effect of a gradual substitution of Hf for Zr on the properties of the Zr–Hf–Cu thin-film alloys is presented. We compare and discuss the results from two film series with an approximately constant value of the Cu content. The first series with approximately 46 at.% Cu is denoted as Cu-poor from now on while the second series with approximately 59 at.% Cu as Cu-rich. First of all, we show the elemental composition of both film series (Fig. 1). Then, we study the effect of the Hf/(Hf+Zr) ratio on the film structure (Fig. 2), thermal behavior (Figs. 3–6), mechanical (Figs. 7 and 8) and surface properties (Fig. 9), electrical resistivity (Fig. 10) and oxidation resistance (Fig. 11).

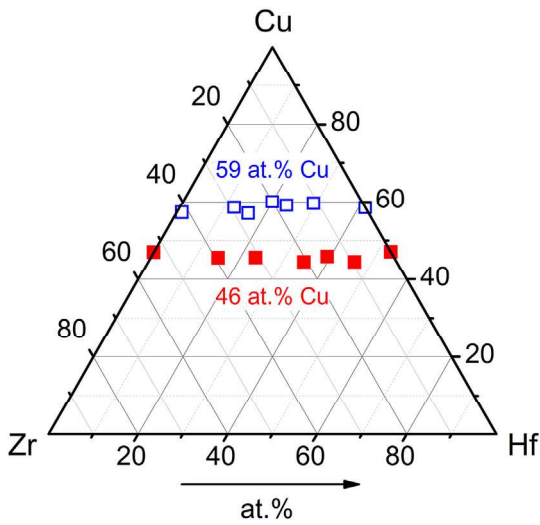


Fig. 1. Elemental composition of Zr-Hf-Cu films of Cu-poor (46 at.% Cu) and Cu-rich (59 at.% Cu) series.

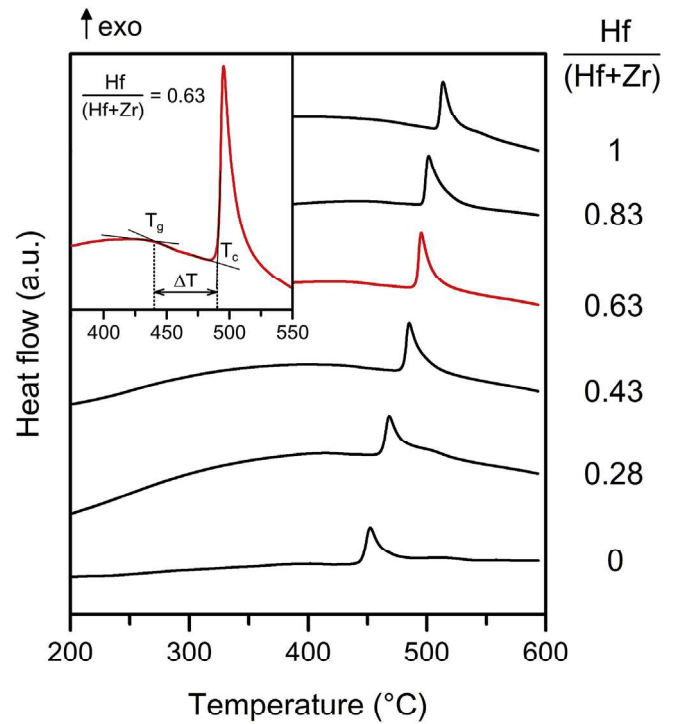


Fig. 3. DSC curves of Zr-Hf-Cu films of a Cu-poor (46 at.% Cu) series. Heating rate was 30 °C/min. The inset shows the glass transition temperature T_g , the crystallization temperature T_c and the super-cooled liquid region $\Delta T = T_c - T_g$ for the Zr-Hf-Cu film with $Hf/(Hf+Zr) = 0.63$.

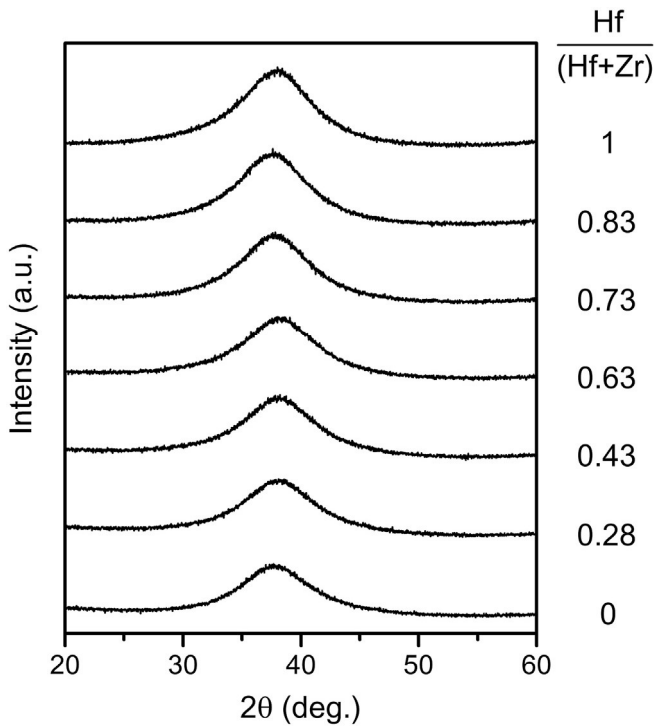


Fig. 2. XRD patterns taken from as-deposited Zr-Hf-Cu films of a Cu-poor (46 at.% Cu) series.

3.1. Elemental composition

The elemental composition of the Zr-Hf-Cu films, shown in the ternary plot in Fig. 1, was varied by adjusting the deposition rate from the Zr, Hf and Cu targets as described in Experimental details. The total deposition rate varied from 15 to 19 nm/min for the Cu-poor series and from 17 to 22 nm/min for the Cu-rich series. In both series, we started the depositions with the binary Zr–Cu films, proceeding through the ternary Zr-Hf-Cu films while increasing the $Hf/(Hf+Zr)$ ratio and ending up with the binary Hf–Cu films. To achieve, for instance, an elemental composition of $Zr_{25}Hf_{25}Cu_{50}$ (in

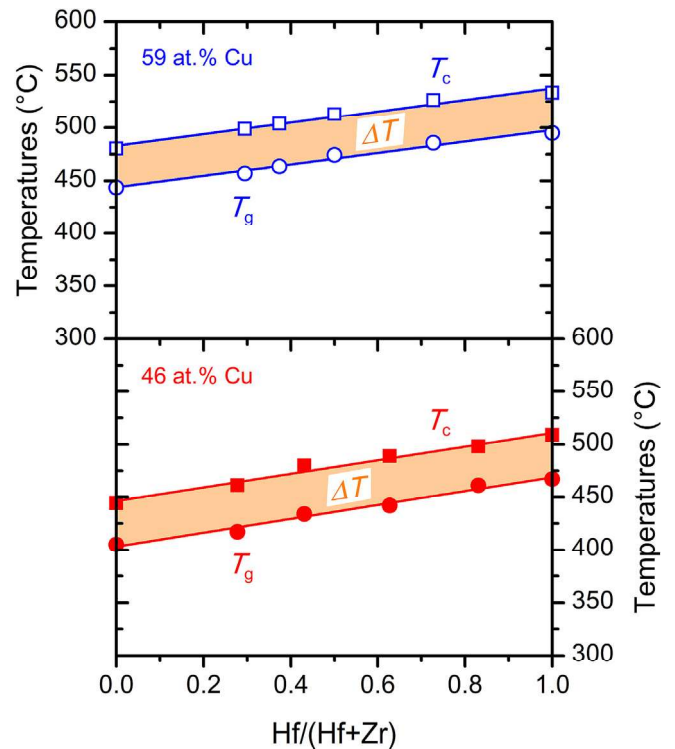


Fig. 4. Crystallization temperature T_c (square symbols), glass transition temperature T_g (circle symbols) and supercooled liquid region $\Delta T = T_c - T_g$ (orange area) of Zr-Hf-Cu films of Cu-poor (46 at.% Cu) and Cu-rich (59 at.% Cu) series. (For interpretation of the references to colour in this figure legend, the reader is referred to the web version of this article.)

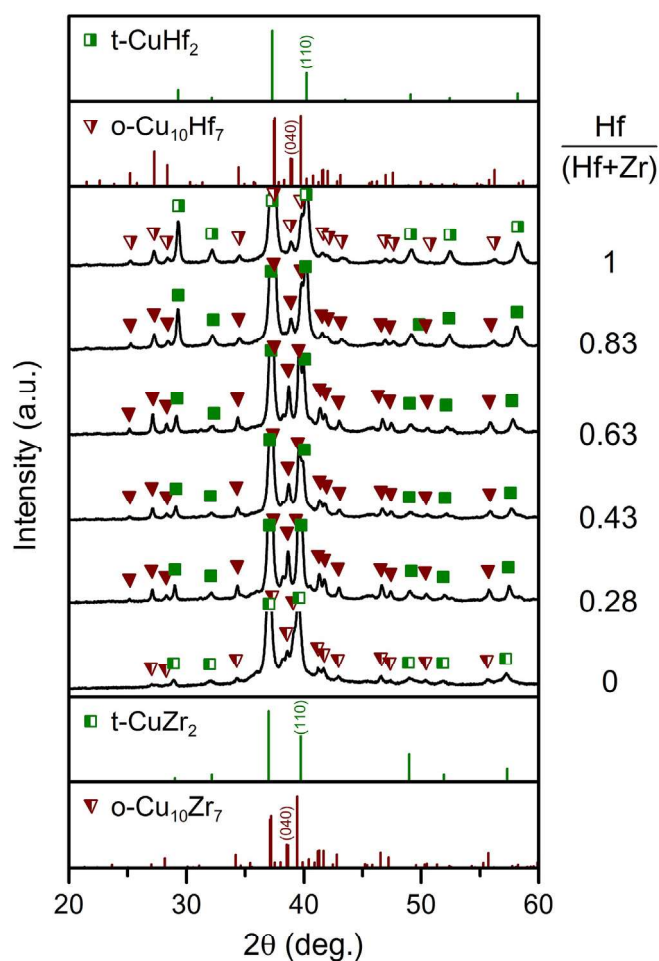


Fig. 5. XRD patterns taken from powdered fragments of Zr-Hf-Cu films of a Cu-poor (46 at.% Cu) series after their annealing to 600 °C in argon. XRD patterns were recorded at room temperature. The half-open symbols correspond to the powder diffraction standards of binary phases listed in the figure while the full symbols represent solid solution phases of $\text{Cu}(\text{Hf,Zr})_2$ and $\text{Cu}_{10}(\text{Hf,Zr})_7$.

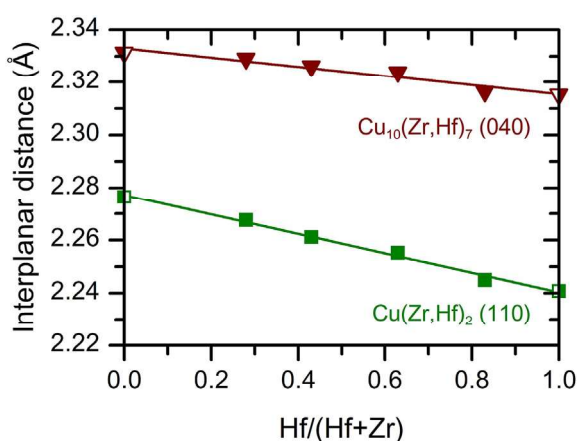


Fig. 6. Evaluated interplanar distances corresponding to the (110) peak of the tetragonal $\text{Cu}(\text{Zr,Hf})_2$ phase and to the (040) peak of the orthorhombic $\text{Cu}_{10}(\text{Zr,Hf})_7$ phase (labeled in Fig. 5).

at.%), the deposition rates from all three targets should be set to approximately the same value. This results from the fact that the molar volumes of Zr (14.01 cm³/mol) and Hf atoms (13.41 cm³/mol) are approximately twice as high as the molar volume of the Cu

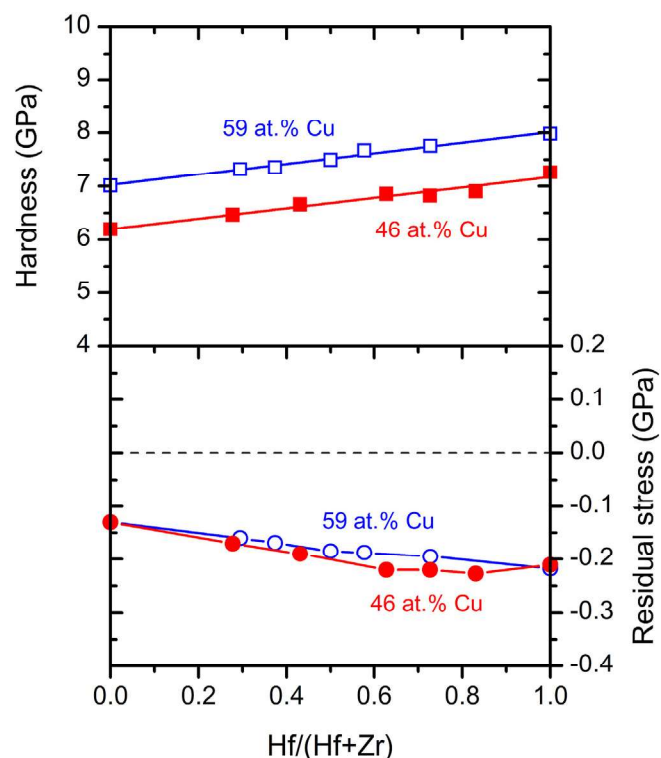


Fig. 7. Hardness and residual stress of Zr-Hf-Cu films of Cu-poor (46 at.% Cu) and Cu-rich (59 at.% Cu) series.

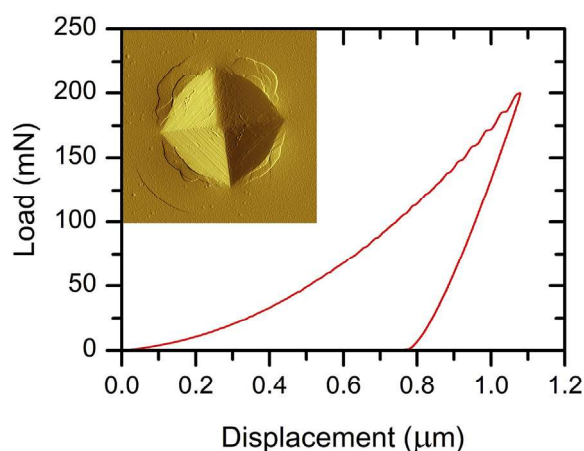


Fig. 8. Indentation curve and AFM image of the indent of the Zr-Hf-Cu film with Hf/(Hf+Zr) = 0.63 obtained a load of 200 mN.

atoms (7.09 cm³/mol). Although this prediction works well when the binary Zr–Cu films are deposited [11], the deposition of the films with a Hf incorporation results in a slightly higher Hf content than expected. This observation can be attributed to the almost twice higher atomic mass of the Hf atoms (178.49) than that of the Zr atoms (91.22) and almost three times higher than that of the Cu atoms (63.55), which may consequently result in more intense flux of fast Ar neutrals backscattered from the Hf target towards the substrate. These fast Ar atoms impact with a quite high energy on the growing film and preferentially resputter Zr and Cu atoms of a lower mass than Hf (supported by our preliminary calculations using the SDTrimSP program [20]).

Fig. 1 clearly shows that the configuration of three independent sputtering targets allowed us to precisely control the elemental

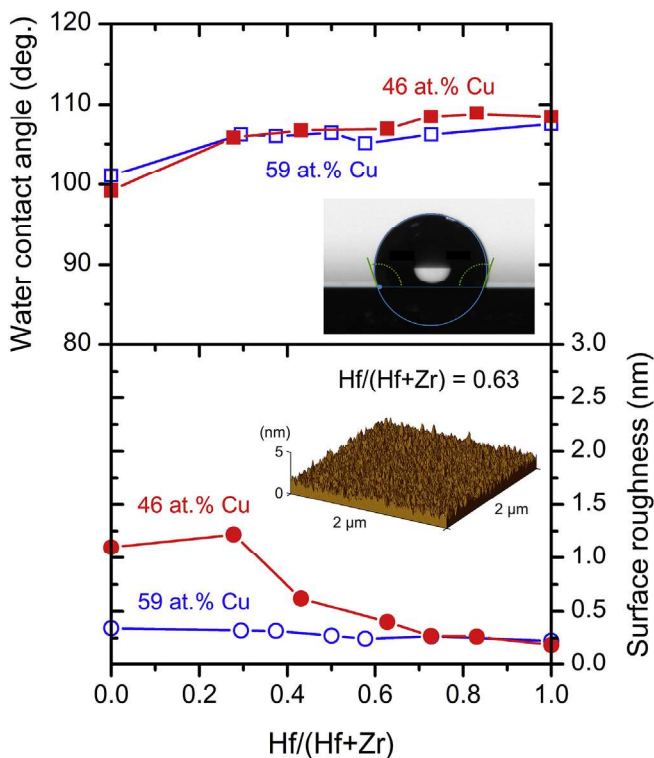


Fig. 9. Water contact angle and surface roughness of Zr-Hf-Cu films of Cu-poor (46 at.% Cu) and Cu-rich (59 at.% Cu) series. The AFM image of the surface morphology and the photograph of a water droplet corresponds to the Zr-Hf-Cu film with Hf/(Hf+Zr) = 0.63.

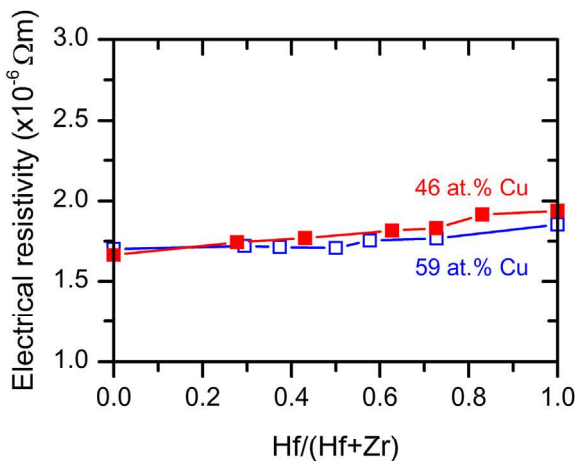


Fig. 10. Electrical resistivity of Zr-Hf-Cu films of Cu-poor (46 at.% Cu) and Cu-rich (59 at.% Cu) series.

composition over a very wide range. As far as we know, there is no comparable experimental study dealing with systematic investigation of the effect of the elemental composition on material properties and behavior in the Zr-Hf-Cu system. The only experimental study has been carried out by Basu et al. on a melt-spun ribbon of the $\text{Cu}_{50}\text{Zr}_{25}\text{Hf}_{25}$ composition [12]. They focused only on the glass forming ability and crystallization process.

3.2. Structure

To investigate the effect of the elemental composition on the

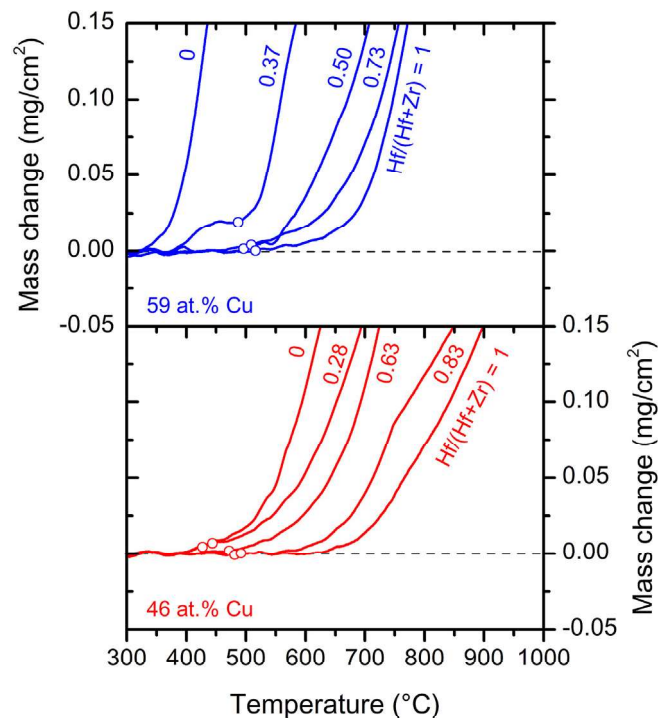


Fig. 11. Oxidation resistance of Zr-Hf-Cu films of Cu-poor (46 at.% Cu) and Cu-rich (59 at.% Cu) series. Open circles represent the crystallization temperatures obtained by DSC at a heating rate of 30 °C/min and recalculated for a heating rate of 10 °C/min.

structure of the Zr-Hf-Cu films, the XRD measurements were performed. Fig. 2 shows the XRD patterns of the Cu-poor film series as a function of a varying Hf/(Hf+Zr) ratio. It can be seen that the XRD patterns for all elemental compositions are characterized by one, broad peak of a low intensity without any other visible diffraction peaks from crystalline phases. The broad peak remains at nearly the same 2θ position of about 38° independently of the Hf/(Hf+Zr) ratio due to the same atomic radius of Hf and Zr (1.55 Å [21]). A very similar set of the XRD patterns was also collected for the Cu-rich film series (not shown). The presence of such a low-intensity broad peak indicates that the as-deposited Zr-Hf-Cu films are X-ray amorphous for all elemental compositions investigated. This experimental observation is consistent with the theoretical predictions [17,18].

Inspecting the XRD patterns of the Cu-poor film series in Fig. 2 in more detail, one can see that the intensity of the broad peak gradually increases as Hf substitutes Zr. The same trend is also observed for the Cu-rich film series. The increase in the intensity is caused by a different X-ray atomic scattering factor of the Zr and Hf atoms. Since X-rays are scattered by the electron cloud of the atoms, the scattering amplitude increases with the atomic number due to a higher number of scattering events. Hence, the binary Hf–Cu films exhibit the highest intensity of the broad peak among other elemental compositions.

3.3. Thermal behavior

The thermal behavior of the Zr-Hf-Cu films annealed in argon up to 600 °C was studied by DSC for both film series. DSC curves from freestanding fragments of the Cu-poor film series are summarized in Fig. 3. It can be seen that all curves exhibit one well-defined exothermic peak, which is related to a crystallization of the films (shown later in Fig. 5) and defining the crystallization temperature, T_c [11]. As can be seen, the peak shifts its position to higher

temperatures with increasing Hf/(Hf+Zr) ratio. The same trend in the evolution of the thermal behavior is also observed for the Cu-rich film series. The only difference between the DSC curves of both film series is that for the Cu-rich series the exothermic peak is positioned at a higher temperature for the same Hf/(Hf+Zr) ratio. The shift of the exothermic peak with increasing Hf/(Hf+Zr) ratio indicates an increasing thermal stability of the Zr-Hf-Cu films as compared to the binary Zr–Cu films.

A detailed examination of each DSC curve in the vicinity of the exothermic peak revealed a decrease of the heat flow before the onset of the peak. This feature, known as the glass transition, is a typical behavior of glasses and defines the glass transition temperature, T_g [11]. The temperature range between T_g and T_c corresponds to the super-cooled liquid region, $\Delta T = T_c - T_g$, in which metallic glasses exhibit viscous flow and behave thermoplastically [22].

Fig. 4 shows the evolution of T_c and T_g with increasing Hf/(Hf+Zr) ratio for both film series. It can be seen that the values of T_c as well as T_g increase monotonically with increasing Hf/(Hf+Zr) ratio in both series. The values may be very well fitted using linear regressions (the square of the correlation coefficient better than 97% in all four cases). Since the slopes of the linear fits of T_c and T_g in each series are very similar, the width of ΔT across the whole range of the elemental composition remains constant. Its value is of approximately 43 °C for the Cu-poor series and 40 °C for the Cu-rich series. These values are comparable with those measured for the $\text{Cu}_{50}\text{Zr}_{25}\text{Hf}_{25}$ melt-spun ribbons [12] and also for the binary Zr–Cu thin-film metallic glasses from our previous study [11]. The substitution of Hf for Zr, however, shifts the supercooled liquid region to higher temperatures. In parallel, the higher Cu content has the same effect. Thereby, the thermal stability of the glassy state and thus the position of the supercooled liquid region can be finely tuned in a very wide temperature range (ΔT from 405 °C to 533 °C) by the controlling the elemental composition, i.e. the Hf/(Hf+Zr) ratio and the Cu content.

To identify products of the crystallization of the Zr-Hf-Cu films after the DSC analysis, XRD patterns were taken from the film fragments turned into the powders. As expected from DSC, the films from both series are well crystallized after their annealing to 600 °C in argon. Fig. 5 shows the XRD patterns corresponding to the Cu-poor film series. We found that all annealed films consist of two types of intermetallic phases, which crystallize in a very narrow temperature interval as follows from the presence of only one apparent exothermic peak on the DSC curves, see Fig. 3. No crystalline oxide phases were detected by XRD for all films. In case of the binary Zr–Cu films [Hf/(Hf+Zr) = 0], the XRD peaks can be assigned to the tetragonal CuZr_2 phase (PDF Card No. 00-018-0466) and the orthorhombic $\text{Cu}_{10}\text{Zr}_7$ phase (PDF Card No. 01-078-3211) while in case of the binary Hf–Cu films [Hf/(Hf+Zr) = 1] to the tetragonal CuHf_2 phase (PDF Card No. 04-004-2396) and the

orthorhombic $\text{Cu}_{10}\text{Hf}_7$ phase (PDF Card No. 01-082-6313). The ternary Zr–Hf–Cu films exhibit XRD peaks in between the positions of both types of these phases. Fig. 6 shows the evolution of the interplanar distances corresponding the (110) peak of the tetragonal phase and the (040) peak of the orthorhombic phase (labeled in Fig. 5). An almost linear decrease of the interplanar distances with increasing Hf/(Hf+Zr) ratio can be explained by the Vegard's law [23]. That is, the crystallized Zr-Hf-Cu films consist of solid solution phases of $\text{Cu}(\text{Hf,Zr})_2$ and $\text{Cu}_{10}(\text{Hf,Zr})_7$, in which Hf gradually substitutes Zr with increasing Hf/(Hf+Zr) ratio.

In case of the Cu-rich film series, the crystallization also results in the formation of the tetragonal $\text{Cu}(\text{Hf,Zr})_2$ and orthorhombic $\text{Cu}_{10}(\text{Hf,Zr})_7$ solid solutions but in this case $\text{Cu}_{10}(\text{Hf,Zr})_7$ is the predominant phase.

3.4. Mechanical properties

The effect of the elemental composition on the hardness of the Zr-Hf-Cu thin-film metallic glasses is shown in the upper panel of Fig. 7. It is seen that the hardness monotonically increases with increasing Hf/(Hf+Zr) ratio from 6.2 GPa to 7.3 GPa for the Cu-poor film series and from 7.0 GPa to 8.0 GPa for the Cu-rich film series. Both dependences can be well fitted by straight lines. The lower panel of Fig. 7 shows the residual stress as a function of the Hf/(Hf+Zr) ratio. All as-deposited films are in a compressive residual stress which is beneficial in terms of enhancing the hardness and suppressing the crack propagation in the material. As shown in our previous study [11], the compressive stress, which is generated in the films instead of the tensile one, is attributed to the bombardment of the growing film by a highly ionized flux of Cu ions with enhanced energies generated in a high power plasma discharge. The absolute values of the stress do, however, not much differ for the two Cu contents investigated (46 at.% and 59 at.%). They slightly increase from 0.13 to 0.23 GPa with increasing Hf/(Hf+Zr) ratio due to increasing flux of heavy Hf atoms impacting on the growing film. The evolution of the effective Young's modulus (see Table 1) follows the trend of the hardness. The values vary from 109 GPa to 127 GPa for the Cu-poor film series and from 121 GPa to 131 GPa for the Cu-rich film series. In case of the evolution of the elastic recovery (see Table 1), we observed no strong dependence on the Hf/(Hf+Zr) ratio. The values scatter within a narrow band around 36.8% and 38.0% for the Cu-poor and Cu-rich film series, respectively. It is evident that the Zr-Hf-Cu films deform predominantly plastically during the indentation tests. Inspecting the indents by using atomic force microscopy, we observed the formation of shear bands on pile-ups. The shear bands were also detected on the loading curves as sharp steps (pop-ins). All these deformation phenomena were more pronounced at higher indentation loads as seen in Fig. 8 for 200 mN. We were, however, not able to recognize a significant difference in the deformation behavior under the indentation with

Table 1

Hardness H , effective Young's modulus $E^* = E/(1 - \nu^2)$ and elastic recovery W_e of the Zr-Hf-Cu films from Cu-poor (46 at.% Cu) and Cu-rich (59 at.% Cu) series (E is Young's modulus and ν is Poisson's ratio).

Cu-poor series							
Hf/(Hf+Zr)	0	0.28	0.43	0.63	0.73	0.83	1
H (GPa)	6.2	6.5	6.7	6.9	6.8	6.9	7.3
E^* (GPa)	109	115	118	121	120	123	127
W_e (%)	36.1	36.7	36.7	37.2	36.9	36.5	37.3
Cu-rich series							
Hf/(Hf+Zr)	0	0.29	0.37	0.50	0.58	0.73	1
H (GPa)	7.0	7.3	7.4	7.5	7.7	7.8	8.0
E^* (GPa)	121	124	126	126	127	128	131
W_e (%)	37.7	37.7	37.9	38.2	38.1	38.3	38.4

increasing Hf/(Hf+Zr) ratio. At present, more detailed micro-mechanical analysis of the deformation behavior under bending is in progress and will be published in a separate paper.

Comparing the data displayed in Figs. 4 and 7 and Table 1, we can see a clear correlation of the evolution of the crystallization temperature, the glass transition temperature and the mechanical properties. A very similar behavior has been also reported on multielement (Hf,Zr)–Ti–Cu–Ni–Al metallic glasses produced as ribbons by melt spinning [24]. In that case, an increasing Hf content resulted in an increase of all characteristic temperatures (glass transition, crystallization and melting) and mechanical properties such as Young's modulus, the yield and fracture stress. Since Hf substitutes Zr in the structure of these metallic glasses without a significant change of atomic ordering, it can be supposed that the increase of all aforementioned quantities is primarily associated with an increase of the average bond energy. This is supported by the fact that Hf exhibits a larger overlap of the *d*-orbitals than Zr, which results in more covalent character of the metallic-covalent bonds and consequently in a higher bond energy. Moreover, diffusion-controlled processes can be limited by a lower mobility of Hf (approximately twice higher atomic mass of Hf than Zr). In case of our Zr–Hf–Cu thin-film metallic glasses, the increase of mechanical properties can be also enhanced by an increase of the compressive residual stress. On the other hand, the increase of the characteristic temperatures and mechanical properties with increasing Cu content from 46 at.% to 59 at.% can be understood as a consequence of the formation of a higher number of icosahedral clusters and thus a higher average coordination number and a higher atomic packing density [11].

3.5. Surface properties

Surface properties of the Zr–Hf–Cu thin-film metallic glasses including the wettability and the surface roughness are presented in Fig. 9 as a function of the Hf/(Hf+Zr) ratio. The wettability was evaluated by means of the water contact angle. One can see from the upper panel of Fig. 9 that the films from both series exhibit a hydrophobic surface. The values of the water contact angle range from 99° to 109°. One may notice that the water contact angle is higher by about 5° compared to the binary Zr–Cu films when incorporating the lowest fraction of Hf into the films [Hf/(Hf+Zr) ≈ 0.3]. On the other hand, there is no significant effect of the Cu content on the wettability for the compositions investigated.

The bottom panel of Fig. 9 shows the arithmetic average surface roughness of both film series. All films exhibit very low surface roughness. As you can notice, the surface roughness decrease with increasing Hf/(Hf+Zr) ratio down to an extremely low value of 0.2 nm, which indicates very smooth surface of the Zr–Hf–Cu thin-film metallic glasses. The decrease is more pronounced for the Cu-poor film series, which exhibits a slightly higher surface roughness due to a lower flux of sputtered Cu ions with enhanced energies bombarding the growing film. Increasing the deposition rate from the Hf target contributes to more intense flux of sputtered Hf atoms with a high atomic mass, which impact on the growing film, incorporate into it, densify it and consequently reduce the surface roughness. The role of fast Ar neutrals backscattering from the Hf target and impacting on the growing film can be also crucial in terms of reducing the surface roughness.

3.6. Electrical resistivity

Fig. 10 shows the electrical resistivity of both series of the Zr–Hf–Cu thin-film metallic glasses measured at room temperature. All films exhibit a very low electrical resistivity with the values ranging between 1.6 and $1.9 \times 10^{-6} \Omega\text{m}$. The electrical resistivity slightly

increases with increasing Hf/(Hf+Zr) ratio but is slightly lower for the Cu-rich series. The increase in the electrical resistivity with increasing Hf incorporation can be attributed to more covalent character of bonds of Hf than Zr resulting in less free electrons. Similarly, the higher Cu concentration may provide more free electrons responsible for a higher electrical conductivity of the films.

3.7. Oxidation resistance

Thermogravimetric oxidation curves of the Zr–Hf–Cu films from both series measured from room temperature up to 1000 °C in flowing air are presented in Fig. 11. It is seen that the oxidation resistance is strongly dependent on the Cu content and the Hf/(Hf+Zr) ratio. The binary Zr–Cu film with 46 at.% Cu starts to oxidize at about 400 °C while the film with 59 at.% Cu at about 100 °C lower temperature. That is, the higher Cu content has a negative effect on the oxidation resistance. This is because oxidized Cu forms less efficient diffusion barrier against oxidation than oxidized Zr. We have shown recently that a pure Cu film oxidizes rapidly at about 300°C while a pure Zr film at about 400°C [25]. Let us also note that the Zr–Cu film with 42 at.% Cu exhibits a superior oxidation resistance compared to pure Zr or Cu films (not shown here and still under investigation).

A gradual substitution of Hf for Zr causes a shift of the onset of the oxidation to higher temperatures in both film series. Open circles, plotted on the curves in Fig. 11, represent the crystallization temperatures for each composition obtained by DSC at a heating rate of 30 °C/min and recalculated for the heating rate of 10 °C/min using Lasocka's equation [26], see Fig. 4. It is clearly seen that all films from the Cu-poor series and the films from the Cu rich series prepared with Hf/(Hf+Zr) ≥ 0.5 exhibit a low mass gain before starting to crystallize. This suggests that the incorporation of Hf into the films has a positive effect on the oxidation behavior and enables to maintain the high oxidation resistance of the Zr–Hf–Cu thin-film metallic glasses even in the super-cooled liquid region. More detailed investigation of the oxidation behavior of these materials is still in progress and will be published in a separate paper.

4. Conclusions

Conventional dc and high-power impulse magnetron co-sputtering of Zr, Hf and Cu in pure argon was proved to be a suitable deposition technique for a reproducible preparation of Zr–Hf–Cu thin-film metallic glasses with a tunable composition and properties.

Ternary Zr–Hf–Cu alloy films with an amorphous structure and glass-like behavior were prepared with a gradually increasing Hf/(Hf+Zr) ratio at 46 at.% Cu and 59 at.% Cu. A clear correlation among the evolution of the glass transition temperature, crystallization temperature, hardness and effective Young's modulus with increasing Hf/(Hf+Zr) ratio was observed. A linear increase of all these quantities can be attributed to an increase of average bond energy as Hf with more covalent character of bonds gradually substitutes Zr in the amorphous structure. Electrically conductive Zr–Hf–Cu thin-film metallic glasses exhibit enhanced hardness (up to 7.8 GPa), enhanced thermal stability and oxidation resistance, and very smooth (surface roughness down to 0.2 nm) and hydrophobic surface (water contact angle up to 109°). Tuning their elemental composition allows us to control the supercooled liquid region in a very wide range from 405 °C to 533 °C, which may be crucial for miscellaneous applications.

Acknowledgments

The authors thank Dr. Jiří Houška, Dr. Jiří Čapek, Dr. Šimon Kos

and Dr. Tomáš Kozák for helpful discussions and calculations, and Dr. Stanislav Haviar for the measurement of the elemental composition. This work was supported by the Czech Science Foundation under Project No. GA16-18183S.

References

- [1] M. Telford, The case for bulk metallic glass, *Mater. Today Off.* 7 (2004) 36–43, [https://doi.org/10.1016/S1369-7021\(04\)00124-5](https://doi.org/10.1016/S1369-7021(04)00124-5).
- [2] M.F. Ashby, A.L. Greer, Metallic glasses as structural materials, *Scr. Mercat.* 54 (2006) 321–326, <https://doi.org/10.1016/j.scriptamat.2005.09.051>.
- [3] A.L. Greer, Metallic glasses on the threshold, *Mater. Today* 12 (2009) 14–22, [https://doi.org/10.1016/S1369-7021\(09\)70037-9](https://doi.org/10.1016/S1369-7021(09)70037-9).
- [4] J. Schroers, G. Kumar, T.M. Hodges, S. Chan, T.R. Kyriakides, Bulk metallic glasses for biomedical applications, *JOM* 61 (2009) 21–29, <https://doi.org/10.1007/s11837-009-0128-1>.
- [5] H.W. Sheng, W.K. Luo, F.M. Alamgir, J.M. Bai, E. Ma, Atomic packing and short-to-medium-range order in metallic glasses, *Nature* 439 (2006) 419–425, <https://doi.org/10.1038/nature04421>.
- [6] A.R. Yavari, Materials science: a new order for metallic glasses, *Nature* 439 (2006) 405–406, <https://doi.org/10.1038/439405a>.
- [7] N. Mattern, P. Jávári, I. Kaban, S. Gruner, A. Elsner, V. Kokotin, H. Franz, B. Beuneu, J. Eckert, Short-range order of Cu–Zr metallic glasses, *J. Alloys Compd.* 485 (2009) 163–169, <https://doi.org/10.1016/j.jallcom.2009.05.111>.
- [8] D.Z. Chen, C.Y. Shi, Q. An, Q. Zeng, W.L. Mao, W.A. Goddard, J.R. Greer, Fractal atomic-level percolation in metallic glasses, *Science* 349 (2015) 1306–1310, <https://doi.org/10.1126/science.aab1233>.
- [9] P. Coddet, F. Sanchette, J.C. Rousset, O. Rapaud, C. Coddet, On the elastic modulus and hardness of co-sputtered Zr–Cu–(N) thin metal glass films, *Surf. Coating. Technol.* 206 (2012) 3567–3571, <https://doi.org/10.1016/j.surfcoat.2012.02.036>.
- [10] M. Apreutesei, P. Steyer, L. Joly-Pottuz, A. Billard, J. Qiao, S. Cardinal, F. Sanchette, J.M. Pelletier, C. Esnouf, Microstructural, thermal and mechanical behavior of co-sputtered binary Zr–Cu thin film metallic glasses, *Thin Solid Films* 561 (2014) 53–59, <https://doi.org/10.1016/j.tsf.2013.05.177>.
- [11] P. Zeman, M. Zitek, S. Zuzjaková, R. Čerstvý, Amorphous Zr–Cu thin-film alloys with metallic glass behavior, *J. Alloy. Comp.* 696 (2017) 1298–1306, <https://doi.org/10.1016/j.jallcom.2016.12.098>.
- [12] J. Basu, S. Ranganathan, Glass forming ability and stability: ternary Cu bearing Ti, Zr, Hf alloys, *Intermetallics* 17 (2009) 128–135, <https://doi.org/10.1016/j.intermet.2008.10.006>.
- [13] S. Nayebossadri, D. Smith, J. Speight, D. Book, Amorphous Zr-based thin films fabricated by magnetron sputtering for potential application in hydrogen purification, *J. Alloy. Comp.* 645 (2015) S56–S60, <https://doi.org/10.1016/j.jallcom.2015.01.230>.
- [14] J.H. Shin, D. Kim, H. Cho, D. Hyung, H. Suematsu, K. Ho, The effect of Mo addition on the microstructural evolution and mechanical properties of Zr–Cu-based metallic glass thin films, *J. Ceram. Process. Res.* 15 (2014) 130–135.
- [15] T.L. Cheung, C.H. Shek, Thermal and mechanical properties of Cu–Zr–Al bulk metallic glasses, *J. Alloy. Comp.* 434 (2007) 71–74, <https://doi.org/10.1016/j.jallcom.2006.08.109>.
- [16] H.S. Chou, J.C. Huang, L.W. Chang, T.G. Nieh, Structural relaxation and nano-indentation response in Zr–Cu–Ti amorphous thin films, *Appl. Phys. Lett.* 93 (2008) 191901, <https://doi.org/10.1063/1.2999592>.
- [17] J. Basu, B.S. Murty, S. Ranganathan, Glass forming ability: miedema approach to (Zr, Ti, Hf)–(Cu, Ni) binary and ternary alloys, *J. Alloy. Comp.* 465 (2008) 163–172, <https://doi.org/10.1016/j.jallcom.2007.10.131>.
- [18] S.Y. Luo, Y.Y. Cui, Y. Dai, J.H. Li, B.X. Liu, Interatomic potential to predict the favored and optimized compositions for ternary Cu–Zr–Hf metallic glasses, *J. Appl. Phys.* 112 (2012) 103518, <https://doi.org/10.1063/1.4766389>.
- [19] W.C. Oliver, G.M. Pharr, An improved technique for determining hardness and elastic modulus using load and displacement sensing indentation experiments, *J. Mater. Res.* 7 (1992) 1564–1583, <https://doi.org/10.1557/JMR.1992.1564>.
- [20] W. Eckstein, R. Dohmen, A. Mutzke, R. Schneider, SDTrimSP: ein Monte-Carlo Code zur Berechnung von Stossereignissen in ungeordneten Targets = SDTrimSP: a Monte-Carlo Code for Calculating Collision Phenomena in Randomized Targets (IPP 12/3), Max-Planck-Institut für Plasmaphysik, Garching, 2007. <http://hdl.handle.net/11858/00-001M-0000-0027-04E8-F>.
- [21] J.C. Slater, Atomic radii in crystals, *J. Chem. Phys.* 41 (1964) 3199–3204, <https://doi.org/10.1063/1.1725697>.
- [22] G. Kumar, J. Schroers, Write and erase mechanisms for bulk metallic glass, *Appl. Phys. Lett.* 92 (2008) 31901, <https://doi.org/10.1063/1.2834712>.
- [23] L. Vegard, Die Konstitution der Mischkristalle und die Raumfüllung der Atome, *Zeitschrift Für Phys. A Hadron. Nucleus* 5 (1921) 17–26.
- [24] X. Gu, T. Jiao, L.J. Kecskes, R.H. Woodman, C. Fan, K.T. Ramesh, T.C. Hufnagel, Crystallization and mechanical behavior of (Hf, Zr)–Ti–Cu–Ni–Al metallic glasses, *J. Non-Cryst. Solids* 317 (2003) 112–117, [https://doi.org/10.1016/S0022-3093\(02\)01990-7](https://doi.org/10.1016/S0022-3093(02)01990-7).
- [25] J. Musil, P. Zeman, M. Jirout, M. Šašek, R. Čerstvý, Oxidation of sputtered Cu, Zr, ZrCu, ZrO₂, and Zr–Cu–O films during thermal annealing in flowing air, *Plasma Process. Polym.* 4 (2007) S536–S540, <https://doi.org/10.1002/ppap.200731401>.
- [26] M. Lasocka, The effect of scanning rate on glass transition temperature of splat-cooled Te₈₅Ge₁₅, *Mater. Sci. Eng.* 23 (1976) 173–177, [https://doi.org/10.1016/0025-5416\(76\)90189-0](https://doi.org/10.1016/0025-5416(76)90189-0).

Part C

Impact of Al or Si addition on properties and oxidation resistance of magnetron sputtered Zr–Hf–Al/Si–Cu metallic glasses

M. Zítek, P. Zeman, M. Kotrlová, R. Čerstvý

Journal of Alloys and Compounds 772 (2019) 409–417



Impact of Al or Si addition on properties and oxidation resistance of magnetron sputtered Zr–Hf–Al/Si–Cu metallic glasses



M. Zítek, P. Zeman^{*}, M. Kotrlová, R. Čerstvý

Department of Physics and NTIS - European Centre of Excellence, University of West Bohemia, Univerzitní 8, 306 14, Plzeň, Czech Republic

ARTICLE INFO

Article history:

Received 15 July 2018

Received in revised form

4 September 2018

Accepted 7 September 2018

Available online 8 September 2018

Keywords:

Zr–Hf–Al/Si–Cu

Amorphous material

Metallic glass

Thin film

Magnetron sputtering

ABSTRACT

Amorphous quaternary Zr–Hf–Al/Si–Cu thin-film metallic alloys were prepared by non-reactive magnetron co-sputtering using four unbalanced magnetrons equipped with Zr, Hf, Al or Si, and Cu targets. The Zr, Hf and Al or Si targets were sputtered in dc regimes while the Cu target in a high-power impulse regime. Two series of films with either Al (up to 17 at.%) or Si (up to 12 at.%) addition were deposited. The effect of the elemental composition on the structure, thermal behavior, mechanical and surface properties, electrical resistivity and oxidation resistance was systematically investigated. All Zr–Hf–Al/Si–Cu films were deposited with an X-ray amorphous structure. The glass transition was, however, recognized only up to 12 at.% Al or 6 at.% Si. The addition of Al or Si enhances mechanical properties of the films and the thermal stability of their amorphous state. This may be explained by an increase of a covalent component of the mixed metallic-covalent bonds with increasing the Al and Si content. Moreover, the Zr–Hf–Al–Cu metallic glasses exhibit a wider super-cooled liquid region, while the Zr–Hf–Si–Cu metallic glasses are more oxidation resistant.

© 2018 Elsevier B.V. All rights reserved.

1. Introduction

Metallic glasses as a promising new type of materials have been widely studied during past years. It is well known that they exhibit many exceptional properties including for instance high yield strength, high elastic strain and hardness, temperature-independent electrical resistivity, excellent surface finishing, and biocompatibility [1–5]. Their unique properties originate from the disordered atomic structure without grain boundaries that contrasts with the well-defined atomic lattice arrangement in crystalline alloys [6–8].

Zr- and Cu-based metallic glasses have been extensively studied both as bulk metallic glasses (BMGs) [9–16] and as thin film metallic glasses (TFMGs) [17–24]. In recent years, several investigations have confirmed that selecting a proper alloying element in an appropriate amount has beneficial effects on the properties of the Zr- and Cu-based metallic glasses. For instance, Choi-Yim et al. [10] reported that the addition of Si up to 2 at.% into Cu₄₇Ti₃₄Zr₁₁Ni₈ improves the thermal stability and expands the supercooled liquid region. A similar effect was observed also for

Zr₄₇Cu₄₄Al₉ metallic glasses alloyed with Si [15]. However, it has also been reported that addition of more than approximately 2 at.% Si into the melt often leads to a rapid crystallization during the fabrication process of BMGs [11]. On the other hand, Zr–Ti–B–Si and Zr–Ti–Si–W thin-film alloys were prepared by magnetron sputtering with an amorphous structure up to 20 at.% Si [21,22]. Unfortunately, it has not been reported if these amorphous alloys exhibit the glass transition. Contrary to Si-containing BMGs, alloying with Al preserves amorphous structure to at least 10 at.% of Al [9,12–14]. An optimized addition of Al into BMGs improves thermal stability [12,14], enhances hardness [14], extends the supercooled liquid region [9,12,14] and increases the critical diameter of BMGs [16]. One may see that alloying with either Al or Si may lead in certain material systems to enhanced properties. We have recently shown that the ternary Zr–Hf–Cu thin-film metallic glasses exhibit enhanced hardness, thermal stability and oxidation resistance, and very smooth and hydrophobic surface [24]. However, the effect of an addition of either Al or Si into the Zr–Hf–Cu system has not been studied yet.

The present study is, therefore, focused on the Zr–Hf–Al/Si–Cu thin-film alloys prepared by magnetron co-sputtering, which was proved to be a suitable technique for deposition of the Zr–Cu based metallic glasses [17–20,23,24]. We utilize four independent magnetrons (each of them equipped with a different material) to

^{*} Corresponding author.

E-mail address: zemanp@kfy.zcu.cz (P. Zeman).

precisely control the elemental composition of the Zr–Hf–Al/Si–Cu thin-film alloys. The main aim of this study lies in a systematic investigation of the effect of an addition of Al or Si into the Zr–Hf–Cu thin-film alloys on their properties and behavior. In particular, we focus on the correlation between elemental composition and structure, thermal behavior, mechanical and surface properties, electrical resistivity and oxidation resistance of the Zr–Hf–Al/Si–Cu thin-film alloys. Since Zr–Hf–Al/Si–Cu thin-film alloys have not been synthesized yet, we systematically investigate different properties and behavior in detail.

2. Experimental details

Quaternary Zr–Hf–Al/Si–Cu thin-film alloys were deposited by magnetron co-sputtering using an AJA International ATC 2200-V sputter system which was pumped by a turbomolecular pump (1200 l/s) backed up with a multi-stage roots pump (27 m³/hr). The base pressure before each deposition was lower than 5×10^{-5} Pa. Depositions were carried out in argon at a pressure of 0.533 Pa (4 mTorr) using four independent unbalanced magnetrons equipped with circular, indirectly cooled targets (50.8 mm in diameter, 6.35 mm in thickness). The magnetrons with the Zr target (99.5% purity, Matsurf Technologies Inc.) and the Hf target (99.9% purity, Plasmaterials Inc.) were powered by a dual power supply (Pinnacle Plus+ 5/5 kW, Advanced Energy) working independently in two dc regimes. The magnetron with the Al target (99.99% purity, Matsurf Technologies Inc.) or the Si target (99.99% purity, Matsurf Technologies Inc.) was powered by a dc power supply (DCXS-750-4, AJA International Inc.) and the magnetron with the Cu target (99.99% purity, Matsurf Technologies Inc.) was powered by a pulsed dc power supply (TruPlasma Highpulse 4002, Hüttinger Elektronik) working in a high-power impulse regime. The average target power density in a pulse was fixed at 1000 W/cm². The negative voltage pulse length was set to a constant value of 200 μ s and the repetition frequency was set to either 36 Hz or 46 Hz. All films were deposited onto polished and ultrasonically pre-cleaned single-crystalline Si(100), soda-lime glass and molybdenum substrates held at a floating potential without any external heating. The substrates were rotated above the targets at a speed of 40 rpm and located at a target-to-substrate distance of 150 mm.

The elemental composition of the Zr–Hf–Al/Si–Cu films was controlled by adjusting the deposition rates from the Zr, Hf, (Al,Si) and Cu targets independently, particularly by the dc target powers (Zr, Hf, and (Al,Si)) and the average target power in a period (Cu). The deposition rates were measured before each deposition using a quartz crystal deposition rate monitor (SQM-160, Inficon).

The elemental composition of the as-deposited films on the Si substrate was analyzed by a scanning electron microscope (SU-70, Hitachi) operated at a primary electron energy of 20 keV using an energy dispersive spectroscopy (UltraDry, Thermo Scientific) to quantify the Zr, Hf, Al and Cu content and wavelength dispersive spectroscopy (MagnaRay WDS, Thermo Scientific) to quantify the Si content. Bulk standards of all elements were used for the quantitative analysis. The error of the elemental analysis was established to be 1 at.%.

The thermal behavior of the films was investigated by differential scanning calorimetry (DSC). Approximately 2- μ m thick films deposited onto the molybdenum thin foils (0.1 mm in thickness) were relatively easily delaminated from this kind of the substrate by its bending. Obtained freestanding film fragments ($\sim 3 \times 3$ mm² each) of a total mass of 5 mg were then inserted into a 100 μ l alumina crucible covered with a lid. An identical uncharged crucible was used as a reference. The measurements were carried out at the same heating and cooling rate of 30 °C/min in flowing argon (1 l/h) in the temperature range from room temperature to 600 °C

using a DSC system (Labsys DSC 1600, Setaram). The calorimeter was calibrated by melting of Pb, Zn and Al standards with purity of $99.998 \pm 0.001\%$.

X-ray diffraction (XRD) measurements of the structure of the as-deposited films on the Si substrates and of the powdered film fragments after their annealing were carried out using a diffractometer (X'Pert PRO, PANalytical) with Cu K α radiation ($\lambda_{\text{Cu}} = 0.154187$ nm) working in a slightly asymmetrical Bragg-Brentano geometry with an ω -offset of 1.5° and in the standard Bragg-Brentano geometry, respectively. The ω -offset was used to eliminate a strong reflection of the single-crystalline Si(100) substrate at 2θ angle of 69.17°. The data were collected using an ultrafast detector X'Celerator in the 2θ range of 20°–60°.

The film thickness and the curvature of the Si substrate coated with the film, from which a residual macrostress was determined using the modified Stoney's formula, were measured by a surface profilometer (Dektak 8 Stylus Profiler, Veeco). The hardness, effective Young's modulus and elastic recovery of the films on the Si substrate were evaluated from the load vs. displacement curves [25], which were measured at room temperature and in ambient environment by a nanoindenter (TI 950 Triboindenter, Hysitron) equipped with a Berkovich-type diamond tip. For each film, a number of indents were made at different loads ranging from 1 to 10 mN and the obtained data were averaged. The ratio of the penetration depth and the film thickness was below 10% in all cases.

The electrical resistivity of the films on the glass substrate was measured at room temperature by a standard four-point probe with a spacing of 1.047 mm between the tips (Cylindrical probe, Jandel). The nonconductive glass substrate was used to avoid the effect of an electrically conductive substrate on the data measured. The measurement was also not affected by a very thin surface oxide layer (few nm in thickness) formed on the films as a result of a reaction with an ambient atmosphere because the penetration depth of the probe tips was much higher (approximately 150 nm). The water contact angle of the films on the Si substrate was measured at room temperature by a drop shape analyzer (DSA30, KRÜSS) using the sessile drop method with a droplet of distilled water with volume of 2 μ l. Three measurements on each film at various positions were carried out and the obtained values were averaged. A typical error of the measurement was $\pm 1^\circ$. The arithmetic average surface roughness of the films on the Si substrate was evaluated from a selected square area of 2×2 μ m² measured in a non-contact mode of an atomic force microscope (SmartSPM, AIST-NT) equipped with a silicon tip (nominal radius of 10 nm).

The oxidation resistance of the films was investigated by thermogravimetry (TG) using a symmetrical high resolution system (Setaram TAG 2400). The TG analysis was carried out in synthetic atmospheric air (flow rate of 1 l/h) with dynamic heating in the temperature range from room temperature up to 1000 °C and isothermal heating at 550 °C for 3 h. The heating rates were set to 10 °C/min and 50 °C/min for dynamic heating and isothermal heating, respectively. The cooling rates were set in both cases to 30 °C/min. The Si substrates were coated only on one side. After subtracting the thermogravimetric signal corresponding to oxidation of the uncoated sides, the resulting thermogravimetric curve is related to the oxidation resistance of the Zr–Hf–Al/Si–Cu film only.

The thickness of the surface oxide layer was determined by a J.A. Woollam Co. variable angle spectroscopic ellipsometer. The measurements were performed in the wavelength range from 300 to 2000 nm using angles of incidence of 65°, 70° and 75° in reflection.

3. Results and discussion

In this section, the effect of an addition of Al (up to 17 at.%) or Si

(up to 12 at.%) into the Zr–Hf–Cu thin-film alloys on their properties and behavior is investigated. Two film series, labeled as Al-series and Si-series from now on, are systematically studied. The effect of the elemental composition (Fig. 1) on the structure (Figs. 2 and 3), thermal behavior (Figs. 4–7), mechanical (Figs. 8 and 9) and surface properties (Fig. 10), electrical resistivity (Fig. 11) and oxidation behavior (Figs. 12 and 13) is presented and discussed in detail.

3.1. Elemental composition

The elemental composition of the Zr–Hf–Al/Si–Cu thin-film alloys was varied by adjusting the deposition rate from the Zr, Hf, Al or Si and Cu targets as described in Experimental details. The total deposition rate varied from 27 nm/min to 36 nm/min and the thickness of all films was around 2 μm . In both series, we started the experiments with the deposition of the ternary Zr–Hf–Cu thin film with approximately 46 at.% Cu, 27 at.% Zr and 27 at.% Hf. A subsequent addition of Al or Si was done at the expense of Zr and Hf while maintaining the ratio $[\text{Zr}]:[\text{Hf}] \approx 1$ and the content of Cu at approximately 46 at.%. An evolution of the elemental composition of the films of the Si-series as a function of the applied power at the Si target is shown in Fig. 1. A similar evolution was observed also for the Al-series except that the comparable Al content was achieved for a lower applied power at the Al target. This is due to different sputtering yields of Al and Si for a comparable energy of impacting Ar ions [26]. One may notice that by setting appropriate target powers, we were able to precisely control the elemental composition in the whole studied range. The Al and Si content in the films was varied from 0 to 17 at.% and from 0 to 12 at.%, respectively.

3.2. Structure

In order to investigate the effect of the elemental composition on the structure of the as-deposited films, the XRD measurements were carried out. XRD patterns of the films of the Al-series are presented in Fig. 2. As can be seen, all films containing up to 17 at.% Al exhibit a low-intensity broad diffraction peak (hump) indicating that these films are X-ray amorphous. The full width at half maximum of this peak is around $5^\circ 2\theta$. As for the Si-series, a similar set of XRD patterns were collected (not shown). It implies that these films are also X-ray amorphous in the whole range investigated, i.e. from 0 to 12 at.% Si. Such a high content of Si for the amorphous alloys based on Zr–Cu has not been reported for BMGs so far, as described in Introduction. Our results point out the key

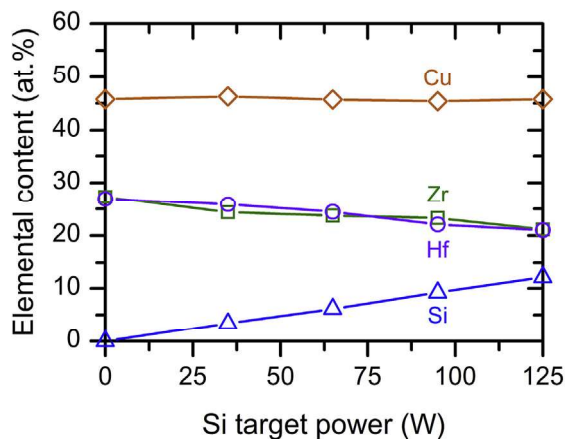


Fig. 1. Elemental composition of the films of the Si-series as a function of the applied power at the Si target.

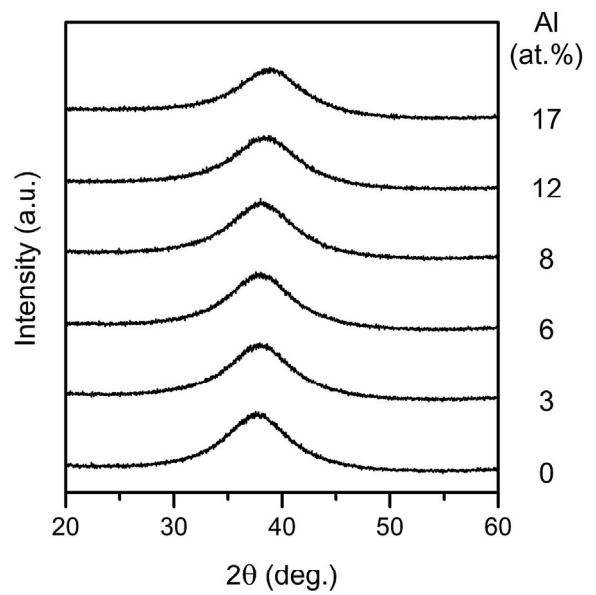


Fig. 2. XRD patterns of the as-deposited films of the Al-series.

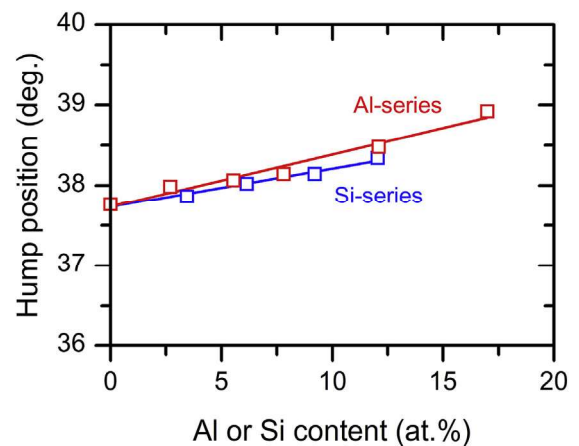


Fig. 3. Position of the broad diffraction peak (hump) of the films of the Al- and Si-series as a function of the Al or Si content.

importance of using magnetron sputtering with very high cooling rates of the vapor on the substrate for the deposition of amorphous thin-film metallic alloys in a wide composition range.

A closer look at the XRD patterns reveals that the maximum of the broad peak shifts to higher 2θ angles with increasing Al and Si content for both film series, see Fig. 3. As mentioned before, either element (Al and Si) is added at the expense of Zr and Hf and both have a lower atomic radius than Zr and Hf. Thus, the average interatomic distance in the material decreases with their addition, which consequently leads to the shift of the hump to higher 2θ angles. As shown in Fig. 3, the shift may be very well fitted by a linear regression. Despite the fact that the radius of Al is larger than that of Si the slope of the straight line fitting the values of the Al-series is steeper indicating more rapid decrease of the interatomic distance with increasing Al content.

3.3. Thermal behavior

The effect of the elemental composition on the thermal behavior of the Zr–Hf–Al/Si–Cu films was studied using differential

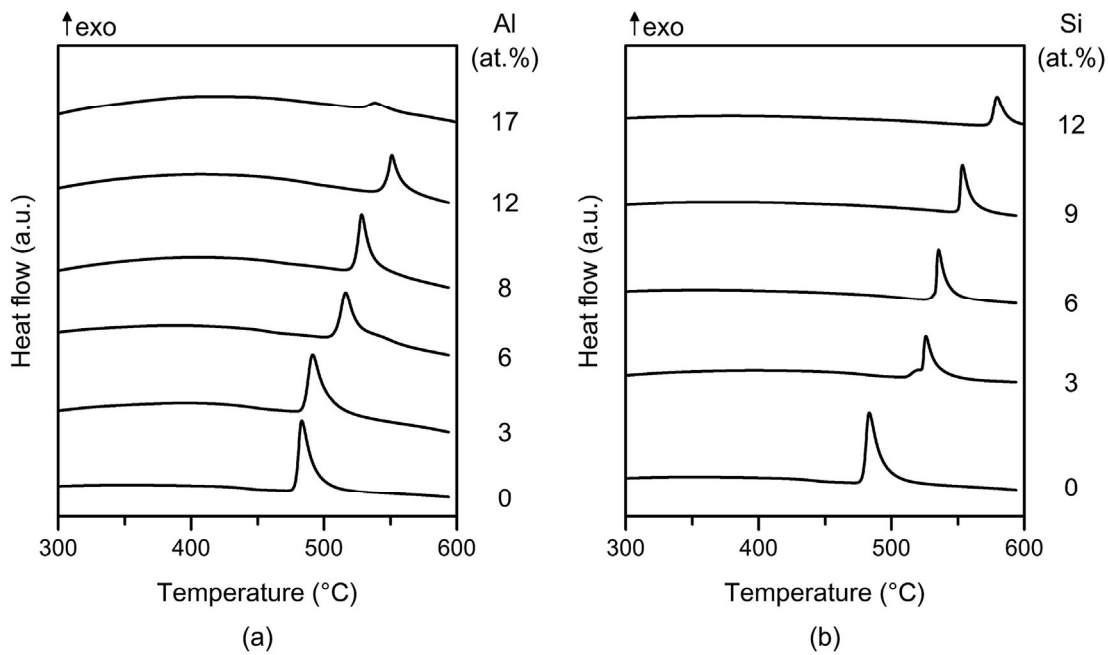


Fig. 4. DSC curves of the films of the (a) Al-series and (b) Si-series acquired at a heating rate of 30 °C/min in Ar.

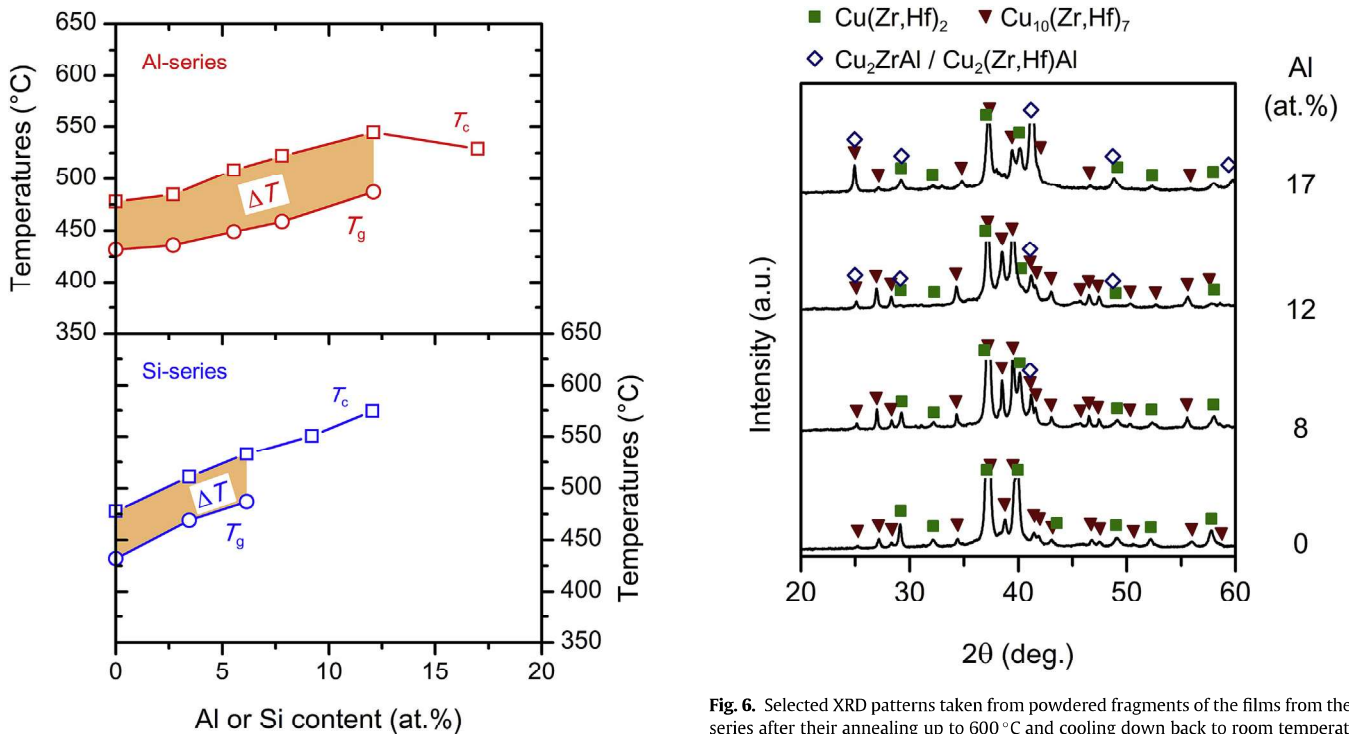


Fig. 5. Crystallization temperature T_c (open squares), glass transition temperature T_g (open circles) and the supercooled liquid region ΔT (orange area) of the films from the Al- and Si-series. (For interpretation of the references to colour in this figure legend, the reader is referred to the Web version of this article.)

scanning calorimetry. Freestanding fragments of each film from both series were annealed up to 600 °C in Ar. Fig. 4a gathers DSC curves of the films of the Al-series. As can be seen, one well-defined exothermic peak is detected up to 12 at.% Al. This peak, related to the crystallization of the film, is shifted to higher temperatures with increasing Al content. The onset of the peak defines the

crystallization temperature, T_c . The DSC curve of the film with 17 at.% Al is also characterized with one exothermic peak, which is, however, detected at a lower temperature compared to the film with 12 at.% Al and has a significantly lower intensity. A similar set of the DSC curves was also observed for the Si-series except that the film with 3 at.% Si is characterized by a low-intensity exothermic peak followed by a second high intensity exothermic peak, see Fig. 4b. It can be also seen in Fig. 4a and b that the exothermic peak

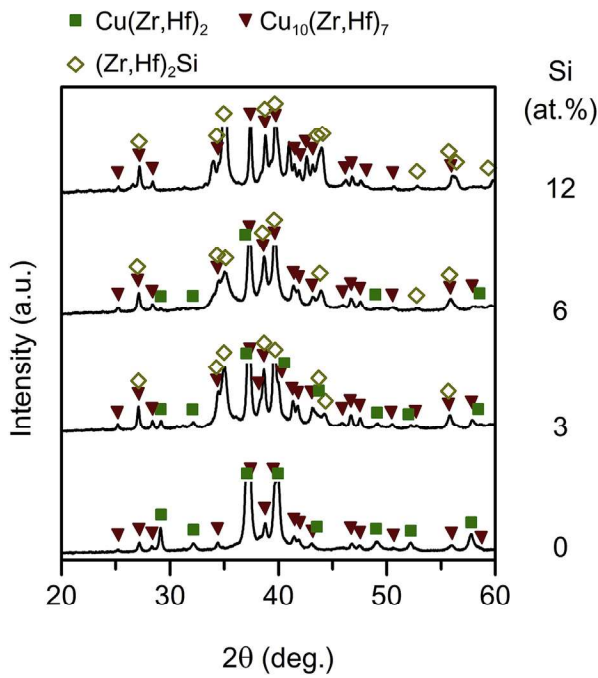


Fig. 7. Selected XRD patterns taken from powdered fragments of the films from the Si-series after their annealing up to 600 °C and cooling down back to room temperature. The main diffraction peaks of the Cu(Zr,Hf)₂, Cu₁₀(Zr,Hf)₇ and (Zr,Hf)₂Si phases are marked by the symbols.

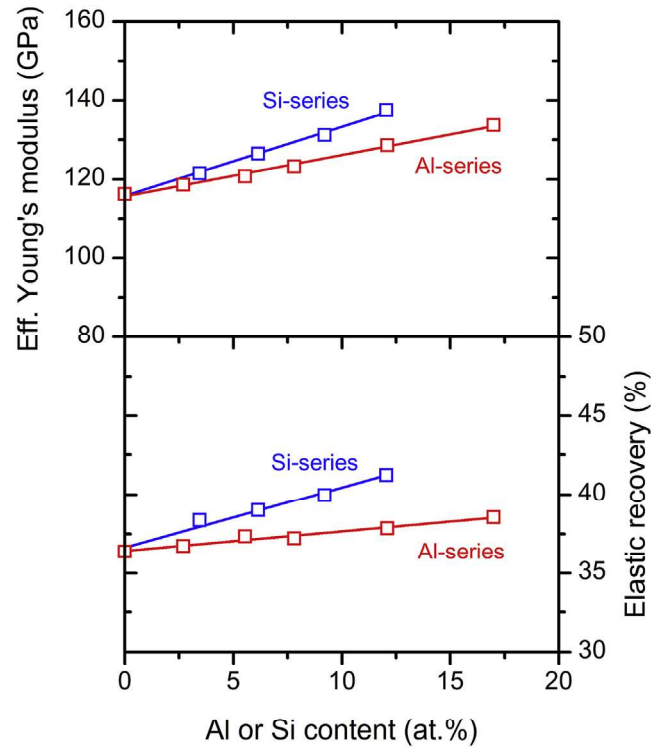


Fig. 9. Effective Young's modulus and elastic recovery of the films of the Al- and Si-series as a function of the Al or Si content.

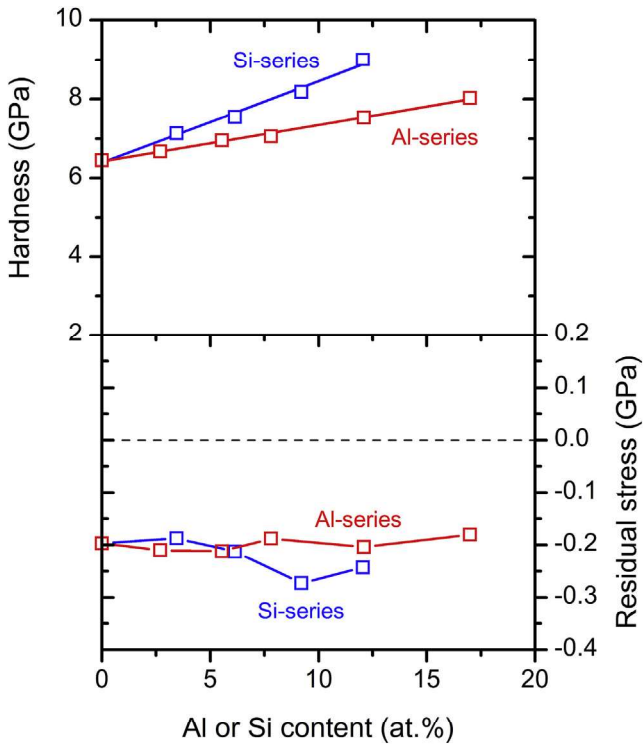


Fig. 8. Hardness and residual stress of the films of the Al- and Si-series as a function of the Al or Si content.

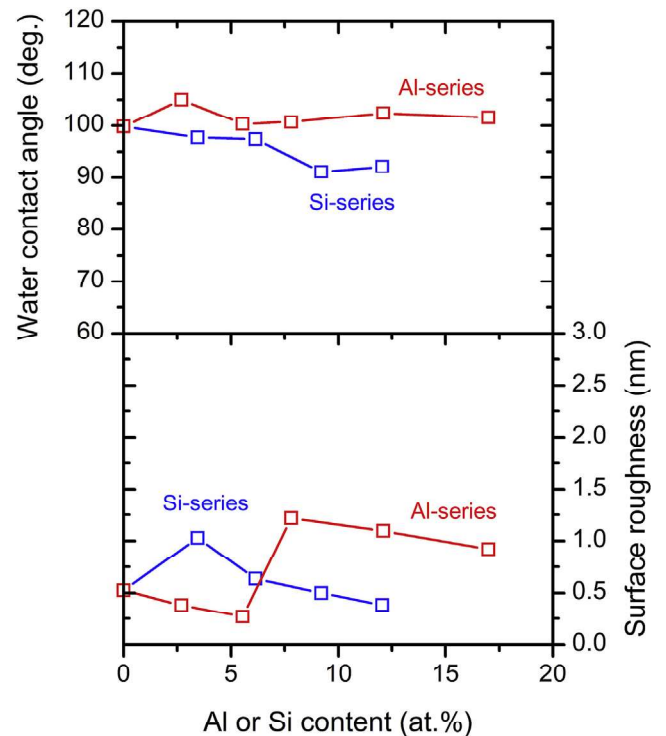


Fig. 10. Water contact angle and surface roughness of the films of the Al- and Si-series as a function of the Al or Si content.

of the films of the Si-series was located at a higher temperature for the comparable amount of Si and Al. The shift of the exothermic peak to higher temperatures with increasing either Al or Si up to 12 at.% indicates an enhanced thermal stability of the amorphous

state of the quaternary Zr–Hf–Al/Si–Cu films compared to the ternary Zr–Hf–Cu films. This behavior may be attributed to more difficult diffusion of the atoms in the film upon heating due to the

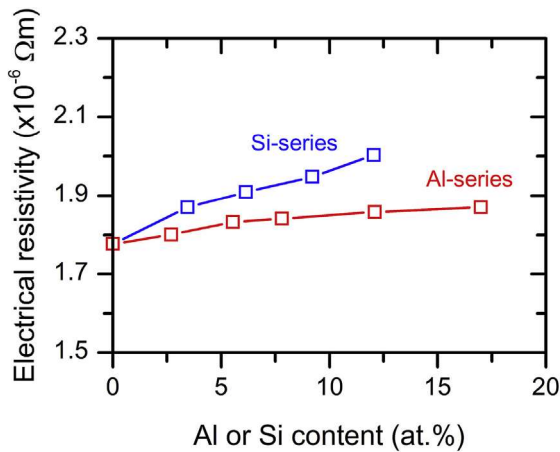


Fig. 11. Electrical resistivity of the films of Al- and Si-series as a function of the Al or Si content.

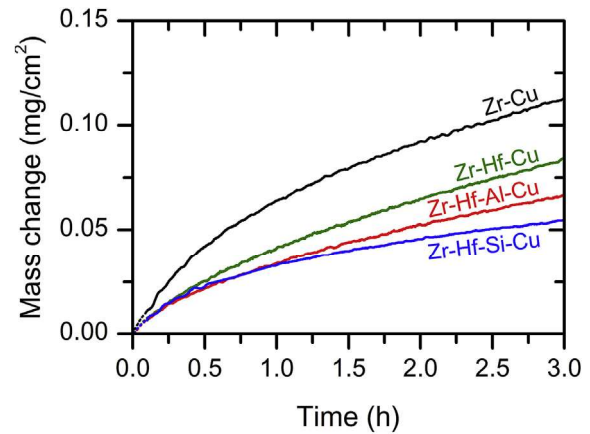


Fig. 13. Isothermal thermogravimetric oxidation curves of the Zr–Cu, Zr–Hf–Cu, Zr–Hf–Al–Cu and Zr–Hf–Si–Cu films with a constant Cu value of 46 at.%, constant ratio $[Hf]:[Zr] \approx 1$ and 3 at.% of Al or Si measured at 550 °C in a synthetic air for 3 h.

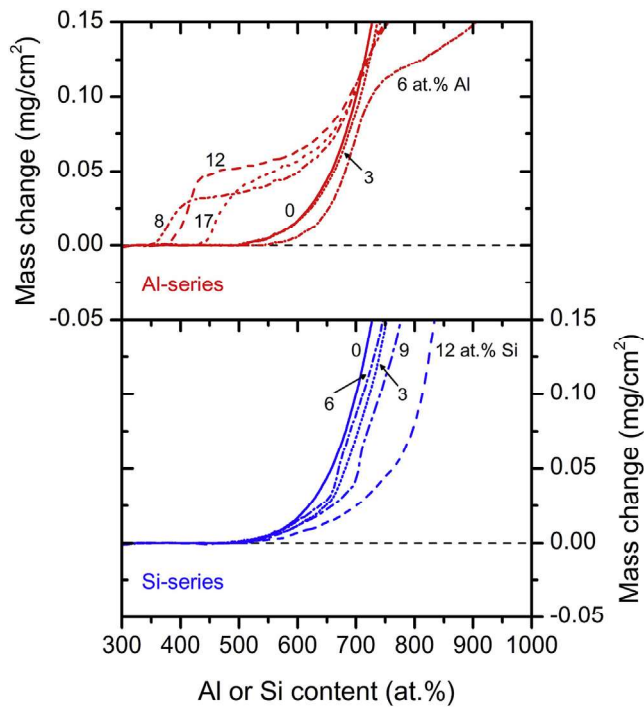


Fig. 12. Dynamical thermogravimetric oxidation curves of the films of the Al- and Si-series acquired at a heating rate of 10 °C/min in a flowing synthetic air.

presence of Al or Si with a stronger covalent bonding (more details given later).

Before the onset of the crystallization peak, we observed a decrease of a heat flow for some Zr–Hf–Al/Si–Cu films. This kind of decrease is a typical behavior of glasses and is known as a glass transition. The glass transition determines the position of the glass transition temperature, T_g (for more details see our previous paper [23]). The supercooled liquid region, ΔT , in which the glass exhibits a viscous flow and thermoplastic behavior, is located between T_g and T_c .

Fig. 5 presents the evolution of T_g and T_c for both series as a function of the Al or Si content. One may notice that we were able to recognize the glass transition only between 0 and 12 at.% Al for the films of the Al-series and between 0 and 6 at.% Si for the films of the Si-series. As can be seen in Fig. 5, the values of T_c increase

monotonically up to 12 at.% of Al or Si with increasing the Al or Si content in the films. Further increase of the Al content causes a decrease of T_c . The values of T_g follow the trend of T_c . The supercooled liquid region is marked in Fig. 5 by the orange area between T_g and T_c . An addition of Al into the ternary Zr–Hf–Cu films extends the supercooled liquid region. The maximum $\Delta T = 63$ °C was achieved for the film with 8 at.% Al. On the other hand, addition of 3 at.% Si reduces the width of the supercooled region while addition of 6 at.% Si gives again the value of the ternary Zr–Hf–Cu film. The values of T_g , T_c and ΔT for the films from Al- and Si-series are summarized in Table 1. As for the addition of Al its effect in the Zr–Hf–Al–Cu films is comparable with reported results for the ternary Zr–Al–Cu metallic glasses [9,13,14]. For instance, Cheung and Shek [14] observed glass transition in the range from 0 to 10 at.% Al with a maximum value of $\Delta T = 73$ °C for 8 at.% Al. Regarding the alloying with Si, its effect is also similar with results published in the literature for the Zr-based BMG [11] except that we were able to prepare metallic glasses in a wider composition range up to 6 at.% Si but we did not observe extending of the supercooled liquid region in the investigated region.

In order to identify products of the crystallization of the films of the Al- and Si-series, XRD analysis was carried out after the DSC measurements. Prior the analysis, the film fragments were ground to powder. As expected from the DSC curves, all films crystallized upon the annealing to 600 °C. The XRD patterns of the representative films of the Al-series are shown in Fig. 6. The ternary Zr–Hf–Cu film consists of the tetragonal $Cu(Zr,Hf)_2$ and orthorhombic $Cu_{10}(Zr,Hf)_7$ solid solution phases. This is in accordance with our previous paper [24] where we showed that Hf gradually substitutes Zr with increasing $Hf/(Hf+Zr)$ ratio. The positions of the XRD peaks are just in the middle of the positions corresponding to the tetragonal $CuZr_2$ (PDF Card No. 00-018-0466) and $CuHf_2$ (PDF Card No. 04-004-2396) phases and the orthorhombic $Cu_{10}Zr_7$ (PDF Card No. 01-078-3211) and $Cu_{10}Hf_7$ (PDF Card No. 01-082-6313) phases, which reflects well the equal content of Zr and Hf in the films. An addition of Al into the Zr–Hf–Cu films results in a quite complex structure which in turn complicates the identification of the crystallization products. In spite of this fact, some conclusions can be drawn from the XRD analysis of the patterns. An increasing Al content to 8 at.% results in the appearance of another peak at a 2θ position of about 41.25° . The position of this peak is very close to the positions of the ternary cubic Cu_2ZrAl (PDF Card No. 03-065-6362) and Cu_2HfAl (PDF Card No. 04-008-2257) phases. It cannot be, however, ruled out that it also may correspond to the cubic

Table 1

Glass transition temperature T_g , crystallization temperature T_c and supercooled liquid region $\Delta T = T_c - T_g$ of the films from the Al- and Si-series.

Al-series						
Al (at.%)	0	3	6	8	12	17
T_g (°C)	432	436	449	459	487	–
T_c (°C)	478	485	509	522	545	529
ΔT (°C)	46	49	60	63	58	–
Si-series						
Si (at.%)	0	3	6	9	12	–
T_g (°C)	432	469	487	–	–	–
T_c (°C)	478	511	533	551	574	–
ΔT (°C)	46	42	46	–	–	–

$\text{Cu}_2(\text{Zr,Hf})\text{Al}$ solid solution phase. With further increase of the Al content, the intensity of the peak increases and also new peaks related to this cubic phase appear. Other peaks in the XRD patterns (≥ 8 at. % Al) can be ascribed to the tetragonal $\text{Cu}(\text{Zr,Hf})_2$ and orthorhombic $\text{Cu}_{10}(\text{Zr,Hf})_7$ phases but with a variable content of Zr and Hf. Some peaks are closer to the CuZr_2 while other to the CuHf_2 diffraction standards. The same is valid for the orthorhombic phase.

The XRD patterns of the representative films of the Si-series are shown in Fig. 7. The results demonstrate much higher reactivity of Si with Zr and Hf than with Cu. A small addition of Si (3 at.%) leads to the crystallization of a silicide phase. Since the positions of the XRD peaks of this phase are in between the positions of the cubic Zr_2Si (PDF Card No. 04-001-0938) and Hf_2Si (PDF Card No. 04-001-0944) diffraction standards, it implies that this phase can be considered to be the cubic $(\text{Zr,Hf})_2\text{Si}$ solid solution. Its amount grows with increasing Si content as deduced from increasing intensity of the corresponding XRD peaks. Simultaneously, the crystallization of the tetragonal $\text{Cu}(\text{Zr,Hf})_2$ phase is limited due to the consumption of Zr and Hf and this phase gradually vanishes. In contrast, the orthorhombic $\text{Cu}_{10}(\text{Zr,Hf})_7$ phase is present for all Si contents investigated. Moreover, the XRD peaks of this phase remain at the same positions independently of the Si content. This is different from the effect of the Al addition.

3.4. Mechanical properties

The effect of the elemental composition on the hardness and the residual stress of the Zr–Hf–Al/Si–Cu films is shown in Fig. 8. It can be seen in the upper panel of Fig. 8 that the hardness of the films of the Al- and Si-series increases monotonically from 6.5 to 8.0 GPa and from 6.5 to 9.0 GPa, respectively. In both series the dependencies can be well fitted by straight lines. It is also clearly seen that the straight line of the Si-series is considerably steeper indicating a more pronounced effect of the Si addition on the hardness enhancement. A maximum value of the hardness of the Zr–Hf–Al/Si–Cu films, which exhibit the metallic glass behavior, is 7.5 GPa and was measured for two films containing either 12 at.% Al or 6 at.% Si. The residual stress for the films of the Al- and Si-series is shown in the bottom panel of Fig. 8. Both film series exhibit a compressive residual stress with the absolute values varying around 0.2 GPa. We have not observed a significant difference in the values of the residual stress with the addition of Al or Si. The compressive residual stress of these films can be attributed to the bombardment of the growing film by energetic Cu ions generated in the discharge in the vicinity of the Cu target sputtered in a high-power impulse regime (for more details see our previous publication [23]). A low or moderate compressive residual stress is generally beneficial in terms of increasing hardness and suppressing crack propagation.

Fig. 9 shows the evolution of the effective Young's modulus and the elastic recovery as a function of the Al or Si content in the films. It is clearly seen that the evolution of both quantities follows the trend of the hardness. The effective Young's modulus increases from 116 to 134 GPa and from 116 to 138 GPa for the Al- and Si-series, respectively. In case of the elastic recovery, the values increase from 36 to 39% and from 36 to 41% for the Al- and Si-series, respectively. The values of the effective Young's modulus as well as the values of the elastic recovery may be also fitted with straight lines with a higher slope for the Si-series. Despite the increase of the elastic recovery from 36% for the ternary Zr–Hf–Cu film, the Zr–Hf–Al/Si–Cu films still deform predominantly plastically via the formation of shear bands.

A clear correlation can be seen when comparing the evolution of T_g and T_c (see Fig. 5) and the evolution of mechanical properties (see Figs. 8 and 9) of the Zr–Hf–Al/Si–Cu metallic glasses. All aforementioned quantities increase with increasing Al or Si content in the films. This behavior may be understood in terms of an average bond energy in the films. Note that the main-group elements, Si and Al, possess p-electrons in their isolated-atom electronic configurations unlike Zr and Hf which are replaced. Thus, a case can be made that the incorporation of Al or Si into the films increases the projection of the resulting hybridized orbitals on odd p-orbitals (contrary to even s- and d-orbitals). The non-zero weight of electrons on odd p-orbitals leads to wavefunctions centered between atoms rather than on an atom, i.e. to a more directional (covalent) bonding [27].

3.5. Surface properties

The surface properties, namely the wettability and surface roughness, of the films of the Al- and Si-series are displayed in Fig. 10 as a function of the Al or Si content. The wettability of the films was characterized by the water contact angle which is shown in the upper panel of Fig. 10. As can be seen, the values of the water contact angle of the films of the Al-series scatter around 100°. On the other hand, the films from the Si-series with Si content up to 6 at.% exhibit a slightly lower water contact angle of about 97°. Further increase of the Si content leads to a more pronounced decrease of the water contact angle to the values slightly below 90°. Thus, only the films with up to 17 at.% Al or 6 at.% Si can be considered as hydrophobic.

The arithmetic average surface roughness of the films of the Al- and Si-series is shown in the bottom panel of Fig. 10. As can be seen, the low addition of Al up to 6 at.% leads to a decrease of the surface roughness from approximately 0.5 nm for the ternary Zr–Hf–Cu film to less than 0.3 nm. An increase of the Al content to 8 at.% causes a rise of the surface roughness to 1.2 nm. Further increase of the Al content leads to a moderate decrease of the surface roughness which, however, does not reach the value of the ternary Zr–Hf–Cu film. In case of the Si-series, the addition of 3 at.% Si induces an increase of the surface roughness to approximately 1 nm followed by a gradual decrease to the values lower than 0.4 nm. Despite the fact that a few films containing either Al or Si exceed the value of the surface roughness of the ternary Zr–Hf–Cu film, the Zr–Hf–Al/Si–Cu films are still very smooth, especially when compared with crystalline alloys [23].

3.6. Electrical resistivity

Fig. 11 summarizes the values of the electrical resistivity of the films of the Al- and Si-series at room temperature. As can be seen the electrical resistivity increases monotonically for both series with increasing Al or Si content. The increase is more pronounced for the films of the Si-series which correlates well with the

evolution of the mechanical properties and characteristic temperatures. Therefore, the increase can be attributed to a more covalent character of the mixed metallic-covalent bonds compared to the ternary Zr–Hf–Cu film leading to less free electrons. Despite the fact that the electrical resistivity increases with increasing Al or Si content all deposited films exhibit very low electrical resistivity lower than $2.0 \times 10^{-6} \Omega \text{ m}$.

3.7. Oxidation resistance

Dynamical thermogravimetric oxidation curves of the films of the Al- and Si-series measured from room temperature up to 1000 °C in synthetic flowing air at a heating rate of 10 °C/min are shown in Fig. 12. It can be seen that the onset of the oxidation depends on the content of the additional element. All films of the Si-series, see the bottom panel of Fig. 12, start to oxidize at about 500 °C but as the temperature increases the oxidation rate decreases with increasing Si content. This may be explained by the formation of a Si-containing surface oxide layer that serves as a more efficient barrier against interdiffusion of oxygen and elements of the film.

In case of the Al-series the evolution of the oxidation resistance is more complex. We recognize two main intervals of the Al content which differ in the oxidation behavior, see the upper panel of Fig. 12. Up to 6 at.% Al, the addition of Al has positive effect on the oxidation resistance and the onset of the oxidation shifts to higher temperatures. For instance, the film containing 6 at.% Al starts to oxidize at about 550 °C. However, when the Al content is above 6 at.% Al, the onset of the oxidation of the films is registered at noticeably lower temperatures, e.g. at 350 °C for 8 at.% Al. The films start to rapidly oxidize gaining a mass change up to 0.05 mg/cm² after which the oxidation slows down. At about 550 °C, it accelerates again and the mass gain follows the trend of the films with 0 and 3 at.% Al. If one compares the onset of the crystallization (Fig. 5 and Table 1) with that of the oxidation (Fig. 12), one may notice that the Zr–Hf–Al–Cu films with the Al content between 0 and 6 at.% and the Zr–Hf–Si–Cu films with the Si content between 0 and 12 at.% exhibit very low mass gain before starting to crystallize.

Since the difference in the oxidation resistance of the Zr–Hf–Cu and Zr–Hf–Al/Si–Cu films with 3 at.% Al or Si was not so pronounced upon the dynamical heating, we carried out in addition isothermal oxidation measurements at 550 °C in a flowing synthetic air for 3 h. Fig. 13 presents the comparison of thermogravimetric curves of binary Zr₅₄Cu₄₆, ternary Zr₂₇Hf₂₇Cu₄₆, and quaternary Zr₂₅Hf₂₆Al₃Cu₄₆ and Zr₂₅Hf₂₆Si₃Cu₄₆ films. All films possess the same Cu content of 46 at.% and ternary/quaternary films a fixed ratio of [Hf]:[Zr] ≈ 1. The films were heated up to 550 °C as fast as possible (50 °C/min) to eliminate their oxidation before starting the isothermal measurements. The corresponding mass gain was therefore close to zero for all films. Because the thermogravimetric signal during the first 5 min was strongly affected by oscillations of the temperature signal due to the transition from the dynamical ramp heating to the isothermal steady-state heating, the thermogravimetric data were just extrapolated (see dashed lines) during the settling time.

As can be seen in Fig. 13, the quaternary Zr–Hf–Al/Si–Cu films containing Al or Si exhibit a lower oxidation rate and a lower mass gain after 3 h of the measurement compared to the binary Zr–Cu and ternary Zr–Hf–Cu films. The best oxidation resistance is achieved for the Zr₂₅Hf₂₆Si₃Cu₄₆ film. Its mass gain after 3 h is close to 0.055 mg/cm², which is approximately two times less than for the Zr₅₄Cu₄₆ film. This is in agreement with the measurement of the thickness of the surface oxide layer. For the Zr₂₅Hf₂₆Si₃Cu₄₆ film, the thickness of the oxide layer was 390 nm while for the Zr₅₄Cu₄₆

film was 840 nm. All oxidation curves can be well fitted with square-root functions. Oxidation in such a way indicates that a dense barrier oxide layer is formed on the surface of the films causing the reduction of the oxidation rate with time. The oxidation is then controlled by a diffusion of the species through the oxide layer [28]. From Fig. 13 it is seen that the Si-containing surface oxide layer is even more efficient than the Al-containing one. Let us also note that even if the binary Zr₅₄Cu₄₆ thin-film metallic glass exhibits the highest mass gain among the films investigated, it is more oxidation resistant than its crystalline counterpart of the identical composition. This will be, however, reported in detail in our separate paper along with crystallization and oxidation kinetics of the aforementioned films.

4. Conclusions

The effect of an addition of Al (up to 17 at.%) and Si (up to 12 at.%) into the Zr–Hf–Cu thin-film alloys on their properties and behavior was studied in detail. Conventional dc and high-power impulse magnetron co-sputtering of Zr, Hf, Al or Si and Cu in pure Ar was proved to be a suitable deposition technique for a reproducible deposition of quaternary Zr–Hf–Al/Si–Cu films.

The deposited thin-film metallic alloys were found to be amorphous in the whole studied range. The glass transition was, however, recognizable only up to 12 at.% Al and 6 at.% Si by differential scanning calorimetry. The increase of the Al and Si content led to an increase of the crystallization (up to 12 at.% Al and Si) and glass transition (up to 12 at.% Al and 6 at.% Si) temperature, and mechanical properties (up to 17 at.% Al and 12 at.% Si). This increase may be explained based on the increasing effect of a covalent component of the mixed metallic-covalent bonds between Al or Si and other elements of the films. Smooth, hydrophobic and electrically conductive Zr–Hf–Al/Si–Cu thin-film metallic glasses exhibit enhanced hardness, thermal stability and oxidation resistance. A wider super-cooled liquid region was obtained for the Zr–Hf–Al–Cu metallic glasses, while a better oxidation resistance for the Zr–Hf–Si–Cu metallic glasses.

Acknowledgments

The authors thank Dr. Jiří Houška, Dr. Šimon Kos and Dr. Stanislav Haviar for helpful discussions. This work was supported by the Czech Science Foundation under Project No. GA16-18183S.

References

- [1] M. Telford, The case for bulk metallic glass, *Mater. Today* 7 (2004) 36–43, [https://doi.org/10.1016/S1369-7021\(04\)00124-5](https://doi.org/10.1016/S1369-7021(04)00124-5).
- [2] M.F. Ashby, A.L. Greer, Metallic glasses as structural materials, *Scr. Mater.* 54 (2006) 321–326, <https://doi.org/10.1016/j.scriptamat.2005.09.051>.
- [3] A.L. Greer, Metallic glasses...on the threshold, *Mater. Today* 12 (2009) 14–22, [https://doi.org/10.1016/S1369-7021\(09\)70037-9](https://doi.org/10.1016/S1369-7021(09)70037-9).
- [4] J. Schroers, G. Kumar, T.M. Hodges, S. Chan, T.R. Kyriakides, Bulk metallic glasses for biomedical applications, *JOM* 61 (2009) 21–29, <https://doi.org/10.1007/s11837-009-0128-1>.
- [5] J.P. Chu, J.S.C. Jang, J.C. Huang, H.S. Chou, Y. Yang, J.C. Ye, Y.C. Wang, J.W. Lee, F.X. Liu, P.K. Liaw, Y.C. Chen, C.M. Lee, C.L. Li, C. Rullyani, Thin film metallic glasses: unique properties and potential applications, *Thin Solid Films* 520 (2012) 5097–5122, <https://doi.org/10.1016/j.tsf.2012.03.092>.
- [6] H.W. Sheng, W.K. Luo, F.M. Alamgir, J.M. Bai, E. Ma, Atomic packing and short-to-medium-range order in metallic glasses, *Nature* 439 (2006) 419–425, <https://doi.org/10.1038/nature04421>.
- [7] A.R. Yavari, Materials science: a new order for metallic glasses, *Nature* 439 (2006) 405–406, <https://doi.org/10.1038/439405a>.
- [8] D.Z. Chen, C.Y. Shi, Q. An, Q. Zeng, W.L. Mao, W.A. Goddard, J.R. Greer, Fractal atomic-level percolation in metallic glasses, *Science* 349 (2015) 1306–1310, <https://doi.org/10.1126/science.aab1233>.
- [9] A. Inoue, T. Zhang, T. Masumoto, The structural relaxation and glass transition of La–Al–Ni and Zr–Al–Cu amorphous alloys with a significant supercooled liquid region, *J. Non-Cryst. Solids* 150 (1992) 396–400, <https://doi.org/>

- 10.1016/0022-3093(92)90160-L.
- [10] H. Choi-Yim, R. Busch, W.L. Johnson, The effect of silicon on the glass forming ability of the Cu₄₇Ti₃₄Zr₁₁Ni₈ bulk metallic glass forming alloy during processing of composites, *J. Appl. Phys.* 83 (1998) 7993–7997, <https://doi.org/10.1063/1.367981>.
- [11] W.H. Wang, Z. Bian, Ping Wen, Y. Zhang, M.X. Pan, D.Q. Zhao, Role of addition in formation and properties of Zr-based bulk metallic glasses, *Intermetallics* 10 (2002) 1249–1257, [https://doi.org/10.1016/S0966-9795\(02\)00140-1](https://doi.org/10.1016/S0966-9795(02)00140-1).
- [12] P. Yu, H.Y. Bai, M.B. Tang, W.L. Wang, Excellent Glass-forming Ability in Simple Cu₅₀Zr₅₀-based Alloys, 2005, <https://doi.org/10.1016/j.jnoncrysol.2005.03.012>.
- [13] G. Kumar, T. Ohkubo, T. Mukai, K. Hono, Plasticity and microstructure of Zr–Cu–Al bulk metallic glasses, *Scr. Mater.* 57 (2007) 173–176, <https://doi.org/10.1016/j.scriptamat.2007.02.013>.
- [14] T.L. Cheung, C.H. Shek, Thermal and mechanical properties of Cu–Zr–Al bulk metallic glasses, *J. Alloys Compd.* 434 (2007) 71–74, <https://doi.org/10.1016/j.jallcom.2006.08.109>.
- [15] B. Zhang, Y. Jia, S. Wang, G. Li, S. Shan, Z. Zhan, R. Liu, W. Wang, Effect of silicon addition on the glass-forming ability of a Zr–Cu-based alloy, *J. Alloys Compd.* 468 (2009) 187–190, <https://doi.org/10.1016/j.jallcom.2008.01.098>.
- [16] Y.T. Sun, C.R. Cao, K.Q. Huang, N.J. Zhao, L. Gu, D.N. Zheng, W.H. Wang, Understanding glass-forming ability through sluggish crystallization of atomically thin metallic glassy films, *Appl. Phys. Lett.* 105 (2014), 051901, <https://doi.org/10.1063/1.4892448>.
- [17] J. Chu, C. Liu, T. Mahalingam, S. Wang, M. O'Keefe, B. Johnson, C. Kuo, Annealing-induced full amorphization in a multicomponent metallic film, *Phys. Rev. B* 69 (2004), 113410, <https://doi.org/10.1103/PhysRevB.69.113410>.
- [18] P.-T. Chiang, G.-J. Chen, S.-R. Jian, Y.-H. Shih, J.S.-C. Jang, C.-H. Lai, Surface antimicrobial effects of Zr₆₁Al_{7.5}Ni₁₀Cu_{17.5}Si₄ thin film metallic glasses on *Escherichia coli*, *Staphylococcus aureus*, *Pseudomonas aeruginosa*, *acinetobacter baumannii* and *Candida albicans*, *Fooyin J. Heal. Sci.* 2 (2010) 12–20, [https://doi.org/10.1016/S1877-8607\(10\)60008-2](https://doi.org/10.1016/S1877-8607(10)60008-2).
- [19] P. Coddet, F. Sanchette, J.C. Rousset, O. Rapaud, C. Coddet, On the elastic modulus and hardness of co-sputtered Zr–Cu–(N) thin metal glass films, *Surf. Coating. Technol.* 206 (2012) 3567–3571, <https://doi.org/10.1016/j.surfcoat.2012.02.036>.
- [20] M. Apreutesei, P. Steyer, L. Joly-Pottuz, A. Billard, J. Qiao, S. Cardinal, F. Sanchette, J.M. Pelletier, C. Esnouf, Microstructural, thermal and mechanical behavior of co-sputtered binary Zr–Cu thin film metallic glasses, *Thin Solid Films* 561 (2014) 53–59, <https://doi.org/10.1016/j.tsf.2013.05.177>.
- [21] Y.-L. Deng, J.-W. Lee, B.-S. Lou, J.-G. Duh, J.P. Chu, J.S.-C. Jang, The fabrication and property evaluation of Zr–Ti–B–Si thin film metallic glass materials, *Surf. Coating. Technol.* 259 (2014) 115–122, <https://doi.org/10.1016/j.surfcoat.2014.03.026>.
- [22] P.C. Wang, J.W. Lee, Y.C. Yang, B.S. Lou, Effects of silicon contents on the characteristics of Zr–Ti–Si–W thin film metallic glasses, *Thin Solid Films* 618 (2016) 28–35, <https://doi.org/10.1016/j.tsf.2016.03.043>.
- [23] P. Zeman, M. Zitek, S. Zuzjaková, R. Čerstvý, Amorphous Zr–Cu thin-film alloys with metallic glass behavior, *J. Alloys Compd.* 696 (2017) 1298–1306, <https://doi.org/10.1016/j.jallcom.2016.12.098>.
- [24] M. Zitek, P. Zeman, S. Zuzjaková, M. Kotrlová, R. Čerstvý, Tuning properties and behavior of magnetron sputtered Zr–Hf–Cu metallic glasses, *J. Alloys Compd.* 739 (2018) 848–855, <https://doi.org/10.1016/j.jallcom.2017.12.301>.
- [25] W.C. Oliver, G.M. Pharr, An improved technique for determining hardness and elastic modulus using load and displacement sensing indentation experiments, *J. Mater. Res.* 7 (1992) 1564–1583, <https://doi.org/10.1557/JMR.1992.1564>.
- [26] W. Eckstein, *Sputtering yields*, in: *Sputtering by Part. Bombard*, Springer, Berlin, 2007.
- [27] J. Houska, S. Kos, Ab initio modeling of complex amorphous transition-metal-based ceramics, *J. Phys. Condens. Matter* 23 (2011), <https://doi.org/10.1088/0953-8984/23/2/025502>.
- [28] S. Bose, *High Temperature Coatings*, first ed., Elsevier Inc., 2007 <https://doi.org/10.1016/B978-0-7506-8252-7.X5000-8>.

Part D

Flexible antibacterial Zr–Cu–N thin films resistant to cracking

J. Musil, M. Zítek, K. Fajfrlík, R. Čerstvý

Journal of Vacuum Science & Technology A 34, 021508 (2016)

Flexible antibacterial Zr-Cu-N thin films resistant to cracking

Jindřich Musil^{a)}

Department of Physics and NTIS – European Centre of Excellence, University of West Bohemia, Univerzitní 8, 306 14 Plzeň, Czech Republic and National Research Tomsk Polytechnic University, 30 Lenin Avenue, 634050 Tomsk, Russia

Michal Zítek

Department of Physics and NTIS – European Centre of Excellence, University of West Bohemia, Univerzitní 8, 306 14 Plzeň, Czech Republic

Karel Fajfrlík

Department of Microbiology, Medical Faculty in Plzeň, Charles University in Praha, E.Beneše 13, CZ-30599 Plzeň, Czech Republic

Radomír Čerstvý

Department of Physics and NTIS – European Centre of Excellence, University of West Bohemia, Univerzitní 8, 306 14 Plzeň, Czech Republic

(Received 3 September 2015; accepted 30 November 2015; published 16 December 2015)

This study investigates how the Cu concentration in Zr-Cu-N films affects the films' antibacterial capacity and mechanical properties. Zr-Cu-N films were prepared by reactive magnetron sputtering from composed Zr/Cu targets using a dual magnetron in an Ar + N₂ mixture. The antibacterial capacity of Zr-Cu-N films was tested on *Escherichia coli* (*E. coli*) bacteria. The mechanical properties of Zr-Cu-N films were determined from the load vs. displacement curves measured using a Fisherscope H 100 microhardness tester. The antibacterial capacity was modulated by the amount of Cu added to the Zr-Cu-N film. The mechanical properties were varied based on the energy E_i delivered to the growing film by bombarding ions. It was found that it is possible to form Zr-Cu-N films with Cu concentrations ≥ 10 at. % that simultaneously exhibit (1) 100% killing efficiency E_k for *E. coli* bacteria on their surfaces, and (2) (1) high hardness H of about 25 GPa, (2) high ratio $H/E^* \geq 0.1$, (3) high elastic recovery $W_e \geq 60\%$ and (4) compressive macrostress ($\sigma < 0$). The Zr-Cu-N films with these parameters are flexible/antibacterial films that exhibit enhanced resistance to cracking. This enhanced resistance was tested by (1) bending the Mo and Ti strip coated by sputtered Zr-Cu-N films (bending test) and (2) loading the surface of the Zr-Cu-N sputtered on a Si substrate by a diamond indenter at high loads up to 1 N (indentation test). Physical, mechanical, and antibacterial properties of Zr-Cu-N films are described in detail. In summary, it can be concluded that Zr-Cu-N is a promising new material for creating flexible antibacterial coatings on contact surfaces. © 2015 American Vacuum Society.

[<http://dx.doi.org/10.1116/1.4937727>]

I. INTRODUCTION

In recent years, much attention has been focused on developing films that efficiently kill bacteria on their surfaces. Films containing silver (Ag)^{1–14} and copper (Cu)^{15–33} have been developed for this purpose. It was found that both kinds of films efficiently kill bacteria if the concentrations of Ag or Cu are above a threshold value, typically ~ 10 at. % or greater. Films containing Cu are preferable because unlike Ag, Cu is an essential trace element and can be released from the human body.¹⁵ Thus, research efforts have shifted to developing antibacterial Cu-containing films in recent years.

However, thus far, little attention has been devoted to mechanical properties of antibacterial films and particularly to correlations between the efficiency of killing bacteria and the mechanical properties of antibacterial films. A higher concentration of Ag or Cu in the film is beneficial for enhancing the efficiency of killing bacteria and shortening the time necessary to kill bacteria. The tradeoff is that these

higher concentrations also decrease hardness H , elastic recovery W_e , and the ratio H/E^* [here, the effective Young's modulus $E^* = E/(1 - \nu^2)$, E is the Young's modulus, and ν is the Poisson's ratio]. High concentrations of Ag or Cu in the films almost always result in dramatic decreases in hardness H . These antibacterial films offer little mechanical protection from external loads, especially against scratching and cracking upon bending. When such coatings are deposited onto flexible substrates, they easily crack and/or delaminate from protective surfaces. Therefore, it is vitally important to develop flexible films that will simultaneously efficiently kill bacteria on their surface and exhibit enhanced resistance to mechanical damage. These films show great potential for many applications and can be immediately deposited by industrial means onto contact surfaces of both rigid and flexible substrates. Examples of applications are for airplanes, buses, trains and trams, cash and ticket machines, furniture in restaurants, theaters, schools, and other objects.

We recently developed antibacterial/flexible/protective Al-Cu-N films that very effectively kill *Escherichia coli* bacteria and simultaneously exhibit enhanced resistance against

^{a)}Electronic mail: musil@kfy.zcu.cz

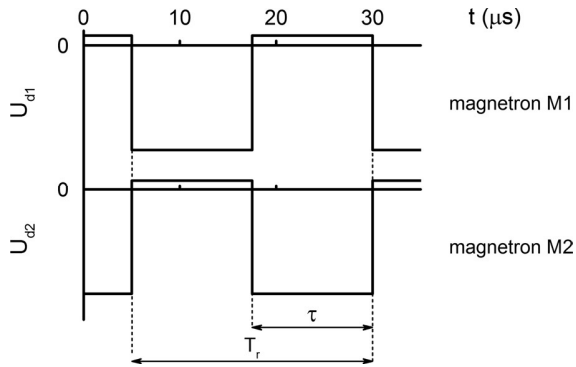


FIG. 1. Schematic illustration of discharge voltage U_d at both magnetrons of the dual magnetron operated in pulsed bipolar mode.

mechanical damage, especially to cracking upon bending when films are deposited on flexible substrates.³⁴ The physical, antibacterial, and mechanical properties of the Zr-Cu-N films are described in detail. However, different applications require different material systems, and so antibacterial coatings must be developed for other material systems. In this study, we demonstrate that the formation of antibacterial coatings is possible.

II. EXPERIMENT

The Zr-Cu-N films were reactively sputtered by a dual magnetron in Ar + N₂ sputtering gas mixture. The dual magnetron consists of two magnetically closed magnetrons tilted with respect to the vertical axis at an angle of 20°. Both magnetrons were equipped with the same Zr/Cu targets ($\varnothing = 50$ mm) composed of Zr (99.9 at. %) circular plates fixed to the cathode body with a Cu (99.9 at. %) fixing ring with inner diameter $\varnothing_{i\text{Cu}}$. The concentration of Cu in the Zr-Cu-N films was controlled by (1) $\varnothing_{i\text{Cu}}$ ranging from 32 to 34 mm and (2) partial pressure of nitrogen p_{N_2} . The dual magnetron was supplied by a floating DC pulsed power supply RMP-10 (Huttinger Electronics, Inc.) operated in a bipolar mode at a repetition frequency $f_r = 1/T_r = 40$ kHz ($T_r = 25$ μ s); here, T_r is the period of pulses (see Fig. 1).

The films were sputtered onto the Si(100) ($20 \times 20 \times 0.625$ mm³) and Si(111) ($35 \times 5 \times 0.38$ mm³) substrates and molybdenum and titanium ($50 \times 10 \times 0.15$ mm³) strips

held either at the floating potential $U_s = U_{fl}$ or at negative pulsed DC of -100 V. The substrate pulsed DC bias was supplied by a pulsed IAP 1010 power supply (EN Technologies) at a repetition frequency $f_{rs} = 1/T_s = 20$ kHz ($T_s = 50$ μ s) with a negative pulse-on time of 25 μ s, and pulse-off time of 25 μ s ($U_s = 0$ for 2.5 μ s, $U_s = 15$ V for 20 μ s, $U_s = 2.5$ V for 2.5 μ s); here, T_s is the period of negative pulses at the substrate (see Fig. 2). Figure 2 shows the time evolution of U_s and I_s at the substrate located in the dual magnetron discharge sustained at $I_{da} = 1$ A, $U_d = 320$ V, and $p_T = p_{Ar} + p_{N_2} = 1$ Pa; here, I_{da} is the magnetron discharge current averaged over the pulse-on time. The Zr-Cu-N films were sputtered at a substrate temperature $T_s = 450$ °C, substrate bias $U_s = -100$ V, substrate-to-target distance $d_{s-t} = 80$ mm, the partial pressure of nitrogen p_{N_2} ranging from 0.03 to 0.24 Pa, and the total sputtering gas pressure $p_T = p_{Ar} + p_{N_2} = 1$ Pa. The substrate ion current density $i_{sp} = I_s/S$ averaged over the time of the negative bias pulse was determined from the substrate current I_s waveforms monitored by a Tektronix TSP 2024 oscilloscope and the Tektronix TPCA 300 current probe; here, S is the surface area of the substrate holder.

The thickness h and the macrostress σ of sputtered Zr-Cu-N films were measured using a stylus profilometer Dektak 8. The macrostress σ was evaluated from the bending of a thin Si plate ($35 \times 5 \times 0.38$ mm³) covered by the film using Stoney's formula. The coating structure was characterized by x-ray diffraction analysis using an XRD diffractometer PANalytical X'pert PRO in the Bragg-Brentano configuration using CuK α radiation. The elemental composition of Zr-Cu-N films was measured by a PANalytical x-ray fluorescence (XRF) spectrometer MagiX PRO calibrated using pure Cu and ZrN films.

The antibacterial efficiency of the Zr-Cu-N films against *E. coli* bacteria was assessed by the plate-counting method. The efficiency E_k of killing bacteria settled on the film surface was calculated using the following formula:

$$E_k(\%) = \{(A - B)/A\} \times 100\%. \quad (1)$$

Here, A is the number of colonies of bacteria, called the bacteria colony forming units, grown from the suspension that was in contact with the surface of the reference Si substrate (without Zr-Cu-N film) and B is the number of

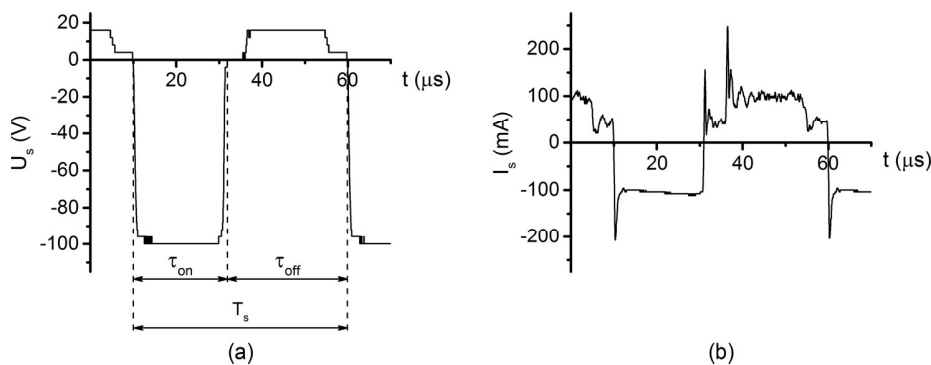


FIG. 2. Waveforms of the pulsed DC substrate bias (a) voltage U_s and (b) current I_s in bipolar operation of dual magnetron at $I_{da} = 1$ A, $U_d = 320$ V, and $p_T = p_{Ar} + p_{N_2} = 1$ Pa.

bacterial colonies grown from the suspension that was in contact with the Zr-Cu-N film covering the surface of a Si substrate. The antibacterial efficiency E_k was evaluated in the daylight for contact time $t_c = 5$ h.

The mechanical properties of films were determined from the load versus displacement curves obtained using the Fischerscope H100 microhardness tester with a Vickers diamond indenter at a load $L = 20$ mN. The measurements of mechanical properties of the film, i.e., the hardness H , effective Young's modulus E^* , and elastic recovery W_e , at the diamond indenter load $L = 20$ mN were not influenced by the substrate; the ratio of the indentation depth d and the film thickness h_f were smaller than 10%, which is the basic condition necessary for correct measurements.

The resistance of the film to cracking was determined using two methods: (1) the indentation test and (2) the bending test. In the indentation test, the resistance of film to cracking was evaluated from the Vickers diamond indenter imprint on the film surface at a high load of $L = 1$ N. For the bending test, the film was sputtered on a thin Mo and Ti strip ($50 \times 10 \times 0.15$ mm³), respectively, and the coated strip was bent around fixed cylinders of different radii r_{fc} until cracks in the film were observed. The resistance of film is defined as a critical film strain ϵ_{cr} . The critical strain ϵ_{cr} is the minimum strain ϵ_{min} at which cracks start to form. By decreasing the radius r_{fc} , the strain ϵ induced in the film was increased. Under the assumption that the thickness $h_{Mo/Ti}$ of the strip is much greater than the thickness h_f of the sputtered film, the critical strain ϵ_{cr} can be calculated from the following formula:^{34,35}

$$\epsilon_{cr} = h_{Mo/Ti}/2r_{fc}. \quad (2)$$

The surface morphology of the bent films was investigated using an optical microscope (OM) and a Hitachi SU-70 scanning electron microscope (SEM).

III. RESULTS AND DISCUSSION

The antibacterial properties of the Zr-Cu-N film were controlled by the concentration of Cu in the film. The mechanical behavior of the Zr-Cu-N film and its resistance to cracking were determined by its hardness H , effective Young's modulus E^* , ratio H/E^* , elastic recovery W_e , macrostress σ , and microstructure of the film.^{36–38} The amount of Cu in the Zr-Cu-N film strongly influences its mechanical properties. Therefore, the first goal was to determine the Cu concentration necessary to efficiently kill *E. coli* bacteria on the surface of the Zr-Cu-N film.

A. Structure of flexible Zr-Cu-N films

The structures of flexible Zr-Cu-N films with different Cu concentrations are shown in Fig. 3. The reference data for standard Cu, ZrN and ZrO₂ were taken from Ref. 40. From Fig. 3, it can be seen that the Zr-Cu-N films with low Cu concentrations have polycrystalline structures. The crystallinity of films decreases with the increasing Cu concentration. The Zr-Cu-N films with high Cu concentrations (>10 at. %) are nanocrystalline and even almost x-ray amorphous at very high (≥ 19 at. %) Cu concentrations. The x-ray

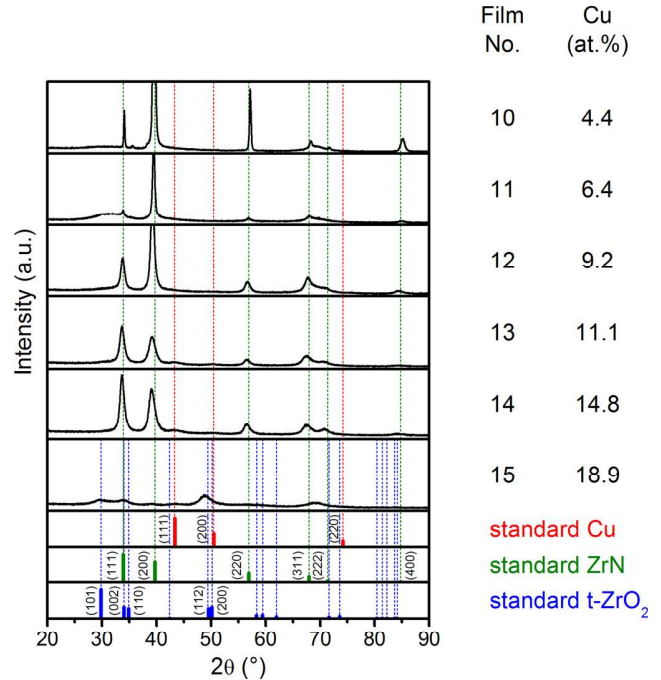


FIG. 3. (Color online) XRD patterns of Zr-Cu-N films sputtered at $U_s = -100$ V as a function of Cu content.

amorphous structure of the Zr-Cu-N films with >19 at. % Cu contains several broad, low-intensity peaks. These broad peaks correspond to small cubic ZrN grains and very likely also to small tetragonal ZrO₂ grains created from the oxygen contained in the residual atmosphere.³⁹ This indicates that these films are nanocomposites composed of small grains embedded in the a-(Zr-Cu-N) matrix. The exact identification of small grains requires more detailed analysis, which was beyond the scope of this study.

All Zr-Cu-N films with Cu concentrations ranging from 0 to ~ 20 at. % were flexible, but only the nanocrystalline Zr-Cu-N films with ≥ 9.2 at. % Cu exhibited a strong antibacterial capacity, which will be discussed in more detail in Sec. III C. This is an important finding because the Zr-Cu-N films with ≥ 9.2 at. % Cu simultaneously exhibit strong antibacterial capacity, high ratio $H/E^* \geq 0.1$, and high elastic recovery $W_e \geq 60\%$. The physical, mechanical, and antibacterial properties are given in Tables I and II and illustrated in Fig. 5. The structure of the sputtered films strongly depended on the energy delivered to the growing film by bombarding ions. Therefore, we cannot exclude the possibility that the efficiency of killing *E. coli* bacteria on the surface of the Zr-Cu-N films will also depend on their structure (see Ref. 29 for details). A change in structures of the Zr-Cu-N films means a change in its phase composition. The resulting chemical reactions at the film target strongly influence the efficiency of killing bacteria seeding on its surface.

B. Antibacterial properties of Zr-Cu-N films

The antibacterial capacity of the film surface is characterized by the efficiency E_k of killing bacteria settled on the

TABLE I. Main physical parameters of Zr-Cu-N films sputtered at $T_s = 450^\circ\text{C}$, $U_s = -100\text{ V}$, $p_T = p_{Ar} + p_{N_2} = 1\text{ Pa}$ on Si(100) substrate as a function of Cu content and used for the investigation of their mechanical properties given in Fig. 5; here, a_D in the deposition rate of film.

Film No.	p_{N_2} (Pa)	Cu (at. %)	h (nm)	a_D (nm/min)	i_{sp} (mA/cm ²)	E_{bi} (MJ/cm ³)	σ (GPa)
1	0.06	0.3	1430	15.9	1.50	9.5	-4.2
2	0.09	1.3	1790	17.9	1.20	6.8	-5.1
3	0.03	4.0	1280	16.0	1.38	8.6	-4.7
4	0.06	5.9	2060	13.8	1.53	11.1	-3.4
5	0.09	11.1	2360	13.9	1.40	10.1	-2.7
6 ^a	0.06	14.8	3470	27.8	1.04	3.8	-2.1
7 ^a	0.13	15.6	3040	21.7	1.27	5.9	-1.7
8 ^a	0.13	16.2	2650	22.1	1.02	4.6	-1.8
9	0.13	18.9	2440	13.1	1.40	10.7	-1.6

^aSputtering with new targets.

film surface. The efficiency E_k is calculated from Eq. (1) given in Sec. II above. Figure 4 shows the antibacterial efficiency E_k of Zr-Cu-N films with different Cu concentrations measured in the daylight as a function of Cu concentration, for contact time $t_c = 5\text{ h}$ of the bacteria with the film. From this figure, it is clear that the E_k value of the Zr-Cu-N film strongly depends on the concentration of Cu. The Zr-Cu-N films with $<10\text{ at. \%}$ Cu exhibit almost no antibacterial activity ($E_k \approx 0$). In contrast, the Zr-Cu-N films with $\geq 10\text{ at. \%}$ Cu very efficiently kill *E. coli* bacteria, and $E_k = 100\%$ was measured after 5 h contact with the film. This indicates that antibacterial Zr-Cu-N films must contain $\geq 10\text{ at. \%}$ Cu. However, the Cu concentration in the Zr-Cu-N film also strongly influences its mechanical properties and mechanical behavior under external loading.

C. Mechanical properties of Zr-Cu-N films

The mechanical properties of Zr-Cu-N films are strongly influenced by (1) the elemental composition of the film and (2) the energy E_i delivered to the film during its growth by

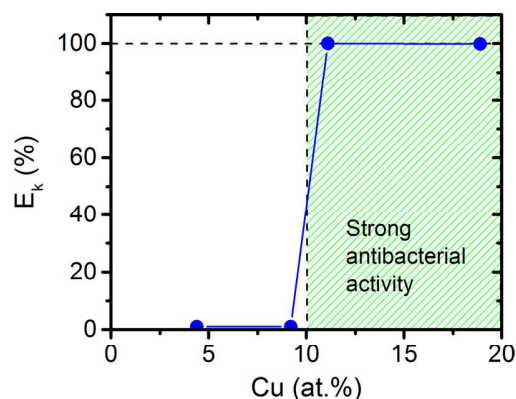


FIG. 4. (Color online) Antibacterial efficiency E_k of *E. coli* bacteria killing on the surface of Zr-Cu-N film as a function of Cu content for contact time $t_c = 5\text{ h}$ at daylight.

bombarding ions E_{bi} and fast neutrals E_{fn} . The energy E_{bi} is controlled by the negative substrate bias U_s and magnetron discharge current I_{da} . An increase in I_{da} , at an approximately the same voltage U_d , results in an increase in electron density N_e of the magnetron discharge plasma, and, consequently, more ions can be extracted to bombard the growing coating. Therefore, the energy E_{bi} increases with the increasing I_{da} . The effect of the amount of Cu incorporated in the Zr-Cu-N film on its mechanical properties is illustrated in Fig. 5. These films were sputtered at a substrate temperature of $T_s = 450^\circ\text{C}$ and substrate bias of $U_s = -100\text{ V}$. Due to high-energy ion bombardment, sputtered films exhibit compressive macrostress ($\sigma < 0$). The hardness H and the effective Young's modulus E^* , and the elastic recovery W_e and the ratio H/E^* of these Zr-Cu-N films are displayed as a function of Cu concentration in Figs. 5(a) and 5(b), respectively. The basic physical parameters of these films are given in Table I. The energy E_{bi} was calculated from a simple formula $E_{bi} = U_s i_s / a_D$ (see Refs. 36–38 for details). The amount of Cu incorporated in the film was controlled by the partial pressure of nitrogen p_{N_2} and by the inner diameter ϕ_i Cu of the copper fixing ring.

TABLE II. Physical and mechanical properties of Zr-Cu-N films sputtered at $T_s = 450^\circ\text{C}$, $U_s = 100\text{ V}$, $p_T = p_{Ar} + p_{N_2} = 1\text{ Pa}$ and used in (1) the antibacterial tests and (2) the bending and indentation tests. E_k is the efficiency of killing of *E. coli* bacteria, and the formation of cracks characterizes the resistance of the film to cracking. L is the load used in indentation test.

Film No.	p_{N_2} (Pa)	Cu (at. %)	h (nm)	a_D (nm/min)	H (GPa)	E^a (GPa)	H/E^a	W_e (%)	σ (GPa)	E_k (%)	Cracks in bending	Indentation
10	0.06 ^b	4.4	1870	31.2	24.7	231	0.107	68	-1.2	~ 0	Yes ^a	Yes ^c
11	0.24 ^b	6.4	2050	17.1	15.3	187	0.082	56	-0.8	- ^d	Yes ^a	Yes ^c
12	0.09	9.2	2090	17.4	25.4	227	0.112	70	-2.3	~ 0	No ^a	No ^c
13	0.09	11.1	2360	13.9	23.5	214	0.110	72	-2.7	100	No ^a	No ^c
14	0.06	14.8	3470	27.8 ^c	22.9	218	0.105	70	-2.1	- ^d	No ^a	No ^c
15	0.13	18.9	2440	13.1	17.3	170	0.101	63	-1.6	100	No ^a	No ^c

^aAt $\epsilon = 1.5\%$.

^bFilms sputtered at floating potential.

^cAt high indenter load $L = 1\text{ N}$.

^dNot tested for bacteria killing.

^eSputtering with new targets.

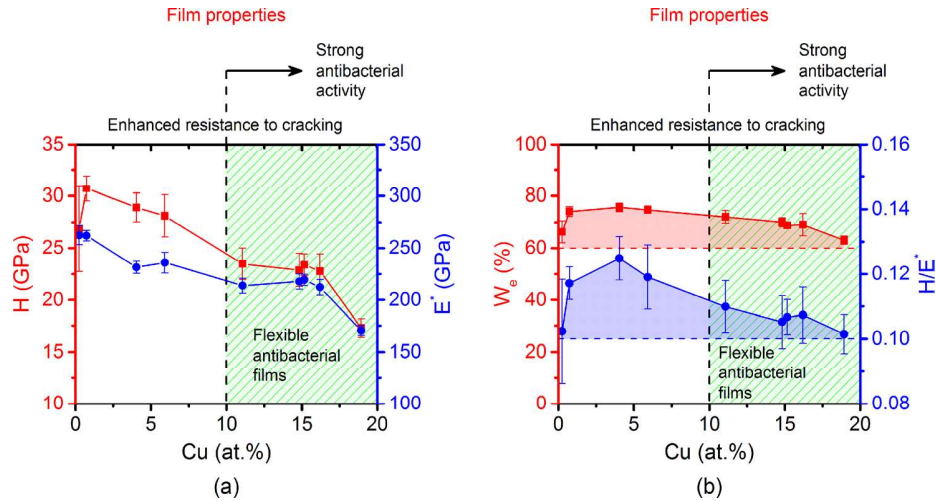


FIG. 5. (Color online) (a) Hardness H , effective Young's modulus E^* , and (b) elastic recovery W_e and H/E^* ratio of Zr-Cu-N films sputtered onto Si(100) substrates at $I_{da} = 1$ A, $T_s = 450$ °C, $U_s = -100$ V, and $p_T = p_{Ar} + p_{N_2} = 1$ Pa.

The main conclusions from the experimental data presented in Fig. 5 and Table I can be briefly summarized as follows:

- (1) The hardness H and effective Young's modulus E^* of the Zr-Cu-N films decrease with increasing Cu concentration from ~ 30 to ~ 17 GPa and from ~ 260 to ~ 170 GPa, respectively.
- (2) On other hand, the Zr-Cu-N films exhibit: (1) high values of elastic recovery ($W_e > 60\%$) and H/E^* ratio (≥ 0.1); and (2) compressive macrostress ($\sigma < 0$) over the whole range of Cu concentrations (0 to ~ 20 at. %) used in this experiment. Recently, it was shown that an H/E^* ratio of ≥ 0.1 and elastic recovery of $W_e \geq 60\%$ are two basic conditions necessary to achieve films with enhanced resistance to cracking.^{35–37} This indicates that all Zr-Cu-N films with Cu concentrations ranging from 0 to ~ 20 at. % should exhibit enhanced resistance to cracking upon bending and under high external loads. The enhanced resistance of these Zr-Cu-N films to cracking was demonstrated by bending and indentation tests described in Sec. III D.
- (3) Only Zr-Cu-N films with ≥ 10 at. % Cu simultaneously exhibited high killing efficiency (100%) of *E. coli* bacteria and enhanced resistance to cracking. Due to high hardnesses H ranging from ~ 24 to ~ 17 GPa, these films also exhibited good mechanical protection of the substrate against scratching. Thus, Zr-Cu-N films with ≥ 10 at. % Cu serve three functions, as antibacterial/flexible/protective films.

D. Enhanced resistance of Zr-Cu-N films to cracking

The resistance of sputtered Zr-Cu-N films against cracking was investigated using the bending and indentation tests. For the bending test, Zr-Cu-N films were sputtered onto Mo and Ti strips, and the coated strip was bent around a fixed cylinder with radius r_{fc} . The physical and mechanical properties of the Zr-Cu-N films used in these tests are summarized in Table II. Films Nos. 10 and 11 were sputtered onto substrates held on floating potential $U_s = U_{fl}$. Films Nos. 12–15 were sputtered at the bias $U_s = -100$ V. All Zr-Cu-N films, which were sputtered

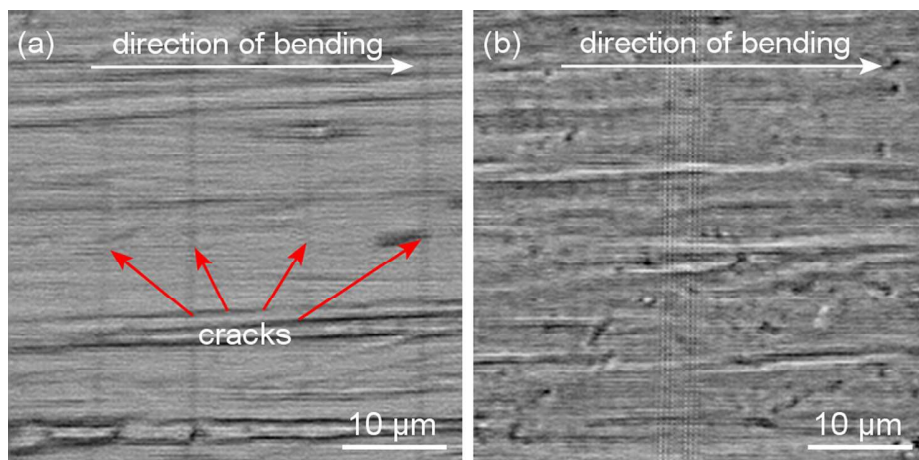


FIG. 6. (Color online) OM images of surface morphology of Zr-Cu-N films with (a) low ratio $H/E^* = 0.082$ (the film No. 11) and (b) high ratio $H/E^* = 0.112$ (the film No. 12) sputtered on Mo strip after bending around fixed cylinder of radius $r_{fc} = 10$ mm.

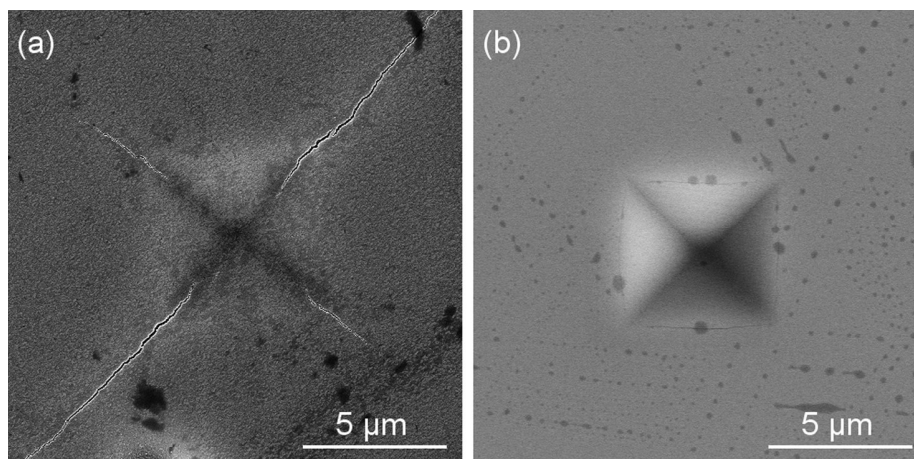


FIG. 7. SEM images of surface morphology of Zr-Cu-N films with (a) low ratio $H/E^* = 0.082$ (the film No. 11) and (b) high ratio $H/E^* = 0.112$ (the film No. 12) sputtered on Si(100) substrate after indentation by diamond indenter at high load $L = 1$ N.

at bias voltage $U_s = -100$ V, exhibited enhanced resistance to cracking (see Figs. 6 and 7), due to an H/E^* ratio of ≥ 0.1 and a high elastic recovery W_e of $\geq 60\%$ [see Fig. 5(b)]. On the other hand, the Zr-Cu-N films sputtered onto the substrate at the floating potential ($U_s = U_{fl}$) easily cracked due to a low H/E^* ratio of < 0.1 and a low W_e value of $< 60\%$, as explained in detail in Refs. 35–37. These low values resulted in lower energy E_{bi} delivered to growing films compared with that delivered to films exhibiting the high values. These results indicate that conditions of Zr-Cu-N film sputtering must be carefully selected. Here, it is important to note that in addition to the substrate bias U_s and substrate ion current density i_s , the deposition rate of the film also plays a key role in the energy E_{bi} , because $E_{bi} \approx (U_s i_s)/a_D$ (see Refs. 37 and 38 for more details).

Figures 6 and 7 show OM images and SEM images, respectively, of the surface morphology of the Zr-Cu-N films Nos. 11 and 12. The Zr-Cu-N film with H/E^* ratio = 0.082 and $W_e = 56\%$ (film No. 11) cracked in both tests, i.e., both in bending and in indentation at high load $L = 1$ N. In the bending test, the film was bent along the outer radius and cracks formed perpendicular to the bending direction. On the other hand, in the Zr-Cu-N film with H/E^* ratio = 0.110 and $W_e = 72\%$, no cracks formed under the same loading. The Zr-Cu-N film containing 9.2 at. % Cu exhibited enhanced resistance to cracking but no antibacterial activity ($E_k \approx 0$).

IV. CONCLUSIONS

The main results from the investigation on properties of flexible, antibacterial Zr-Cu-N films sputtered by dual magnetron can be summarized as follows:

(1) The Zr-Cu-N films with Cu concentrations ranging from ~ 1 to ~ 19 at. % sputtered at a substrate bias $U_s = -100$ V exhibited enhanced resistance to cracking due to a high H/E^* ratio of ≥ 0.1 , high elastic recovery $W_e \geq 60\%$, and compressive macrostress ($\sigma < 0$) (see Fig. 5).

- (2) Only Zr-Cu-N films with ≥ 10 at. % Cu concentrations exhibited antibacterial activity and efficiently killed *E. coli* bacteria. One hundred percentage of *E. coli* bacteria were killed after 5 h of contact with the Zr-Cu-N film surface.
- (3) The Zr-Cu-N films with ≥ 10 at. % Cu concentrations, hardness H ranging from ~ 17 to ~ 25 GPa, H/E^* ratios ≥ 0.1 , elastic recovery $W_e \geq 60\%$, and compressive macrostress ($\sigma < 0$) simultaneously exhibited 100% efficiency in killing of *E. coli* bacteria and enhanced resistance to cracking.

ACKNOWLEDGMENT

This work was supported in part by the Grant Agency of the Czech Republic under Projects P 108/12/0393.

- ¹L. A. Brook, P. Evans, H. A. Foster, M. E. Pemble, A. Steele, D. W. Sheel, and H. M. Yates, *J. Photochem. Photobiol. A* **187**, 53 (2007).
- ²J. Musil, M. Louda, R. Čerstvý, P. Baroch, I. B. Ditta, A. Steele, and H. A. Foster, *Nanoscale Res. Lett.* **4**, 313 (2009).
- ³H. A. Foster, D. W. Sheel, P. Sheel, P. Evans, S. Varghese, N. Rutschke, and H. M. Yates, *J. Photochem. Photobiol. A* **216**, 283 (2010).
- ⁴C. M. Jones and E. M. V. Hoek, *J. Nanopart. Res.* **12**, 1531 (2010).
- ⁵H. A. Foster, I. B. Ditta, S. Varghese, and A. Steele, *Appl. Microbiol. Biotechnol.* **90**, 1847 (2011).
- ⁶J. H. Hsieh, T. H. Yeh, S. Y. Hung, S. Y. Chang, W. Wu, and C. Li, *Mater. Res. Bull.* **47**, 2999 (2012).
- ⁷J. H. Hsieh, T. H. Yeh, C. Li, S. Y. Chang, C. H. Chiu, and C. T. Huang, *Surf. Coat. Technol.* **228**, S116 (2013).
- ⁸J. H. Hsieh, C. H. Chiu, C. Li, W. Wu, and S. Y. Chang, *Surf. Coat. Technol.* **233**, 159 (2013).
- ⁹J. H. Hsieh, T. H. Yeh, C. Li, C. H. Chiu, and C. T. Huang, *Vacuum* **87**, 160 (2013).
- ¹⁰P. K. Chu, *Thin Solid Films* **528**, 93 (2013).
- ¹¹H. L. Huang, Y. Y. Chang, J. C. Weng, Y. C. Chen, C. H. Lai, and T. M. Shieh, *Thin Solid Films* **528**, 151 (2013).
- ¹²H. L. Huang, Y. Y. Chang, Y. C. Chen, C. H. Lai, and M. Y. C. Chen, *Thin Solid Films* **549**, 108 (2013).
- ¹³Y.-H. Chen, C.-C. Hsu, and J.-L. He, *Surf. Coat. Technol.* **232**, 868 (2013).
- ¹⁴S. Rtimi, O. Baghriche, A. Ehiasarian, R. Bandorf, and J. Kiwi, *Surf. Coat. Technol.* **250**, 14 (2014).
- ¹⁵G. Borkow and J. Gabbay, *Curr. Med. Chem.* **12**, 2163 (2005).

- ¹⁶X. B. Tian, Z. M. Wang, and S. Q. Yang, *Surf. Coat. Technol.* **201**, 8606 (2007).
- ¹⁷Y.-C. Kuo, J.-W. Lee, C.-J. Wang, and Y.-J. Chang, *Surf. Coat. Technol.* **202**, 854 (2007).
- ¹⁸P. C. Liu, J. H. Hsieh, C. Li, Y. K. Chang, and C. C. Yang, *Thin Solid Films* **517**, 4956 (2009).
- ¹⁹V. Ondok, J. Musil, M. Meissner, R. Čerstvý, and K. Fajfrlík, *J. Photochem. Photobiol. A* **209**, 158 (2010).
- ²⁰T. W. Chiu, Y. C. Yang, A. C. Yeh, Y. P. Wang, and Y. W. Feng, *Proceedings of the 11th International Symposium on Sputtering and Plasma Processes (ISSP 2011)*, Kyoto Research Park, Kyoto, Japan, 6–8 July 2011, pp. 495–498.
- ²¹T. W. Chiu, B. S. Yu, Y. R. Wang, K. T. Chen, and Y. T. Lin, *J. Alloy. Compd.* **509**, 2933 (2011).
- ²²Y.-H. Chan, C.-F. Huang, K.-L. Ou, and P.-W. Peng, *Surf. Coat. Technol.* **206**, 1037 (2011).
- ²³V. Stranak *et al.*, *Mater. Sci. Eng. C* **31**, 1512 (2011).
- ²⁴P. Osorio-Vargas, R. Sanjines, C. Ruales, C. Castro, C. Pulgarin, A.-J. Rengifo-Herrera, J.-C. Lavanchy, and J. Kiwi, *J. Photochem. Photobiol. A* **220**, 70 (2011).
- ²⁵G. Grass, Ch. Rensing, and M. Solioz, *Appl. Environ. Microbiol.* **77**, 1541 (2011).
- ²⁶S. K. Singhal, M. Lal, Lata, S. R. Kabi, and R. B. Mathur, *Adv. Nat. Sci.: Nanosci. Nanotechnol.* **3**, 045011 (2012).
- ²⁷X. Zhang, X. Huang, Y. Ma, N. Lin, A. Fan, and B. Tang, *Appl. Surf. Sci.* **258**, 10058 (2012).
- ²⁸T.-W. Chiu, Y.-C. Yang, A.-C. Yeh, Y.-P. Wang, and Y.-W. Feng, *Vacuum* **87**, 174 (2013).
- ²⁹J. Musil, J. Blažek, K. Fajfrlík, R. Čerstvý, and Š. Prokšová, *Appl. Surf. Sci.* **276**, 660 (2013).
- ³⁰J. H. Hsieh, T. H. Yeh, S. Y. Chang, C. Li, C. C. Tseng, and W. Wu, *Surf. Coat. Technol.* **228**, S81 (2013).
- ³¹N.-H. Chen, C.-J. Chung, C.-C. Chiang, K.-C. Chen, and J.-L. He, *Surf. Coat. Technol.* **236**, 29 (2013).
- ³²H.-W. Chen, K.-C. Hsu, Y.-C. Chan, J.-G. Duh, J.-W. Lee, J. S.-C. Jang, and G.-J. Chen, *Thin Solid Films* **561**, 98 (2014).
- ³³J. P. Chu, T.-Y. Liu, C.-L. Li, C.-H. Wang, J. S. C. Jang, M.-J. Chen, S.-H. Chang, and W.-C. Huang, *Thin Solid Films* **561**, 102 (2014).
- ³⁴J. Musil, J. Blažek, K. Fajfrlík, and R. Čerstvý, *Surf. Coat. Technol.* **264**, 114 (2015).
- ³⁵J. Musil, *Thin Films and Coatings: Toughening and Toughening Characterization*, edited by S. Zhang (CRC, Boca Raton, FL, 2015), pp. 377–463.
- ³⁶J. Musil, *Surf. Coat. Technol.* **207**, 50 (2012).
- ³⁷J. Musil, *RSC Adv.* **5**, 60482 (2015).
- ³⁸J. Musil, J. Šícha, D. Heřman, and R. Čerstvý, *J. Vac. Sci. Technol. A* **25**, 666 (2007).
- ³⁹P. Pokorný, J. Musil, P. Fitl, M. Novotný, J. Lančok, and J. Bulíř, *Plasma Processes Polym.* **12**, 416 (2015).
- ⁴⁰International Centre for Diffraction Data, PDF-2 Database Sets 1–47, Pennsylvania, U.S.A. (1997).

IV. Conclusions of the thesis

The Ph.D. thesis reports on the preparation of Zr–Cu, Zr–Hf–Cu and Zr–Hf–Al/Si–Cu thin-film alloys and nanocomposite Zr–Cu–N films by magnetron sputter deposition and their characterization by different analytical techniques.

The main results of the systematic investigations are summarized as follows:

- 1) Binary Zr–Cu thin-film metallic alloys with an amorphous structure were prepared in a very wide range of the Cu content (18–88 at.%) when the deposition was employed at the low density discharge conditions. The glass transition was unambiguously recognized for the films with the Cu content between approximately 30 and 65 at.% Cu independently of the low or high density discharge conditions used. The glass transition temperature increased gradually with increasing Cu content and the maximum of the supercooled liquid region was achieved for approximately 55 at.% Cu. A clear correlation between the evolution of the crystallization temperature and mechanical properties with increasing Cu content was observed. The deposition at the high density discharge conditions resulted in a preparation of the Zr–Cu thin-film metallic alloys with a compressive stress (<0 GPa), an enhanced hardness (>7 GPa), very smooth (surface roughness < 1 nm) and hydrophobic (water contact angle $>100^\circ$) surface.
- 2) Ternary Zr–Hf–Cu thin-film metallic alloys with an amorphous structure and glass-like behavior were prepared with a gradually increasing Hf/(Hf+Zr) ratio at 46 at.% Cu and 59 at.% Cu. A clear correlation among temperature, hardness and effective Young's modulus with increasing Hf/(Hf+Zr) ratio was observed. A linear increase of all these quantities can be attributed to an increase of average bond energy as Hf with more covalent character of bonds gradually substitutes Zr in the amorphous structure. Electrically conductive Zr–Hf–Cu thin-film metallic glasses exhibit enhanced hardness (up to 7.8 GPa), enhanced thermal stability and oxidation resistance, and very smooth (surface roughness down to 0.2 nm) and hydrophobic surface (water contact angle up to 109°). Tuning their elemental composition allows us to control the supercooled liquid region in a very wide range from 405°C to 533°C .
- 3) Quaternary Zr–Hf–Al/Si–Cu thin-film metallic alloys were found to be amorphous up to 17 at.% Al and 12 at.% Si. The glass transition was, however, recognizable only up to 12 at.% Al and 6 at.% Si by differential scanning calorimetry. The increase of the Al and Si content led to an increase of the crystallization (up to 12 at.% Al and Si) and glass transition (up to 12 at.% Al and 6 at.% Si) temperature, and mechanical properties (up to 17 at.% Al and 12 at.% Si). This increase may be explained based on the increasing effect of a covalent component of the mixed metallic-covalent bonds between Al or Si and other elements of the films. Smooth, hydrophobic and electrically conductive Zr–Hf–Al/Si–Cu thin-film metallic glasses exhibit enhanced hardness, thermal stability and oxidation resistance. A wider supercooled liquid region was obtained for the Zr–Hf–Al–Cu metallic glasses, while a better oxidation resistance for the Zr–Hf–Si–Cu metallic glasses.

- 4) Nanocomposite Zr–Cu–N films with Cu concentrations ranging from ~1 to ~19 at.% sputtered at a substrate bias $U_s = -100$ V exhibited enhanced resistance to cracking due to a high H/E^* ratio of ≥ 0.1 , high elastic recovery $W_e \geq 60\%$, and compressive macrostress ($\sigma < 0$). Only Zr–Cu–N films with ≥ 10 at.% Cu concentrations exhibited antibacterial activity and efficiently killed *E. coli* bacteria. One hundred percent of *E. coli* bacteria were killed after 5 h of contact with the Zr–Cu–N film surface. The Zr–Cu–N films with ≥ 10 at.% Cu concentrations, hardness H ranging from ~17 to ~25 GPa, H/E^* ratio ≥ 0.1 , elastic recovery $W_e \geq 60\%$, and compressive macrostress ($\sigma < 0$) simultaneously exhibited 100% efficiency in killing of *E. coli* bacteria and enhanced resistance to cracking.

The results obtained in this Ph.D. thesis will be further used for the development of advanced multilayer coatings with enhanced mechanical and thermal properties. This is, however, beyond the scope of this thesis.

V. Further publications of the candidate

1. Papers in impacted international journals

- [1] M. Kotrlová, P. Zeman, Š. Zuzjaková, M. Zítek
“On crystallization and oxidation behavior of $Zr_{54}Cu_{46}$ and $Zr_{27}Hf_{27}Cu_{46}$ thin-film metallic glasses compared to a crystalline $Zr_{54}Cu_{46}$ thin-film alloy”
J. Non-Cryst. Solids. 500 (2018) 475-481

2. Contributions at international conferences

- [1] M. Zítek, J. Musil, K. Fajflík, R. Čerstvý
“Hard antibacterial Zr-Cu-N thin films resistant to cracking”
4th Magnetron, Ion processing and Arc Technologies European Conference and 14th International Symposium on Reactive Sputter Deposition (MIATEC and RSD) 8.–11. 12. 2015, Paris, France. (poster presentation)
- [2] P. Zeman, M. Zítek, Š. Zuzjaková, R. Čerstvý, S. Haviar
“Amorphous Zr/Cu-Based Thin-Film Alloys Prepared by Magnetron Co-Sputtering”
43rd International Conference on Metallurgical Coatings and Thin Films (ICMCTF 2016) 25. - 29. 4. 2016, San Diego, USA. (co-author of oral presentation)
- [3] M. Zítek, P. Zeman, Š. Zuzjaková, S. Haviar, J. Rezek
“Amorphous Zr–Cu thin-film alloys prepared by magnetron co-sputtering”
4th International Workshop and the 3rd International Mini Workshop on Solution Plasma and Molecular Technologies (SPM-4 and Mini SPM-3) 7.–11. 6. 2016, Plzeň, Czech Republic. (oral presentation)
- [4] M. Zítek, J. Musil, K. Fajflík, R. Čerstvý, P. Zeman
“Hard antibacterial Zr–Cu–N coatings with resistance to cracking”
27th Symposium on Plasma Physics and Technology (SPPT 2016) 20.–23. 6. 2016, Prague, Czech Republic. (poster presentation)
- [5] M. Zítek, J. Musil, K. Fajflík, R. Čerstvý, P. Zeman
“Hard Antibacterial Zr–Cu–N Coatings with Resistance to Cracking”
15th International Conference on Plasma Surface Engineering (PSE 2016) 12.–16. 9. 2016 Garmisch-Partenkirchen, Germany. (poster presentation)

- [6] P. Zeman, M. Zítek, Š. Zuzjaková, R. Čerstvý, S. Haviar
“Amorphous Zr–Cu metallic alloys prepared by magnetron co-sputtering”
 15th International Conference on Plasma Surface Engineering (PSE 2016) 12. – 16.
 9. 2016 Garmisch-Partenkirchen, Germany. (co-author of oral presentation)
- [7] M. Zítek, P. Zeman, Š. Zuzjaková, R. Čerstvý, S. Haviar, J. Rezek
“Amorphous Zr–Cu thin-film alloys with metallic glass behavior”
 15th International Conference on Reactive Sputter Deposition 2016 (RSD2016) 1.–
 2. 12. 2016 Ghent, Belgium. (poster presentation)
- [8] M. Zítek, P. Zeman, Š. Zuzjaková, R. Čerstvý, S. Haviar, M. Kotrlová
*“Mechanical and Thermal Behavior of Magnetron Sputtered Zr–Cu and Zr–Hf–Cu
 Metallic Glasses*
 44th International Conference on Metallurgical Coatings and Thin Films (ICMCTF
 2017) 24.–28. 4. 2017, San Diego, USA. (oral presentation)
- [9] P. Zeman, M. Zítek, Š. Zuzjaková, R. Čerstvý, S. Haviar, M. Kotrlová
*“Properties and thermal behavior of magnetron sputtered Zr–Cu and Zr–Hf–Cu
 metallic glasses”*
 E-MRS 2017 Spring Meeting 22.–26. 5. 2017, Strasbourg, France. (co-author of
 oral presentation)
- [10] P. Zeman, M. Zítek, Š. Zuzjaková, R. Čerstvý, S. Haviar, M. Kotrlová
*“Tuning mechanical and thermal properties of magnetron sputtered Zr–Hf–Cu me-
 tallic glasses”*
 24th International Symposium on Metastable, Amorphous and Nanostructured Ma-
 terials (ISMANAM 2017) 18.–23. 6. 2017, Donostia-San Sebastian, Spain. (oral
 presentation)
- [11] M. Zítek, P. Zeman, Š. Zuzjaková, R. Čerstvý, S. Haviar, M. Kotrlová
*“Mechanical properties and thermal behavior of Zr–Hf–Cu thin film metallic
 glasses”*
 European Congress and Exhibition on Advanced Materials and Processes (EURO-
 MAT2017) 17.–22. 9. 2017, Thessaloniki, Greece. (co-author of poster presenta-
 tion)
- [12] M. Zítek, P. Zeman, Š. Zuzjaková, R. Čerstvý, S. Haviar, M. Kotrlová
*“Tuning properties and behavior of magnetron sputtered Zr–Hf–Cu metallic
 glasses”*
 16th International Conference on Reactive Sputter Deposition (RSD 2017) 4.–6. 12.
 2017, Plzeň, Czech Republic. (poster presentation)

- [13] M. Zítek, P. Zeman, M. Kotrlová, R. Čerstvý
“Impact of alloying on properties and oxidation resistance of magnetron sputtered Zr–Hf–Cu based metallic glasses”
25th International Symposium on Metastable, Amorphous and Nanostructured Materials (ISMANAM 2018) 2.–6. 7. 2018, Rome, Italy. (oral presentation)
- [14] M. Kotrlová, M. Zítek, P. Zeman
“Differences in properties and oxidation behavior of amorphous and crystalline magnetron sputtered Zr–Cu alloys”
17th Joint Vacuum Conference (JVC 2018), 10. - 14. 9. 2018, Olomouc, Czech Republic. (co-author of poster presentation)
- [15] M. Zítek, M. Kotrlová, P. Zeman
“Differences in properties and oxidation behavior of amorphous and crystalline magnetron sputtered Zr–Cu alloys”
16th International Conference on Plasma Surface Engineering (PSE 2018), 17.–21. 9. 2018 Garmisch-Partenkirchen, Germany. (poster presentation)

Abstract

This Ph.D. thesis deals with the preparation and characterization of the Zr–Cu based thin-film metallic glasses with enhanced mechanical and thermal properties and the nanocomposite Zr–Cu–N films with enhanced mechanical properties and strong antibacterial activity.

Chapter I of the thesis is devoted to a general introduction. Chapter II defines the aims of the thesis. Chapter III is the major part of the thesis where the results obtained during the Ph.D study are presented. This chapter consists of the papers (Parts A–D) published in impacted international journals.

Binary Zr–Cu thin-film alloys were prepared by non-reactive conventional dc and impulse magnetron co-sputtering using two unbalanced magnetrons equipped with Zr and Cu targets. The magnetron with the Zr target was operated in a dc regime while the magnetron with the Cu target in a pulse regime either at low or high density discharge conditions. It was shown that Zr–Cu thin-film metallic glasses were prepared with the Cu content between approximately 30 and 65 at.% Cu independently of the low or high density discharge conditions used. A clear correlation between the evolution of the crystallization temperature and mechanical properties with increasing Cu content was observed. The deposition at the high density discharge conditions resulted in a preparation of the Zr–Cu thin-film metallic alloys with a compressive stress (<0 GPa), an enhanced hardness (>7 GPa), very smooth (surface roughness < 1 nm) and hydrophobic (water contact angle $>100^\circ$) surface.

Ternary Zr–Hf–Cu thin-film alloys with glass-like behavior deposited by non-reactive conventional dc and high-power impulse magnetron co-sputtering using three unbalanced magnetrons equipped with Zr, Hf and Cu targets were discussed. Two series of films with a gradually increasing Hf/(Hf+Zr) ratio at 46 at.% Cu and 59 at.% Cu were deposited. A clear correlation among the evolution of the glass transition temperature, crystallization temperature, hardness and effective Young's modulus with increasing Hf/(Hf+Zr) ratio was found. A linear increase of these quantities is attributed to an increase of the average bond energy in the films as Hf gradually substitutes Zr. The Zr–Hf–Cu thin-film metallic glasses exhibit enhanced hardness (up to 7.8 GPa), enhanced thermal stability and oxidation resistance, very smooth (surface roughness down to 0.2 nm) and hydrophobic surface (water contact angle up to 109°), and very low electrical resistivity (lower than $1.9 \times 10^{-6} \Omega\text{m}$).

Quaternary Zr–Hf–Al/Si–Cu thin-film metallic alloys were prepared by non-reactive magnetron co-sputtering using four unbalanced magnetrons equipped with Zr, Hf, Al or Si, and Cu targets. Two series of films with either Al (up to 17 at.%) or Si (up to 12 at.%) addition were deposited. All Zr–Hf–Al/Si–Cu films were deposited with an X-ray amorphous structure. The glass transition was, however, recognized only up to 12 at.% Al or 6 at.% Si. The addition of Al or Si enhances mechanical properties of the films and the thermal stability of their amorphous state. This may be explained by an increase of a covalent component of the mixed metallic-covalent bonds with increasing the Al and Si content. Moreover, the Zr–Hf–Al–Cu metallic glasses exhibit a wider supercooled liquid region, while the Zr–Hf–Si–Cu metallic glasses are more oxidation resistant.

The effect of the Cu concentration in the Zr–Cu–N films on the antibacterial capacity and mechanical properties was investigated. Zr–Cu–N films were prepared by reactive magnetron sputtering from composed Zr/Cu targets using a dual magnetron in an Ar + N₂ mixture. It was found that it is possible to form Zr–Cu–N films with Cu concentrations ≥ 10 at. % that simultaneously exhibit 100% killing efficiency for *E. coli* bacteria on their surfaces, and high hardness of about 25 GPa, high ratio $H/E^* \geq 0.1$, high elastic recovery $W_e \geq 60\%$ and compressive macrostress ($\sigma < 0$). The Zr–Cu–N films with these parameters are flexible/antibacterial films that exhibit enhanced resistance to cracking. This enhanced resistance was tested by bending the Mo and Ti strip coated by sputtered Zr–Cu–N films (bending test) and loading the surface of the Zr–Cu–N sputtered on a Si substrate by a diamond indenter at high loads up to 1 N (indentation test).

In chapter IV, the conclusions of the Ph.D. thesis are given. In chapter V, further publications of the candidate are listed.

Resumé

Tato disertační práce se zabývá přípravou a charakterizací tenkovrstvých kovových skel na bázi Zr–Cu se zlepšenými mechanickými a tepelnými vlastnostmi a nanokompozitních vrstev Zr–Cu–N se zlepšenými mechanickými vlastnostmi a silným antibakteriálním účinkem.

Kapitola I této práce je věnována obecnému úvodu. V kapitole II jsou definované cíle práce. Kapitola III je hlavní částí této práce a jsou zde prezentované výsledky dosažené během Ph.D. studia. Tato kapitola se sestává z článků (Část A–D) publikovaných v mezinárodních impaktovaných časopisech.

Binární tenkovrstvé slitiny Zr–Cu byly připraveny nereaktivním konvenčním dc a pulzním magnetronovým naprašováním ze dvou nevyvážených magnetronů osazených Zr a Cu terči. Magnetron s terčem Zr byl provozován v dc režimu, zatímco magnetron s terčem Cu v pulzním režimu buď za nízké, nebo vysoké hustoty výboje. Bylo ukázáno, že tenkovrstvá kovová skla Zr–Cu byla připravena s obsahem Cu mezi přibližně 30 a 65 at.% Cu nezávisle na použití nízké nebo vysoké hustoty výboje. Byla pozorována jasná korelace mezi vývojem krystalizační teploty a mechanických vlastností s rostoucím obsahem Cu. Depozice za vysoké hustoty výboje vedla k přípravě tenkovrstvých kovových slitin Zr–Cu s tlakovým pnutím (<0 GPa), zvýšenou tvrdostí (>7 GPa), velmi hladkým (povrchová drsnost <1 nm) a hydrofobním (kontaktní úhel vody $>100^\circ$) povrchem.

Ternární tenkovrstvé slitiny Zr–Hf–Cu se skelným chováním byly deponovány nereaktivním konvenčním dc a vysoko-výkonovým magnetronovým naprašováním ze tří nevyvážených magnetronů osazených Zr, Hf a Cu terči. Byly připraveny dvě série vrstev s postupně rostoucím poměrem Hf/(Hf+Zr) při 46 at.% Cu a 59 at.% Cu. Byla nalezena jasná korelace mezi vývojem teploty skelného přechodu, krystalizační teploty, tvrdosti a Youngova modulu s rostoucím poměrem Hf/(Hf+Zr). Lineární nárůst těchto veličin lze přičíst nárůstu průměrné vazebné energie ve vrstvách s postupným nahrazováním Zr za Hf. Tenkovrstvá kovová skla Zr–Hf–Cu vykazují zvýšenou tvrdost (až 7,8 GPa), zvýšenou tepelnou stabilitu a oxidační odolnost, velmi hladký (povrchová drsnost až 0,2 nm) a hydrofobní povrch (kontaktní úhel vody až 109°), a velmi nízkou elektrickou rezistivitu (nižší než $1,9 \times 10^{-6} \Omega\text{m}$).

Kvaternární tenkovrstvé kovové slitiny Zr–Hf–Al/Si–Cu byly připraveny nereaktivním magnetronovým naprašováním ze čtyř nevyvážených magnetronů osazených Zr, Hf, Al nebo Si, a Cu terči. Byly připraveny dvě série vrstev buď s přidaným Al (až 17 at.%) nebo Si (až 12 at.%). Všechny vrstvy Zr–Hf–Al/Si–Cu byly připraveny s rentgenově amorfni strukturou. Skelný přechod byl ale rozpoznán pouze do 12 at.% Al nebo 6 at.% Si. Přidání Al nebo Si zlepšuje mechanické vlastnosti vrstev a tepelnou stabilitu jejich amorfni struktury. To lze vysvětlit zvyšujícím se podílem kovalentní složky smíšené kovalentně-kovové vazby s rostoucím obsahem Al a Si. Kovová skla Zr–Hf–Al–Cu navíc vykazují širší oblast přechlazené kapaliny, zatímco kovová skla Zr–Hf–Si–Cu jsou odolnější vůči oxidaci.

Byl vyšetřován vliv koncentrace Cu ve vrstvách Zr–Cu–N na antibakteriální chování a mechanické vlastnosti. Vrstvy Zr–Cu–N byly připraveny reaktivním magnetronovým naprašováním ze složených terčů Zr/Cu za využití duálního magnetronu ve směsi Ar + N₂. Bylo zjištěno, že

je možné připravit vrstvy Zr–Cu–N s obsahem Cu ≥ 10 at. %, které budou současně vykazovat 100% efektivitu zabíjení bakterií *E. Coli* na jejich povrchu a vysokou tvrdost kolem 25 GPa, vysoký poměr $H/E^* \geq 0,1$, vysokou elasticitou vratnost $W_e \geq 60\%$ a tlakové pnutí ($\sigma < 0$). Vrstvy Zr–Cu–N s těmito parametry jsou flexibilní/antibakteriální vrstvy, které vykazují zvýšenou odolnost proti vzniku trhlin. Tato zvýšené odolnost byla testována při ohybu Mo a Ti pásku pokrytého vrstvou Zr–Cu–N a zatěžováním povrchu naprášeného Zr–Cu–N na substrátu Si diamantovým indentorem při vysokých zátěžích až do 1 N.

V kapitole IV jsou závěry této Ph.D. práce. V kapitole V jsou uvedeny další publikace kandidáta.